Abstracts of Master Theses
Presented in February 2008

Preface

Master theses of Department of International Development Engineering, Tokyo Institute of Technology were presented successfully on July 25, 2008 and February 8, 2008. This technical report consists of the abstracts of those theses.

Technical Report of International Development Engineering

TRIDE-2008-02

Table of Contents

Path Loss Model considering Beam Tilt Angle of Base Station Antenna for Mobile Communication Systems

Student Number: 05M18107   Name: Ryoko NAGANO   Supervisor: Jun-ichi TAKADA

Abstract

-

1   Introduction

Wideband Code Division Multiple Access (*WCDMA*) is a type of third-generation (*3G*) mobile system which provides wide-area wireless voice telephony and broadband wireless data communication to mobile phones. Services such as web browsing, audio-streaming, and video-streaming are significant examples of broadband data communications.

However, these services might be limited due to attenuation and fluctuation of the received signal strength at the mobile terminal, on which the installation of base station (*BS*) could have a big impact. Therefore, in cell planning, path loss prediction is used in order to minimize dead spots avoiding poor quality-of-service (*QoS*). Path loss is defined as the power density reduction through propagation which is affected by free space loss, reflection, diffraction, scattering, and absorption. The simplest path loss model is Friis' law which describes free-space propagation. Friis' law on the decibell is

$$P_{\mathrm{RX}} = P_{\mathrm{TX}} + G_{\mathrm{TX}} + G_{\mathrm{RX}} + 20\log(\frac{\lambda}{4\pi d}), \quad (1)$$

where P_{RX} and P_{TX} denote the received power and the transmit power respectively, G_{TX} is the transmit antenna gain to the direction of the receive antenna, G_{RX} is the receive antenna gain, and $20\log(\frac{\lambda}{4\pi d})$ represents the free-space path loss.

Several path loss models have been proposed for mobile communications. Some were derived analytically considering the laws that govern electromagnetic wave propagation. These models require geometrical information such as the building height, the street width, etc. Others were derived empirically based on field measurements and observation. These empirical models usually include small-scale-fading and large-scale-fading. For macrocell planning, one of the popular empirical path loss models

is the Okumura-Hata model [1, 2] which is widely used to predict path loss because of its simplicity and the applicable range of the parameters. The Okumura-Hata model is expressed in a closed form of the antenna heights, the carrier frequency and the distance between the BS and mobile station (*MS*). The Okumura-Hata equation for path loss in dB is written as

$$PL = 46.3 + 33.9\log(f) - 13.82\log(h_{\mathrm{BS}}) - a(h_{\mathrm{MS}})$$
$$+ (44.9 - 6.55\log(h_{\mathrm{BS}}))\log(d) + C_{\mathrm{m}}, \quad (2)$$

where, PL denotes the path loss, f is the frequency in MHz, d is the distance between the BS and MS antennas in km, h_{BS} and h_{MS} is the BS and MS antenna height above ground level in meter respectively, and C_{m} is defined as 0 dB for a suburban or rural (flat) environment, and 3 dB for an urban environment. The parameter $a(h_{\mathrm{MS}})$ for an urban environment is defined as

$$a(h_{\mathrm{MS}}) = 3.2(\log(11.75h_{\mathrm{MS}}))^2 - 4.97 \quad (3)$$

when $f > 400$ MHz, while for suburban and rural (flat) environments,

$$a(h_{\mathrm{MS}}) = (1.1\log(f) - 0.7)h_{\mathrm{MS}} - (1.56\log(f) - 0.8). \quad (4)$$

In order to predict the Rx power, the effect of the BS antenna gain is also to be designed considering the predicted path loss. The design of the effect of the BS antenna is important as most of the BS antennas are directional, because this saves radiation power and aids in interference suppression. In the case of line-of-sight (*LOS*) propagation, the antenna gain in the direction to the receive antenna is simply added to the transmit power. However, in macrocell scenario, the transmit signal usually travels along various paths to the receiver. This propagation is called *multipath propagation*. Thus, the effect of BS

Table 1: Measurement Information

	Area class	Urban
BS	Sectors per cell	2 or 3
	Carrier frequency	2.2 GHz
	Transmit power	30 dBm
	Antenna height	30–47.2 m
	Antenna gain	16.95 dB
	Elevation beamwidth	120 deg
	Azimuth angle (peak)	60 deg
	Beam tilt angle (electronical)	1–9 deg
	Cable loss	1.3–3.9 dB
MS	antenna height	1.7 m

antenna gain is not just viewed to go straight to the receiver but to be averaged over multipath propagation.

Therefore, in this study, how the BS antenna directivity affects the path loss prediction in multipath environment, has been examined.

Section 2 presents path loss data collection. Then, in section 4, two models are fitted by regression analysis using the path loss data. One model is the same form as Okumura-Hata model. The other model includes an additional term that could describe the effect of the BS antenna gain if it exists. Afterwards the two models are compared in terms of goodness of fit.

2 Path Loss Measurement

The field data were measured by driving through the urban service areas in western Japan. Table 1 lists the basic measurement parameters. The BS antenna directivity was tilted electronically not mechanically and thus, the antenna beam pattern was simply shifted down. The data at a measurement point consists of the Rx power and the latitude and longitude of the measured location. Thus, assuming that the receive antenna gain is zero, the path loss minus the transmit antenna gain is determined at each measurement point as we know the value of Tx power and cable loss. The equation is

$$PL - G_{\text{TX}} = P_{\text{TX}} - L_{\text{C}} - P_{\text{RX}} \tag{5}$$

where L_{C} denotes the cable loss. If the path loss and the G_{TX} data sets can be proven to be independent from G_{TX}, G_{TX} can be neglected in Rx power prediction. And then we can conclude that the effect of the BS antenna gain can be smoothed over multipath propagation.

3 Linear Regression

Regression is a method to describe the relationship between the dependent variable (path loss in this study) and the independent variables (BS-MS distance, antenna height, etc. in this study). The dependent variable is assumed to be determined by the independent variables. When the relationships between the variables can be presented by linear functions, it is called *linear regression*. The linear regression equation is written as

$$\hat{y} = \alpha + \beta_1 x_1 + \beta_2 x_2 + \cdots + \beta_p x_p, \tag{6}$$

where $\hat{y}$ denotes the dependent variable, each x_i denotes the independent variables, α and β_i denotes the intercept and coefficient of the regression model, respectively, and p denotes the number of the independent variables. The coefficients and intercept are solved using least squares which is expressed as

$$\mathbf{b} = (\mathbf{X}^T \mathbf{X})^{-1} \mathbf{X}^T \mathbf{y}, \tag{7}$$

where

$$\mathbf{y}^{\text{T}} = \begin{pmatrix} y_1 & y_2 & \cdots & y_n \end{pmatrix}, \tag{8}$$

$$\mathbf{X} = \begin{pmatrix} 1 & x_{11} & x_{12} & \cdots & x_{1p} \\ 1 & x_{21} & x_{22} & \cdots & x_{2p} \\ \vdots & \vdots & \vdots & \ddots & \vdots \\ 1 & x_{n1} & x_{n2} & \cdots & x_{np} \end{pmatrix}, \tag{9}$$

$$\mathbf{b}^{\text{T}} = \begin{pmatrix} \alpha & \beta_1 & \beta_2 & \cdots & \beta_p \end{pmatrix}. \tag{10}$$

The smaller the variance of the residual is, the better the regression model describes the relationship between the variables. The critical of the *coefficient of determination* (R^2) is often used in order to examine the goodness of fit in the resulting equations. The coefficient of determination is defined as

$$R^2 = \frac{SS_{\text{tot}} - SS_{\text{reg}}}{SS_{\text{tot}}}, \ \ 0 \leq R^2 \leq 1, \tag{11}$$

where

$$SS_{\text{tot}} = \sum_{i=1}^{n} (y_i - \bar{y}_i)^2, \tag{12}$$

$$SS_{\text{reg}} = \sum_{i=1}^{n} (y_i - \hat{y}_i)^2, \tag{13}$$

SS_{tot} stands for the total sum of squares, SS_{reg} stands for error sum of squares, $\hat{y}_i$ denotes the expected value of y_i, and $\bar{y}_i$ denotes the average of y_i. The closer R^2 is to 1.0, the better the simple linear regression model explains the relationship of the variables.

However, it is not straightforward to choose the best model based on R^2 for the models which contain different numbers of independent variables. By adding independent variables to a model, R^2 is sure to increase, though it may be quite small. Hence the *adjusted R^2* ($\bar{R}^2$) [7] is used to adjust the number of independent variables in the model. Unlike
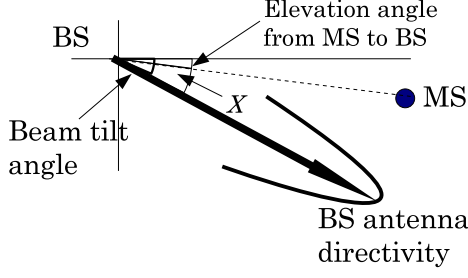
Figure 1: Definition of X as the elevation angle difference between the antenna main lobe and the LOS between the BS and MS

R^2, *adjusted* R^2 increases only if the additional term explains the model better than would be expected by chance. The *adjusted* R^2 is defined as

$$\bar{R}^2 = 1 - (1 - R^2)\frac{(N - 1)}{(N - P - 1)}, \qquad (14)$$

where P is the total number of independent variables, and N is the sample size.

4 Path Loss Models

Two path loss models are calculated by linear regression to compare their goodness of fit.

The first is the regression model which takes the same form as Okumura-Hata model. Since the carrier frequency and the MS height of the data are constant, the intercept of the model includes them. The model consists of the distance and the BS height terms, which are all in logarithm to the base 10 scale.

$$PL = (a \log(h_{\text{BS}}) + b) \log(d) + c \log(h_{\text{BS}}). \quad (15)$$

The second model is the same form as the Okumura-Hata model plus a term, $e(X + g)^2$.

$$PL = (a \log(h_{\text{BS}}) + b) \log(d) + c \log(h_{\text{BS}}) + e(X + g)^2. \quad (16)$$

where X is the elevation angle difference between the antenna main lobe and line-of-sight (LOS) between the BS and MS (see Fig. 1) and is defined as

$$X = \theta_{\text{tilt}} - \arctan(\frac{h_{\text{BS}} - h_{\text{MS}}}{d},) \qquad (17)$$

where θ_{tilt} denotes the BS antenna beam tilt angle, $\arctan(\frac{h_{\text{BS}} - h_{\text{MS}}}{d})$ represents the elevation angle looking from the MS side to the BS. Parameter X was introduced to the path loss model because BS antenna gain depends on the parameter X and hence, it is expected that the effect of antenna gain in a path loss model can be expressed more precisely by adding the parameter X appropriately if it exists.

Table 2 lists the regression result and the adjusted coefficient of determination of each model. The result of the second model which includes the

Table 2: Path Loss Models

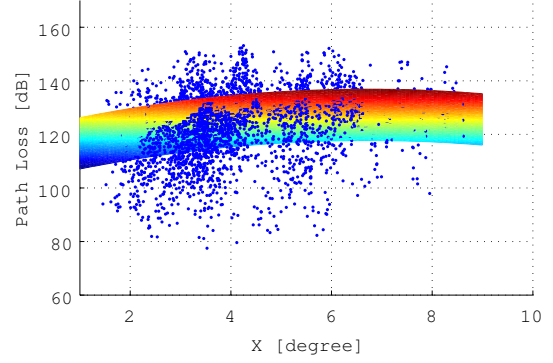| Same form as the Okumura-Hata model	$adj.R^2$
$PL = (159 \log(h_{BS}) - 223) \log(d)$ $-12.0 \log(h_{BS}) + 138$	0.17
Same form as O-H model + term of X	$adj.R^2$
$PL = (118 \log(h_{BS}) - 154) \log(d)$ $-31.3 \log(h_{BS}) + 170 - 1.08(X - 3.03)^2$	0.20

Figure 2: Second regression model of the path loss with the effect of the antenna gain

term of X shows better agreement to the measured path loss data with respect to the *adjusted* R^2. Also the significance of X is proved by hypothesis testing using the conditional F-test [8]. Since the path loss is dependent on X, its inclusion to the conventional path loss model is a significant supplement.

Figure 2 is a graph of the second regression model. The color level of regression model denotes the path loss in terms of the distance between the BS and MS. The graph presents the dependency of the second regression model on X. The path loss decreases about 8 dB, i.e. Rx power increases 8 dB, when X changes from 5 to 1 degrees. This shift of the level is similar to the vertical antenna gain pattern in the range of X: 5-1 degrees (see Fig. 3). Although this graph shows the vertical antenna gain pattern in a certain azimuth direction, the other antenna gain patterns are assumed to be approximately similar. This similarity of the shifts of the path loss and vertical antenna gain against X (5-1 degrees), suggests that X in the path loss model can possibly describe the neglected effect of the BS antenna gain and thus, give better prediction of the Rx power.

5 Conclusion

A modified path loss model based on Okumura-Hata model considering the effect of BS antenna gain was examined to predict Rx power more precisely.

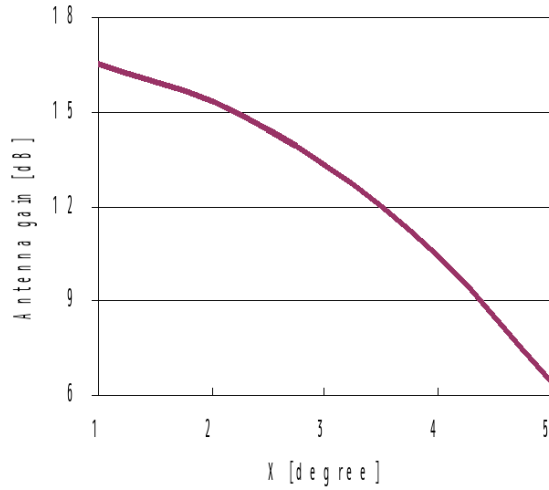The result shows that the path loss data that

Figure 3: Vertical antenna gain pattern versus X

includes the effect of the BS antenna gain is dependent on the angle X. Thus, the effect of the BS antenna gain seems to be describable by including X which is associated with antenna gain. Therefore this study proposes to present path loss excluding the BS antenna gain as

$$PL - G_{\text{TX}} = (a\log(h_{\text{BS}}) + b)\log(d) + c\log(h_{\text{BS}}) + e(X+g)^2 \tag{18}$$

by adding the term, $e(X + g)^2$ to the conventional form of the Okumura-Hata model. It should be concerned that the coefficient of X would change depending on the BS antenna gain pattern.

References

[1] M. Hata, "Propagation loss prediction models for land mobile communications", *Microwave and Millimeter Wave Technology Proceedings*, ICMMT, 1988.

[2] M. Hata, "Empirical formula for propagation loss in land mobile radio services", *IEEE Transactions on Vehicular Technology*, vol. VT-29, no.3, pp. 317-325, Aug. 1980.

[3] COST Action 231, *"Digital mobile radio towards future generation systems, final report"*, *European Communities*, EUR 18957, 1999.

[4] Y. Okumura, E. Ohmori, T. Kawatoko, and K. Fukuda, "Field strength and its variability in UHF and VHF land-mobile radio service", *Review of Electrical Communications Laboratory*, vol.16, no.9-10, pp. 825-873, 1968.

[5] J. Chambers, W. Cleveland, B. Kleiner, and P. Tukey, *Graphical Method for Data Analysis*, Chapman and Hall, 1983.

[6] J. H. Zar, *Biostatistical Analysis*, Prentice-Hall Inc., pp.82-84, 1974.

[7] J.G. Liao , D. McGee, "Adjusted Coefficients of Determination for Logistic Regression", *The American Statistician*, vol.57, 2003

[8] W. L. Carlson and B. Thorne, *Applied Statistical Methods*, pp. 724, 1997

Comparative Study of Biodiesel Production by Alkaline Transesterification from Low-valued Feeds

Student ID: 05M51263   Name: Sinthupinyo Patima   Supervisor: Egashira Ryuichi

アルカリ触媒エステル交換によるバイオディーゼル製造に対する低価格原料油の比較

シントュピンヨ　パティマー

まず，トリパルミチン(脂肪酸基C_{16})およびトリオレイン(C_{18})からなる2成分モデル混合物を原料としてメタノールおよび水酸化ナトリウム触媒によりバイオディーゼルを合成した。原料中のC_{16}の分率の増加等によりバイオディーゼルの収率は低下し純度は向上した。C_{16}とC_{18}の間の水への溶解性および乳化性の差異によるものと考えられる。ついで，粗パーム油，粗ジャトロファ油，および廃食油を原料としてバイオディーゼルを合成した。粗ジャトロファ油および廃食油に比較して，粗パーム油中のC_{16}の分率は高かった。粗パーム油を原料とした場合の収率は低く，純度は高く，モデル原料の場合の結果と一致した。粗ジャトロファ油中の不純物の分率は最も高く，前処理において多量の試薬を必要とした。

1. Introduction

Biodiesel is one of the alternative energy outstanding on the forefront of energy business due to its biodegradability, renewability, an excellent lubricity in low-sulfur diesel, high cetane number, etc.[1] Moreover, biodiesel production itself also shows the outstanding reduction in CO_2 generation drastically. Nonetheless, biodiesel commercialization has not been effective due to its high cost of production and limitation on feed cost and supply.

This study comparatively investigates differences among low-valued oils used as feedstock for biodiesel production in order to minimize cost of biodiesel production and to increase feed supply and flexibility of biodiesel production. In the first phase of this study, a binary model feed oil was transesterified to examine the relations among feed oil composition, the required reaction conditions, the biodiesel yield, and purity. Then, the real feed oils were applied in the second phase of study. The characterization of the feed oils, the pretreatment to remove impurities in the feeds, and biodiesel syntheses from the pretreated feeds were conducted and their relations were discussed.

2. Transesterification of Binary Model Mixture
2.1. Experimental

A binary mixture of pure tripalmitin (C_{16}) and triolein (C_{18}) (Wako Pure Chemical Industries, ltd.) was selected as a model feed oil to be transesterified to biodiesel (methyl ester form). The reaction was carried out in a 50 cm^3 three-necked flask, which was equipped with reflux condenser, and temperature-controlled bath oil. After 30 ml of the oil was heated to a specified temperature in the reactor, the mixture of methanol and sodium hydroxide, the catalyst, was added to the oil. The transesterification was a set of simultaneous reactions and is heterogeneous during reactions. Therefore, the liquids in the reactor were well mixed by a magnetic stirrer and this state was kept for one hour. During the reaction, nitrogen gas was purged inside to avoid moisture contamination and oxidation from air. After the transesterification, oil and glycerol phases were separated into each other by decantation funnel. The oil phase was freed of methanol, soaps and glycerol by washing with warm water (20 % mass of oil phase), was dried over magnesium sulphate, and was filtered to remove the solid drying agent.[2] Methyl ester content in oil phase was determined by analysis using a gas chromatograph (G-3000, Hitachi Co. Ltd).

Table 2-1 shows the principal experimental conditions. The composition of the feed oil, namely, the mass ratio of C_{16}/C_{18}, F, mass percentage of sodium hydroxide to the feed oil, C, molar ratio of methanol relative to the feed oil, M, and reaction temperature, T, were varied first to know roughly the effects of these variables on the biodiesel yield and purity. The ranges of M and C widely used were employed here. The range of T was selected based on the boiling point of methanol (64.7 °C) and sufficient temperature to equilibrate the reaction system within one hour (aprrox. 45 °C~). Next, in the ranges allowing high conversion of methyl ester, the effects of the respective variables on the biodiesel yield and purity were analyzed by means of a simple mathematical way[3].

Table 2-1: Principal experimental conditions

F [–]	C [%]	M [–]	T [°C]
0 ~ ∞	0.25~1.25	3~9	45~65

2.2. Results and Discussion

Biodiesel yield (Y) was defined as the mass ratio of methyl esters in the obtained biodiesel phase relative to the feed oil and biodiesel purity (P), as the mass fraction of methyl esters in the biodiesel phase.

The experimental results obtained under the various conditions of Table 2-1 were narrowed down experimentally based on the ranges, which gave the great yield and purity. Except that of F, which was based on typical fatty acid composition in vegetable oil.

As the result, the optimum ranges of conditions were obtained and shown in Table 2-2

Table 2-2: Optimum experimental conditions

F [–]	C [%]	M [–]	T [°C]
0.7 ~ 1.3	0.5~1.0	5~7	50~60

These ranges of F, C, M, and T were transformed into those of encoded variables, X_F, X_C, X_M and X_T, valued from −1 to 1 for each variable. Y and P could, thus, be expressed by simple quadratic equations of the encoded variables as,

$$Y = (99.54 - 0.39X_F - 1.05X_C + 0.44X_M - 0.45X_T - 0.11X_F^2$$
$$- 0.80X_C^2 - 0.35X_M^2 + 0.04X_T^2 - 0.42X_F X_C + 0.05X_F X_M$$
$$- 0.38X_F X_T - 0.01X_C X_M - 0.39X_C X_T + 0.05X_M X_T)/100 \quad (1)$$

$$P = (99.01 + 0.27X_F + 3.24X_C + 1.04X_M + 0.89X_T + 0.59X_F^2$$
$$- 2.83X_C^2 - 0.42X_M^2 - 0.05X_T^2 - 0.11X_F X_C - 0.10X_F X_M$$
$$- 0.26X_F X_T - 0.11X_C X_M - 0.32X_C X_T - 0.01X_M X_T)/100 \quad (2)$$

where the coefficients on the variables were obtained by the method of least squares with the experimental results. The influences of F, C, M, and T on the biodiesel yield and purity were evaluated using these equations.

Figure 2-1 shows the relations between one of the encoded variables, X_F, X_C, X_M, and X_T, and the biodiesel yield, Y, or purity, P, when the other encoded variables were fixed at 0, the center point. Y decreased with F, or T and increased with M. The effect of F was explained as follows: low-molecular weight oil has higher saponification value and is converted into soaps more; the formed soap increases triglyceride loss, lowers the reaction rate by foaming with gas in the reactor, and interferes the separation between methyl ester and glycerol. P increased, as either F, M, or T increased. Glycerides with short-chain of fatty acid remaining not converted into methyl esters would have higher solubility in glycerol phase than that with long-chain, so that the higher F gave the
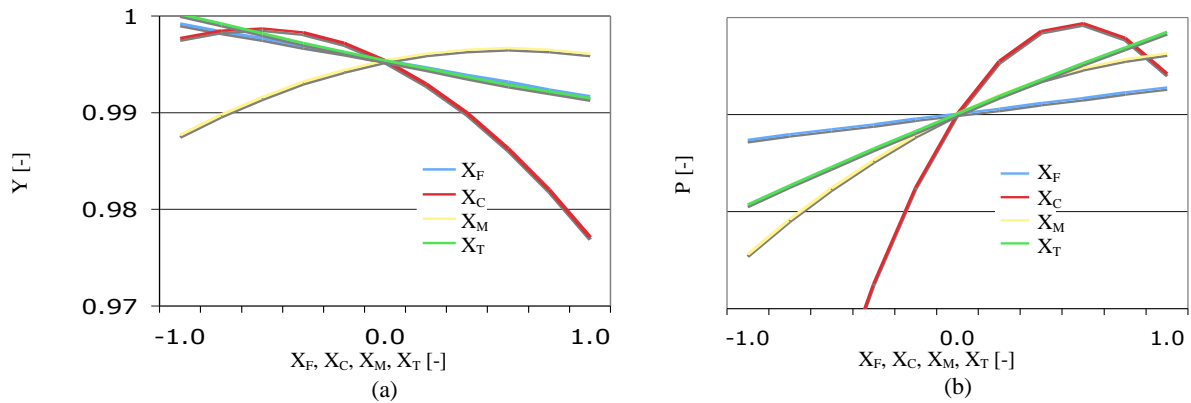

Figure 2-1: Relations between X_F, X_C, X_M, X_T, and: (a) Y; (b) P
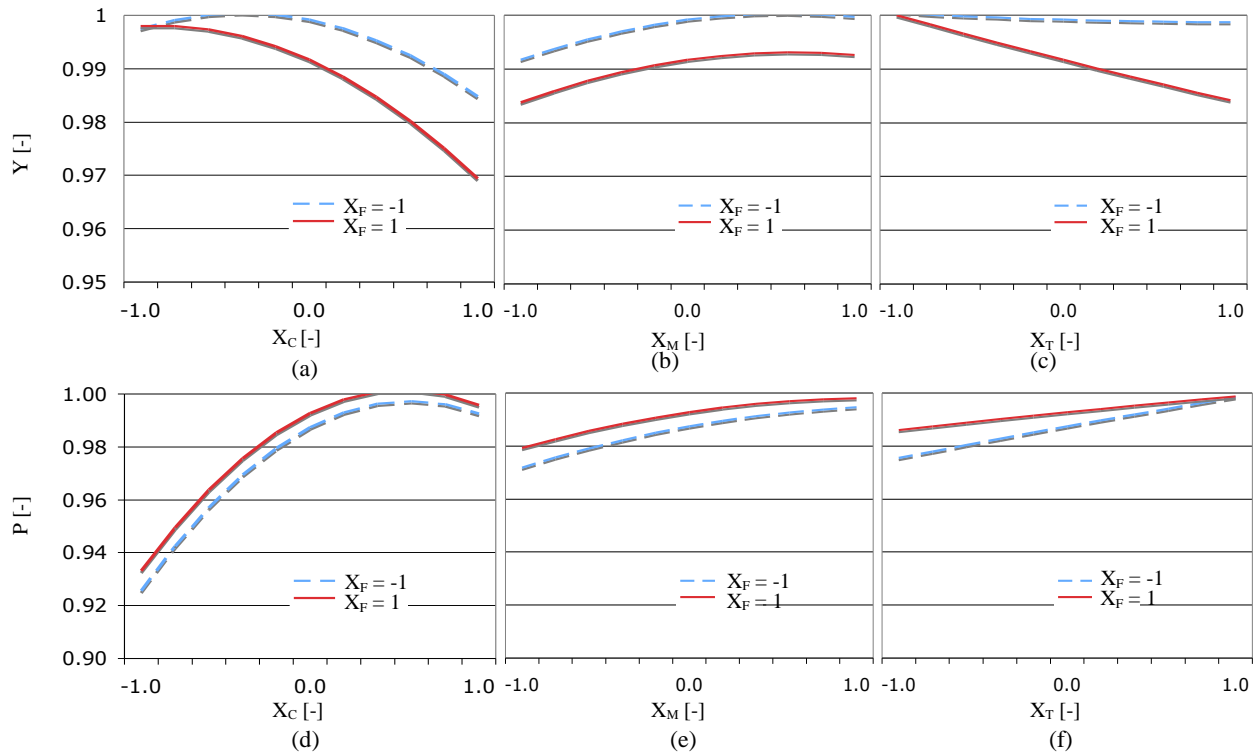

Figure 2-2: Interactions between X_F and other variables

6

higher biodiesel purity. Y had the maximum over M. Due to reversibility of transesterification, lower amount of methanol will reduce drive of forward reaction and have a negative effect on reaction yield, while higher amount of methanol increased side reaction and solubility of methyl ester into glycerol as well. Y and P had the maxima over C, namely, too high C gave low Y and P. This is due to saponification side-reaction of triglyceride instead of transesterification under too high C. This side-reaction led to the triglyceride loss and the formation of soaps. The effects of C on both Y and P were the strongest among those of the studied variables.

The interactions between the effects of X_F and the other variables on biodiesel yield, Y, and purity, P, were presented in Figure 2-2, where X_F was fixed at 1 or −1 while the other variables were varied from −1 to 1 for the both value of X_F. The influences of C and T on Y were more significant at higher F, while those of M were quite the same irrespective of X_F. In other words, it was presumed that the appropriate amount of catalyst should be chosen for each of feed oil, since the catalyst amount giving the maximum yield varied with the feed oil composition. The influences of all the variables on P were the same regardless of X_F.

3. Biodiesel Production from Low-valued Feeds
3.1. Feed oil selection
Crude palm oil (CPO), crude jatropha oil (CJO), and used frying oil (UFO) were selected as low-valued feed in this study. The merits of CPO is a high scale of production, lower price than any other vegetable oils such as soy bean oil, rapeseed oil, sunflower oil, *etc.*. CJO is superior in respect of inedibility, *i.e.*, no oil competition with food use, drought-resistant perennial, and growing well in even poor soil. UFO is considered as the costless oil, recycle and value-add the un-use vegetable oil.

3.2. Experimental
CPO and CJO were obtained from Malaysia and Thailand, respectively. UFO was obtained from a company treating used oil in Japan (Someya Shouten Ltd., Sumida, Tokyo).

The feed oils were analyzed by the same gas chromatograph as mentioned above after sufficient transesterification of triglycerides in the oils to methyl ester to know fatty acid chain compositions. Phosphorus and water contents were analyzed by an inductively coupled plasma spectrometer (SPS 7800, Seiko Instruments Co. Ltd.) and a Karl-Fisher titrator (758 KFD Titrino, Metrohm Co. Ltd.), respectively. Acid value was determined according to ASTM D 664. The average molecular weight of fatty acid and triglyceride were calculated from the composition of oil and the content of free fatty acid. Concentration of methyl ester in the biodiesel product was determined by the gas chromatograph.

The real feed oils contain impurities unfavorable for biodiesel production, *e.g.*, phosphorus, free fatty acid, moisture. These impurities not only contaminate in biodiesel product but reduce biodiesel yield as well. The feed oils were, thus, pretreated to remove phosphorus (degumming, DG), free fatty acid (deacidification, DA), and water (drying), before sent to transesterification. Some or all of these pretreatments were carried out, in order to investigate the influences of the respective pretreatments on the biodiesel yield and purity.

The experimental apparatus and procedure for the transesterification were the same as those with the model feed oil as described in Section 2.1. In transesterification, the methanol/oil ratio, M, and the catalyst concentration, C, were varied from 3 to 6 and 0.5 % to 1.5 %, respectively.

3.3. Results and discussion
Fatty acid compositions, free fatty acid contents (%FFA), moisture contents, and phosphorus contents of the fresh feed oils are shown in Table 3-1 together with the previous result [4)-6)]. All of the feed oils contained fatty acid chains mainly of C_{16} and C_{18} and CPO had more C_{16} chains than CJO and UFO.

If there was no pretreatment, biodiesel yield decreased from 99 % and 96 % to 60 % and 71 % in the case of CPO and UFO, respectively, and jelly-soap instead of biodiesel formed entirely in the reactor in the case of CJO. Biodiesel could not be produced in the case of CJO and the biodiesel yield considerably decreased in the case of CPO, without deacidification (DA). DA was the most significant of all the pretreatments in this study. Degumming was necessary only in the case of CJO, of which phosphorus content was the highest.

Table 3-1: Properties of Feed Oil

|	CPO		CJO		UFO	
	This study	Maycock[5)]	This study	Azam[4)]	This study	Merve[6)]
Myrstic acid (C14:0) [%]	1.13	1.08	nil	1.4	nil	0.23
Palmitic acid (C16:0) [%]	35.02	44.0	10.25	15.6	7.72	11.93
Stearic acid (C18:0) [%]	4.63	4.5	13.84	9.7	3.98	3.80
Oleic acid (C18:1) [%]	42.11	39.2	42.7	40.8	34.42	31.25
Linoleic acid (C18:2) [%]	16.60	10.1	26.26	32.1	53.89	50.76
Avg. fatty acids MW	272	267	277	276	280	276
Avg. oil MW	854	840	869	866	877	866
Free fatty acid [%]	5	N/A	11	N/A	0.62	N/A
Acid value [mg-KOH/g-oil]	10.3	N/A	22.3	N/A	1.24	N/A
Phosphorus [ppm]	9.01	N/A	40.15	N/A	8.93	N/A
Water [%]	0.47	N/A	2.3	N/A	0.72	N/A
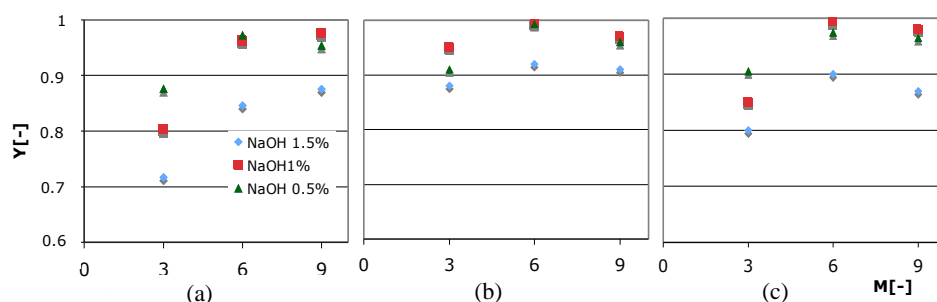
Figure 3-1: Effect of the mass ratio of methanol to feed oil, M, on the biodiesel yield, Y: (a) in the case of CPO; (b) CJO; (c) UFO
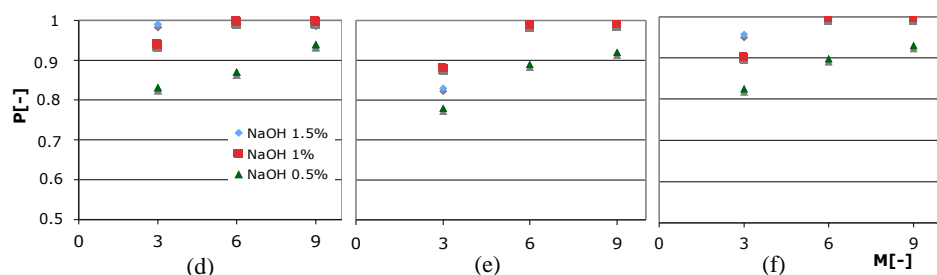

Figure 3-2: Effect of the mass ratio of methanol to feed oil, M, on the biodiesel purity, P: (a) in the case of CPO; (b) CJO; (c) UFO

Biodiesel yield comparison among CPO, CJO, and UFO in the case with all pretreatments is shown in Figure 3-1. The biodiesel yields of 99 % or more could be obtained in the cases of CJO and UFO, which contained C_{16} less, whereas the yield from CPO, whose C_{16} content was higher, was lower. The biodiesel yield had the maximum over the methanol/oil ratio, M. The emulsification of glycerol and methanol due to soap formation become serious, if the amount of methanol was too high or too low. Too much catalyst lowered the biodiesel yields.

Biodiesel purity comparison among CPO, CJO, and UFO in the case with all pretreatments is shown in Figure 3-2. All of the feed oils gave biodiesel purity more than 99 %. The highest purity was obtained from CPO, which contained C_{16} more than the other oils, the purities in the cases of the other oils were slightly lower. The highest biodiesel purities from all feed oils increased with methanol/oil ratio, M, and came to plateau around M=6. The biodiesel purity increased with amount of catalyst.

All of these results obtained with the real feed oils, CPO, CJO, and UFO, were similar to those with the binary model feed oil.

4. Conclusion

Firstly, the relations among feed oil composition, the required reaction conditions, the biodiesel yield, and purity were clarified by the transesterification run with a binary model feed oil. In the next, with the real feed oils, the requirement for the pretreatments of the feed oil was correlated with the impurities in the feed oil and the results with the model feed oil was confirmed. These results will provide useful information for design of the biodiesel production process with low-valued feed oils.

Literature Cited
1) Vicente, G.; Martinez, M.; Aracil. *J. Bioresource. Tecnol.* **2004**, 92, 297-305.
2) Dhruv, T.; Dennis, W.; Cole, G. Process Modeling Approach for Evaluating the Economic Feasibility of Biodiesel Production. **2004**.
3) Gemma, V.; Mercedes, M.; Jose, A. Optimisation of Integrated Biodiesel Production. *Bioresource. Tecnol.* **2007**, 98, 1724-1733.
4) Azam, M. M.; Amtul W.; Nahar N.M. *Biomass & Bioenergy.* **2005**, 29, 293-302.
5) Maycock, J.H. Extraction of Crude Palm Oil, in Palm Oil, edited by F.D. Gunstone, C. *Rep. Appi. Chem.*, John Wiley & Sons, New York. **1987**, 15, 29-38.
6) Merve C.; Filiz K. *Energy & Fuels.* **2004**, 18, 1888-1895.

Moving picture coding using wavelet transform

Student Number   05M18060   Name   Osamu SAKURAI   Super visor   Yukihiko YAMASHITA

MPEG

1   Introduction

Recently, the information communication technology is rapidly developed. Not only document but also picture, a sound, etc. are widely used for communication. However, the amount of information of the multimedia data which generally contains digitized pictures and sounds is huge. Therefore, in order to treat the information, the broad band method and the mass storage medium are necessary. Then, research on reduction of the information by the data compression of pictures or sounds so-called compression coding has come to be popular for the purpose of efficient use. Although the broadband communication can be used in wide area, narrowband communication is also used. Then, efficiency of image coding has to be increased.

Video coding is the method of compressing by reducing the redundancy included in video. There are two kinds of the redundancy in video data. One is the spatial redundancy and the other is temporal redundancy. The former is mainly used for still picture coding. JPEG (Joint Photographic Experts Group) which is the international standard of still picture coding is used very widely. And the algorithm called motion compensation prediction is used for the latter reduction. This is used in MPEG (Moving Picture Experts Group) which is the international-standard system of video coding. It enables to code and compress video data at high efficiency by these two techniques compared with only the former. However, such algorithm had the problem in a decoding picture. Visual degradation called block distortion is produced from process on block.

In order to solve this problem, we propose a new

moving picture coding with 2×2 pixel motion compensation prediction and wavelet. The wavelet coding which reduces block distortion is applied to our video coding method. Furthermore, motion compensation with 2×2 [pixel] block is applied. Thereby, the problem of block distortion is vanished. Moreover, various motions rotation, expansion, etc. which were not able to be used conventionally can be applied more correctly. Since correlation of data becomes high, it enables to perform efficient compression. Therefore, decoding which suppresses quality-of-image degradation is realized in small amount of data. This thesis explains the algorithm of the proposed method. Next, the advantages are confirmed by comparing with MPEG which is a video coding standard by using a computer experiment.

2   MPEG

The MPEG standard is a standard of the multimedia coding for accumulation media, broadcast, communication, etc. It mainly consists of three regulations, such as the regulation on the coding method of a video signal, the regulation on the coding method of an audio signal, and the integration method for both.

Video data is realized by set of the still picture located in a line on the time-axis. Each picture is called a frame. MPEG performs compression coding by reducing those spatial redundancy and time redundancy. Reduction of spatial redundancy is called the coding in a frame, and performs DCT (discrete cosine transform), quantization, and coding for every 8×8[pixel] block. Moreover, reduction of time redundancy is called

the coding between frames, and is performed using the technique of motion compensation prediction. This is extracting and treating the motion information on a certain domain in a picture between two near frames in time. It reduces the redundancy of video. Generally, block matching is performed for every 16×16[pixel] block. And the motion vector which is motion information is extracted. The general procedure of motion compensation prediction is shown below.

1. Extraction of motion vector by comparing between a target frame and a reference frames

2. Generation of the prediction frame by the motion vector and the reference frame

3. Generation of the picture of the difference by the difference between the prediction and the target frames

4. Coding the motion vector and the difference frame

5. Execution of 1. to the following two frames

The main coding parts of MPEG are realized with the combination of the coding between frames and within a frame. First of all as a basic procedure of MPEG, the frame of the beginning of video or the frame used as a starting point performs only the coding in a frame. These frames are called Intra-coded frame or I-frame. I-frame which had conversion-quantization performed here is inverse-transformed by the local decoder, and is temporarily memorized by the frame memory. Next, frames other than I-frame perform the coding between frames which use motion compensation prediction. There are called P-frame and B-frame. P-frame refers to a previous frame and B-frame refers to both previous and future frames.

3 Motion compensation prediction with 2×2 pixel

In the field of still picture coding, the coding which reduces block distortion using wavelet transform and subband conversion as a method has been examined. Then, in order to reduce block distortion produced in video, we try to apply the coding (wavelet coding) which used wavelet transform. However we have another problem with motion compensation prediction. Using the

block matching method used by MPEG, the problem of producing block distortion which is visual lattice-like degradation appears in the decoded video. In order to reduce block distortion using wavelet, the motion compensation prediction which uses block matching is not proper. Then, we propose the motion compensation prediction which extracts the information on a motion in 2×2[pixel] block.

3.1 2×2 pixel motion compensation prediction

Using a pixel for the macro block, the motion compensation with a pixel unit was realized. However, this method lacks in reliability. Therefore, we propose the 2×2[pixel] motion compensation prediction, which uses the recursive algorithm. In order to prevent a motion vector dispersing, a smooth portion is detected in the picture and processing suitable for the portion is performed. The algorithm of 2×2[pixel] motion compensation prediction is as follows.

1. A target block is compared to a reference frame using the block of 16×16[pixel] and extract a motion vector. The variance of pixel values of the block is calculated, and when the value is below a fixed value, the block is not divided any more.

2. Four divisions (these are called a mini blocks) of the target block are carried out. In each mini block, block matching is applied and motion vectors are extracted. The variance of pixel values of the mini blocks is calculated, and when the value is below a fixed value, the block is not divided any more.

3. For each mini block, if the block size is not 2 pixel, go to Step 2. When a target block becomes 2×2[pixel], go to Step 4.

4. Compare them with the 2×2[pixel] block finally, and the final motion vector is calculated.

3.2 Wavelet coding

Recently wavelet is used for the compression coding. When energy inlines toward low frequence bands, it is

known that very efficient coding is possible. The coding method called SPIHT (Set Partitioning In Hierarchical Trees) which is specialized in the tree structure of wavelet. This coding method is used for the coding part of the proposal technique. Correlation of the 2-dimensional motion vectors will be high supposing motion vectors obtained by block matching are extracted correctly correctly. Therefore, information inclines toward lower frequency domain. Moreover, the absolute values of the pixels in the difference frames become very small. Therefore, both information can be compressed at high efficiency using the above-mentioned wavelet coding.

4 Image coding experiment

In experiments, two frames of the standard video sequence for assessment are used for I-frame and P-frame, respectively. And coding and decoding were performed by the proposal technique. The example of a frame is shown in Fig.1. Moreover, it is compared with MPEG used as codec of Hi-Vision or standard quality-of-image television. And quality-of-image degradation of a decoding picture was evaluated numerically. PSNR is used for numerical assessment. PSNR is given by the following formulas here.

$$PSNR(dB) = 20\log\frac{255}{MSE} \quad (1)$$

$$MSE = \sqrt{\frac{\sum_{x=0}^{W-1}\sum_{y=0}^{H-1}(f(x,y) - f'(x,y))^2}{WH}} \quad (2)$$

f and f' stand for values of the original image and the decoded image. W and H stand for width and height of the image. In coding of I-frame, the block distortion of the shape of a lattice is produced by MPEG which performs block processing in a decoding picture. However, block distortion is not produced by the proposed method. In comparison of PSNR, the decoded image by the proposed method outperforms one by MPEG in the same bitrate. This result is shown in Fig. 2. In this figure, x-axis stands for bitrate of I frame and y-axis stands for its PSNR. This result shows the proposed method overcomes MPEG.

In coding of P-frame, the motion vector of the horizontal direction expressed by tone of before and after coding are shown in Fig. 3 and 4. Moreover, the comparison with MPEG by numerical assessment is shown
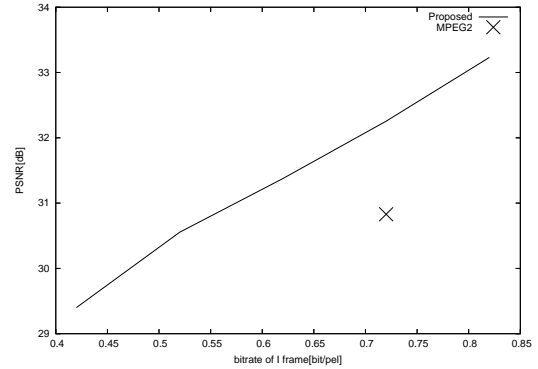

Fig. 1: Intersection

Fig. 2: PSNR for different bitrates (I frame)

in Fig. 5. In this figure, x-axis stands for bitrate of motion vector and y-axis stands for PSNR of P frame. Each result of the proposed method can not overcome MPEG. The proposed method has caused remarkable quality-of-image degradation especially around the white line of a crossing paved road or a track in a target frame. This is because matching of such a portion is incorrect and correlation of a motion vector becomes low in the case of 2×2[pixel] block motion compensation prediction.

5 Conclusions

In this paper, the video coding method using wavelet and 2×2[pixel] block motion compensation prediction was proposed, and the computer experiment was conducted. Moreover, the advantage was shown by comparing with MPEG which is an international image coding standard. For future work, we have to develop the 2×2[pixel] motion detection method that provides more highly correlated motion vectors, and a more efficient

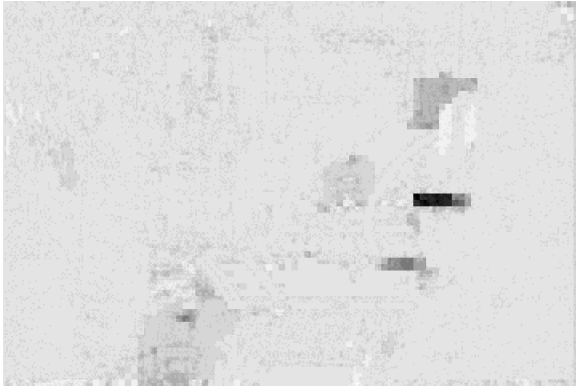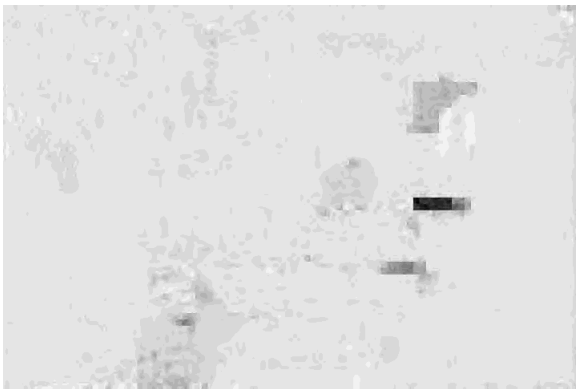coding method for the difference image. Furthermore, calculation speed have to be increased.

References

[1] Yoshinori Sakai Toshiyuki Yoshida "Image information encoding", Ohmsha, 2001.

[2] Sadayasu Ono Junji Suzuki "Achievement method of comprehensible JPEG/MPEG2" Ohmsha, 1995.

[3] Susumu Sakakibara "Wavelet beginner's guide" Tokyo Electrical Engineering College Publications Service 1995.

[4] Amir Said, William A.Pearlman "A New Fast and Efficient Image Codec Based on Set Partitioning in Hierarchical Trees" IEEE Trans. Circuits and Systems for Video Technology, vol.6, pp.243-250, June. 1996.

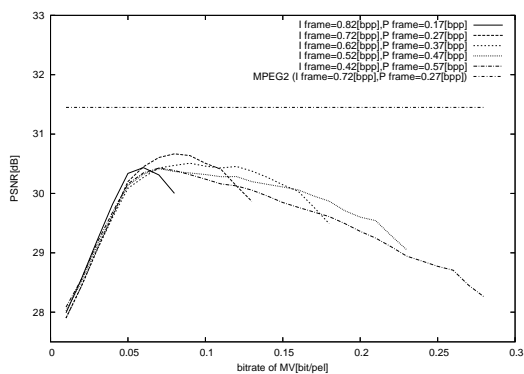Fig. 3: Before encoding

Fig. 4: After decoding

Fig. 5: PSNR for different bitrates (P frame)

Expansion of Non-negative Matrix Factorization using Fisher's Discriminant and its Application

Student Number: 05M51257　Name: Naoya KOIDE　Supervisor: Yukihiko YAMASHITA

Fisher   NMF

(NMF)　Fisher   FisherNMF

NMF

2

FisherNMF

1　Introduction

Pattern recognition is a process to distribute observed patterns to known categories. For example, in recognition of alphabet characters, we should discriminate observed patterns among 26 categories. Patterns are given by two-dimensional images, three-dimensional objects, signals in time series like sound signals, and so on.

Non-negative Matrix Factorization(NMF) is a method for extracting features. Although NMF decomposes a non-negative matrix into two non-negative matrices, a base matrix and a feature matrix obtained by NMF is not unique. Therefore NMF is not suitable for pattern recognition.

In this paper We propose FisherNMF, which is a method that Fisher's Discriminat is introdeced into NMF. and we evaluate the performance of FisherNMF by experiments.

2　Non-negative Matrix Factorization

Non-negative Matrix Factorization(NMF, Paatero and Tapper[1]; Lee and Seung[2],[3]) is a method which decomposes a non-negative matrix into two non-negative matrices.

PCA(Principle Component Analysis) proves the most suitable basis for approximate patterns. But those bases contain negative values, and meanings as images are lost. On the contrary, bases given by NMF are not so suitable for approximation, but NMF can give common parts of images as features since NMF gives non-negative values. NMF equation is defined by eq.(1).

$$\mathbf{V} \approx \mathbf{WH} \qquad (1)$$

$\mathbf{W}$ is a base matrix, and it gives images of common parts. $\mathbf{H}$ is a feature matrix, and it gives feature quantities of each data.

Since we can't determine a base matrix $\mathbf{W}$ and a feature matrix $\mathbf{H}$ uniquely, we should calculates repeatedly to obtain a solution. There are several ways to measure the distance between $\mathbf{V}$ and $\mathbf{WH}$. The most easiest way is to measure by Frobenius norm. This estimation criterion is obtained as eq.(2).

$$\min_{\mathbf{W},\mathbf{H}} \quad D(\mathbf{V},\mathbf{WH}) = \|\mathbf{V}-\mathbf{WH}\|_{\mathrm{F}}^2 \qquad (2)$$

subject to $\quad W_{ia} \geq 0, H_{bj} \geq 0, \forall_{i,j,a,b}$

Notice that $\|\mathbf{A}\|_{\mathrm{F}}^2 = \sum_{i,j} A_{ij}^2$. We should find a base matrix $\mathbf{W}$, and a feature matrix $\mathbf{H}$ which minimize eq.(2). We can obtain the

solution with a rule eq.(3), (4).

$$W_{ij} \leftarrow W_{ij} \frac{(\mathbf{VH}^T)_{ij}}{(\mathbf{WHH}^T)_{ij}} \qquad (3)$$

$$H_{ij} \leftarrow H_{ij} \frac{(\mathbf{W}^T\mathbf{V})_{ij}}{(\mathbf{W}^T\mathbf{WH})_{ij}} \qquad (4)$$

3   FisherNMF

Feature vectors obtained by NMF may not be separatable in each category in a feature space. This is because no constraint is given to a base matrix $\mathbf{W}$ and a feature matrix $\mathbf{H}$. Therefore, it is difficult to classify unknown input pattern to known categories by using NMF, and it is not suitable to apply NMF to pattern recognition.

In order to solve this problem, We propose a new method, FisherNMF. Fisher's Discriminant is a well-known method as a 2-class linear classifier. Its criterion is to minimize within class variance and maximize between class variance. In FisherNMF, by introducing the Fisher's Discriminant term to the criterion of NMF, the discrimination performance is improved.

At first, within class variance and between class variance are defined as eq.(5), (6).

$$S_W := \frac{1}{CM} \sum_{i=1}^{C} \sum_{\mathbf{h}_k \in \Omega_i} (\mathbf{h}_k - \mu_i)^T (\mathbf{h}_k - \mu_i),$$
$$(5)$$

$$S_B := \frac{1}{C(C-1)} \sum_{i=1}^{C} \sum_{j=1}^{C} (\mu_i - \mu_j)^T (\mu_i - \mu_j),$$
$$(6)$$

$$\text{where} \quad \mu_i := \frac{1}{M} \sum_{\mathbf{h}_k \in \Omega_i} \mathbf{h}_k$$

The criterion of FisherNMF is defined by eq.(7).

$$\min_{\mathbf{W},\mathbf{H}} \quad D(\mathbf{V},\mathbf{WH}) = \|\mathbf{V} - \mathbf{WH}\|_F^2 + \alpha \log \frac{S_W}{S_B}$$
$$(7)$$

subject to $\quad W_{ia} \geq 0, H_{bj} \geq 0, \forall_{i,j,a,b}$

FisherNMF minimizes not only $\|\mathbf{V} - \mathbf{WH}\|_F$ but $\frac{S_W}{S_B}$. By minimizing Fisher Discriminant term, known training patterns are separated in each category in feature space, so that FisherNMF is more suitable than normal NMF for discrimination.

Let $J = \log \frac{S_W}{S_B}$, the update rule of FisherNMF is obtained by the next equation.

$$W_{pq} \leftarrow W_{pq} \frac{(\mathbf{VH}^T)_{pq}}{(\mathbf{WHH}^T)_{pq}} \qquad (8)$$

$$H_{pq} \leftarrow H_{pq} \frac{(\mathbf{W}^T\mathbf{V})_{pq}}{(\mathbf{W}^T\mathbf{WH})_{pq} + \alpha \frac{\partial J}{\partial H_{pq}}} \qquad (9)$$

Note that the derivatives of Fisher's Discriminant term is eq.(10).

$$\frac{\partial J}{\partial H_{pq}} = \frac{\frac{2}{M} \left(MH_{pq} - \sum_{\mathbf{h}_k \in \Omega_x} H_{pk} \right)}{\sum_{i=1}^{C} \sum_{\mathbf{h}_k \in \Omega_i} (\mathbf{h}_k - \mu_i)^T (\mathbf{h}_k - \mu_i)}$$
$$- \frac{\frac{4}{M^2} \left(C \sum_{\mathbf{h}_k \in \Omega_x} H_{pk} - \sum_{i=1}^{C} \sum_{\mathbf{h}_k \in \Omega_i} H_{pk} \right)}{\sum_{i=1}^{C} \sum_{j=1}^{C} (\mu_i - \mu_j)^T (\mu_i - \mu_j)}$$
$$(10)$$

In recognition step, the update rule to feature vector $\mathbf{h}$ is the same as eq.(11). because we cannot debate about the categories of unknown input patterns.

$$\mathbf{h}_i \leftarrow \mathbf{h}_i \frac{(\mathbf{W}^T\mathbf{v})_i}{(\mathbf{W}^T\mathbf{Wh})_i} \qquad (11)$$

Note that $\mathbf{v}$ is an input pattern and $\mathbf{h}$ is a feature vector of an input pattern. The category which an input pattern belongs to is decided by nearest neightbor method.
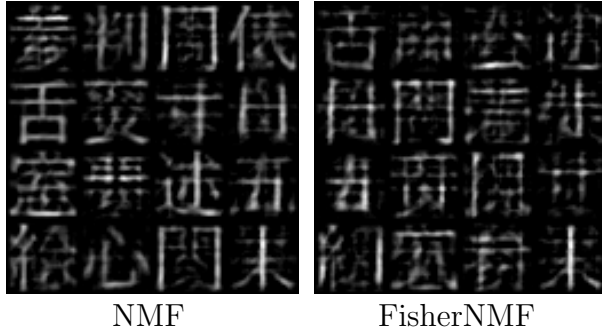
4   Experiment

At first, I conduct experiments on educational *kanji* images of different 16 fonts. 40 random selected characters are used. The size of images are 32×32. 12 fonts of 16 are used as training patterns, and 4 fonts are used as test patterns. For the dimension of feature vector r is 16 and 64 are used. α is a parameter of FisherNMF.

Table 1: Result for educational *kanji*

Method	α	Error Rate(%)	
		$r=16$	$r=64$
NMF	–	12.50	5.00
FisherNMF	0.5	9.38	4.38
	1.0	13.75	2.50
	2.0	8.13	3.75

The results are shown in Table 1. α is as shown in the table, FisherNMF gives better recognition results than normal NMF.

Obtained bases **W** are shown in Figure 1. Although FisherNMF gives a better result, images of basis by FisherNMF are not clearer than images of NMF. It is because the criterion of FisherNMF has a constraint that minimizes Fisher's Discriminant term.


NMF   FisherNMF

Figure 1: Obtained Base $\mathbf{W}(r=16)$

In the next experiment, ETL data set is used. The size of character images was reduced to 16×16. There are 160 patterns for each character. 120 patterns of 160 patterns are used for training data, and 40 patterns for test data. In this experiment, the dimension of feature vectors **W** are set to 16, 64, 256.

Table 2: Result for ETL data set

Method	α	Error Rate(%)		
		$r=16$	$r=64$	$r=256$
NMF	-	67.40	31.68	29.43
FisherNMF	0.5	72.70	33.54	30.65
	1.0	71.60	36.19	32.72
	2.0	70.90	33.31	31.01

The results are shown in Table 2. In this case, FisherNMF doesn't show better performance than NMF. The convergences of norm, $\|\mathbf{V} - \mathbf{WH}\|_{\mathrm{F}}$, on each step is shown in Figure 2. In case of FisherNMF, the iteration converged to a local minimum point. Since the criterion of FisherNMF is more complex, the iteration falls into a local minimum.
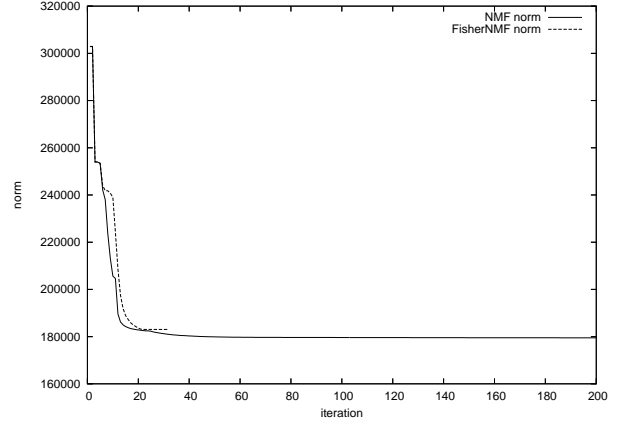
Figure 2: Convergence of $\|\mathbf{V} - \mathbf{WH}\|_{\mathrm{F}}(r = 16)$

On some characters. I selected 30 characters which look like (Table 3). These characters have a very similar part with each other. Therefore pattern recognition becomes difficult for them.

Table 3: Characters Used on the Experiment

Table 4: Result

Method	α	Error Rate(%)	
		$r=16$	$r=64$
NMF	–	15.83	13.33
FisherNMF	0.5	11.67	5.83
	1.0	11.67	8.33
	2.0	10.83	10.00

The results are shown in Table 4. It is obvious that FisherNMF is more efficient in this experiment.

NMF

FisherNMF

Figure 3: Obtained Base $\mathbf{W}(r = 64)$

The obtained bases are shown in Figure 4. Although NMF does not distinguish any parts of characters, FisherNMF emphasizes main parts of characters which is called *bushu*. This is because FisherNMF clarifies the difference between each categories.

5 Conclusions

In this paper, We proposed FisherNMF, which is a method that Fisher's Discriminant is introduced into NMF. Furthermore, we evaluated performance of FisherNMF by experiments on *kanji* images, comparing NMF and FisherNMF. As a result, FisherNMF showed well on some conditions. We have to improve convergence of FisherNMF and apply it to various fields.

References

[1] Paatero, Tapper *Positive matrix factorization: A non-negative factor model with optimal utilization of error estimates of data values*, Environmetrics, vol.5, pp.111-126, 1994.

[2] D.D.Lee and H.S.Seung. *Learning the parts of objects with nonnegative matrix factorization*, Nature, 401:pp788-791, 1999.

[3] D.D.Lee and H.S.Seung. *Algorithms for non-negative matrix factorization*, Advanced in Neural Information Processing Systems 13, pp.556-562. MIT Press, 2001.

Parameter determination method for constitutive model of sand based on relative density relation

Student Number: 06M18010 Name: Takanori AOKI Supervisor: Thirapong PIPATPONGSA

密度の相違を考慮した砂の構成モデルとそのパラメータの決定法

青木　孝憲

砂質土のせん断挙動に関して最も支配的なのは初期状態における密度の違いである．この相違を統一的に表現できる構成モデルについては既に提案されているが，それらに関わるパラメータの多くは明確に決定する手法が現時点で存在しないため，実務レベルでの活用に至っていない．本研究では，全てのパラメータを客観的に決定できることを主眼におき，下負荷面の発展則を導入した構成モデルを用いた．密度の違いを構成モデル内における降伏応力の違いとして考え，それを定量的に評価できる手法を提案する．またその妥当性を，初期密度の異なる砂の非排水三軸試験結果と比較して検討を行っている．

1. Introduction

The most influential property of sandy soil on elasto-plastic behavior is the degree of density. Shearing behavior of sandy soil does not entirely depend only on current stress condition and stress history, but also relative density.
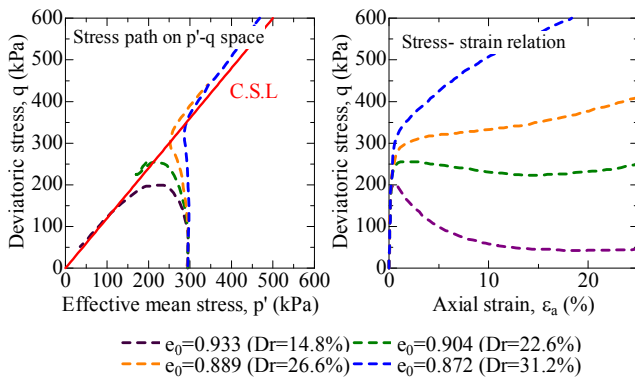

Fig.1 Experimental result of undrained shear test
Left: Stress path on p'-q space
Right: Stress-strain relationship

Fig.1 shows the experimental results of undrained shear test for various initial relative density (Dr) conducted by Kato, Ishihara and Towhata (2001)[1].

2. Previous researches

Many researchers have proposed constitutive models which can express shearing behavior of sandy soil. Asaoka et al. (2002) proposed the Sys-Cam clay model[2] which can suitably express shearing behavior of both dense and loose sand[3]. However, parameters determination method has not been specifically defined yet. That is why, this model is not used in practical analyses. Due to setback of parameter determination for the Sys-Cam clay model, EC model[4] proposed by Ohno et al.(2006) including Sub-loading surface[5] (Hashiguchi, 1989), was employed in this research. This model can more or less express sandy soil behavior at a certain level. Besides, all parameters can be determined obviously.

3. Parameters determination method

3.1 Parameter which interpret "degree of density"

In order to represent "the degree of density" in constitutive model, the parameter which can govern a relative density is necessary. However, typical constitutive models; the modified Cam clay, the Sekiguchi-Ohta, EC models and so on, do not have such parameter, because these model were rooted in the experimental results of clays, not sand.

On the other hand, the characteristics under drained and undrained shear condition of over-consolidated clay and dense sand are similar. Therefore, in this research, the degree of density is assumed to associate with the yielding stress parameter, p'_0. Fig.2 shows the concept of Dr relation with p'_0.
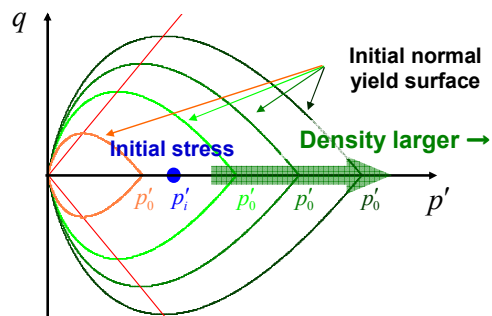

Fig.2 Illustration of $Dr - p'_0$ relation

3.2 Sub-loading surface model

In fact, over-consolidated state is represented as the stress bounded within the yield surface. In this case, the simulated behavior of soil becomes elastic, as far as the stress remains inside the yield surface by using typical constitutive model. In this research, a degree of density is interpreted to a degree of over-consolidation by the constitutive model. As a consequence, in the case of undrained shearing simulation for dense sand, elasto-plastic response does not exhibit at the initial stage. On the other hand, realistic range of elastic response for sand carried out under undrained shear test is very small, ($\varepsilon \approx 10^{-6} \sim 10^{-5}$ at strain level). Thus, typical constitutive model cannot satisfactorily describe realistic behavior of sand (See black lines in Fig.3).

Sub-loading surface model was proposed by Hashiguchi (1989). In this model, sub-loading surface always passes through a current stress point in the stage not only loading but also unloading process while keeping a similarity to the normal-yield surface. Besides, it is assumed that the sub-loading surface approaches asymptotically to the normal-yield surface in a loading process, causing a decrease of plastic modulus (See Fig.3).
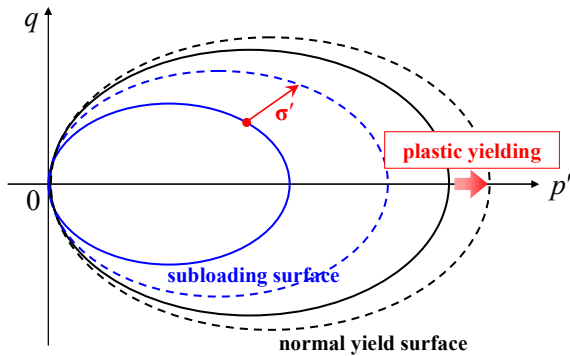

Fig.3 Illustration of the Sub-loading surface model

Expansion ratio of sub-loading surface to normal yield surface, $\dot{R}$ (where $0 < R \leq 1$) is defined by the following Eq. (1).

$$\dot{R} = m \ln R \left\| \dot{\boldsymbol{\varepsilon}}^p \right\| \tag{1}$$

where, R : similarity ratio of sub-loading surface
$\quad m$: expansion rate parameter
$\quad \boldsymbol{\varepsilon}^p$: plastic strain tensor

By using this model, it is possible to describe elasto-plastic response for the state of stress within the normal yield surface (See red lines in Fig.4). It is obvious that for over-consolidated soil, shear behavior simulated by using sub-loading surface model is far more realistic than that simulated without using sub-loading surface model.
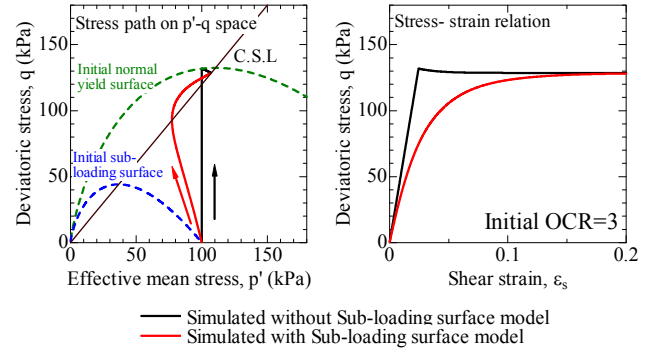

Fig.4 Simulated result with sub-loading surface model
& without sub-loading surface model
Left: Stress path on p'-q space
Right: Stress-strain relationship

3.3 Method for estimation of p_0'

In order to estimate the realistic p_0' , experimental result is required. Through the observation of Fig.1, shear behavior among each initial density can be categorized to 3 types:

① Dense: q is monotonically increasing.

② Intermediate: q becomes stable at critical state.

③ Loose: q becomes decreasing after critical state.

On the other hand, the behavior of undrained shear simulation on normally consolidated soil is similar to type ②. Therefore, the realistic value of p_0' can be classified into the following Table (1).

Table (1)

Type	Experimental result		Constitutive model
	Degree of density	Relative density, D_r(%) in Fig.1	Yield stress, p'$_0$
①	Dense	26.6, 31.2	$p_0' > p_i' (0 < R < 1)$
②	Intermediate	22.6	$p_0' = p_i' (R = 1)$
③	Loose	14.8	$p_0' < p_i' (1 < R)$

In Fig.1, behavior of loose sand (type ③, Dr =14.8%) cannot be described by using sub-loading surface model, because the similarity ratio of sub-loading surface must be defined in the range $0 < R \leq 1$. This is why, the modeling of loose sand is out of scope in this study.

Generally, the value of yielding stress is obtained by e-lnp' relationship. Therefore, compression and swelling indexes of sand are required. Sakajo et al. (1995) performed isotropic consolidation/swelling tests on sand with different grain size distribution by using triaxial apparatus[6]. Tests ware carried out for various relative density at the initial states. Fig. 5 shows the relation between compressing and swelling indices, λ , κ and the initial relative density Dr before loading. It is obvious that λ and κ do not depend on characteristics of grain size distribution but depend on initial relative density, i.e., the larger initial density is,

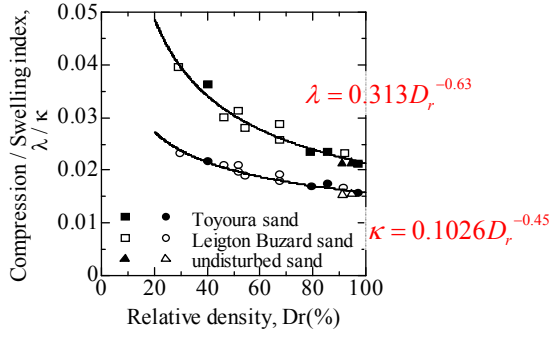the smaller λ and κ are observed.

Fig.5 Relationship between λ, κ and initial Dr

According to these experimental results, the concept for estimating p'_0 is proposed. Fig. 6 shows the illustration of the relationship between initial void ratio, e which can directly related to the relative density, and to p'_0. This idea has no objection with the typical characteristics of soil under compression loading. The initial void ratio of sand in corresponding to the initial consolidated pressure p'_i refers to the various degree of density. Among of them (e_{ref}, e_1, e_2 in Fig.6), e_{ref} defined as the intermediate state (type ②) can be obtained from the process of undrained shear test. In regarding to the state compressed from e_{ref}, compression index is adopted as λ_{ref}, because e_{ref} (Dr_{ref}) is considered as the normal consolidated condition in the constitutive model. λ_{ref} can be obtained from Eq. (2).

$$\lambda_{ref} = \lambda = 0.313 Dr^{-0.63} \qquad (2)$$

Denser state (e_1, e_2 in Fig.6) is considered to be "over-consolidated state" in constitutive model. Thus, in regarding to the state compressed from e_1, e_2, compression index is adopted as κ which can be obtained from Eq. (3).

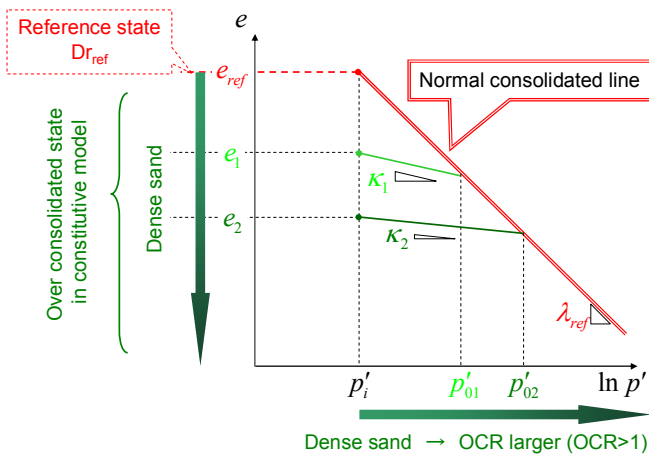$$\kappa = 0.1026 Dr^{-0.45} \qquad (3)$$


Fig.6 Illustration of the relation density to p'_0

The intersecting point of λ_{ref} line from e_{ref} with κ_1, κ_2 line from e_1, e_2 is supposed to estimate p'_0.

3.4 Parameters determination procedures

Fig.7 shows the flow chart of parameters determination. The proposed procedure is divided into 2 sections.

At section 1: "reference state", e_{ref} (Dr_{ref}) will be found based on the experiment result of undrained shear test. This state is interpreted as the "normal consolidated state" in constitutive model.

At section 2: "dense state", p'_0 related to e_i ($e_i < e_{ref}$) will be estimated by using the determined parameters obtained from section1. In addition, dense state is considered as "over-consolidated state" in constitutive model. Therefore, sub-loading surface parameter, m is required. This parameter will be determined by curve fitting with experimental results; stress path and stress-strain relation.
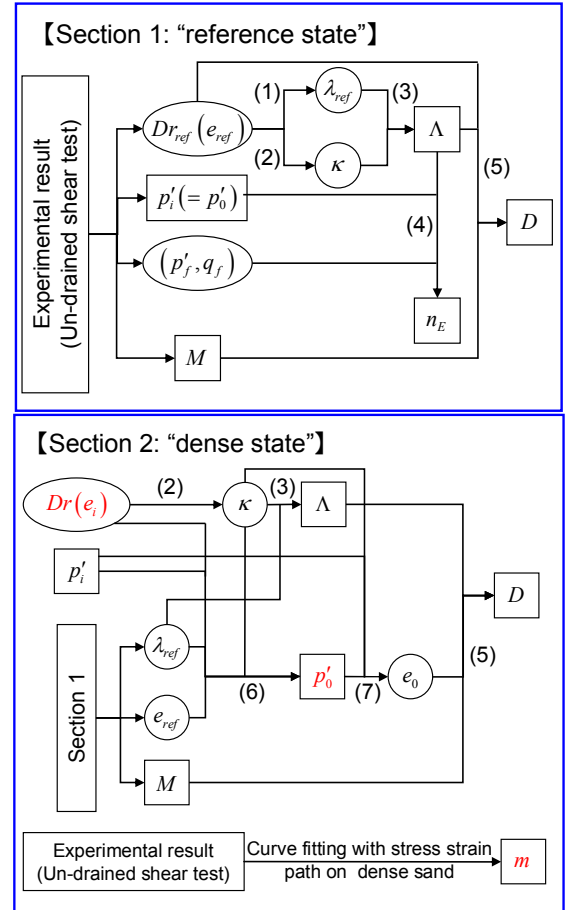
	Description	Formula
(1)	Compression index	$\lambda_{ref} = 0.313 D_r^{-0.63}$
(2)	Swelling index	$\kappa = 0.1026 D_r^{-0.45}$
(3)	Irreversible ratio	$\Lambda = 1 - \kappa/\lambda$
(4)	Fitting parameter in EC model	$n_E = \Lambda / \ln\left(p'_0/p'_f\right)$
(5)	Dilatancy parameter	$D = \lambda\Lambda / \left(M(1+e_0)\right)$
(6)	Yield stress parameter	$p'_0 = p'_i \exp\left[\left(e_{ref} - e_i\right) / \left(\lambda_{ref} - \kappa\right)\right]$
(7)	Void ratio at yielding	$e_0 = e_i - \kappa \ln\left(p'_0/p'_i\right)$

Fig.7 Flowchart of parameters determination

4. Simulated results

To validate the proposed determination method, 5 simulations of undrained shear test were carried out to compare with the reported experimental results. Herein, the simulated result for Toyoura sand is presented.

Section 1: "reference state"

According to Fig.1, Dr_{ref} is determined as 22.6%. By using flowchart defined in section 1, parameters are calculated as shown in Table (2).

Table (2)

Dr (%)	M	Λ	D	n_E	p'$_0$ (kPa)
22.6	1.2	0.4254	0.00817	1.4	294.0

Section 2: "dense state"

According to Fig.1, Dr at dense state are 26.6% and 31.2%. By using flowchart at section 2, parameters are calculated as shown in Table (3).

Table (3)

Dr (%)	M	Λ	D	n_E	m	p'$_0$ (kPa)
26.6	1.2	0.4661	0.00911	1.4	0.2	608.4
31.2		0.5030	0.01000			1251.7

Fig. 8 shows the simulated result of undrained shear test for each relative density. Each simulated result shows a good agreement with experimental results.
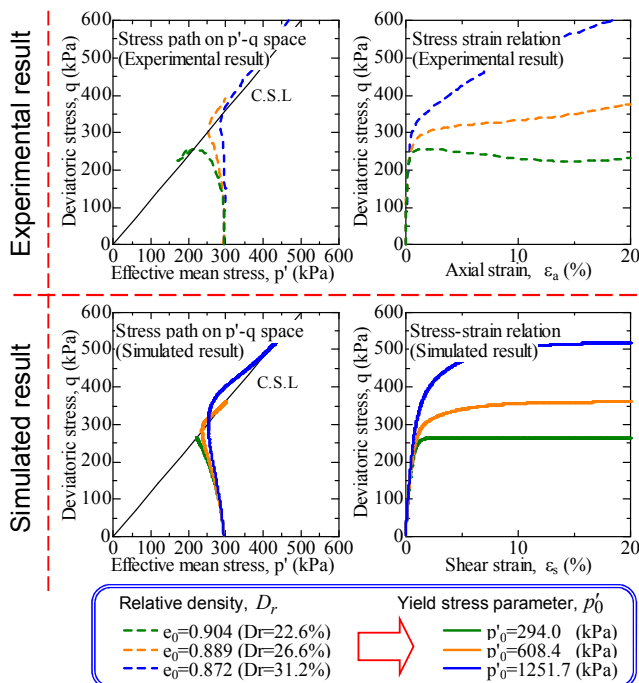

Fig.8 Simulated result
Upper: Experimental results, Lower: Simulated results
Left: Stress path on p'-q space
Right: Stress-strain relationship

5. Conclusion

In this research, simulations of undrained shear test for 5 kinds of sand are carried out. Conclusions are discussed as followed:

- The simulated results are agreed well with experimental result when the initial Dr is close to Dr_{ref}.

- However, the discrepancy increases as the degree of relative density becomes larger. The applicable range of Dr seems to be more or less Dr_{ref} +15 ～25%.

- The reason why simulated result does not coincide with experimental result, for which is very dense sand, the estimated p'_0 is significantly larger than the appropriate value.

- Simulated results of "reference state" defined in section 1 which do not coincide with experimental results were found in other kind of sand. Conceivable reasons are thought as followed: ① The constitutive model employed in this research, EC model including sub-loading surface, still has a limitation to represent the realistic behavior of sand. ② Parameter λ, κ obtained from the empirical Eq. (2) & (3), which take an important role in the proposed parameter determination method, are not coincide with whole kinds of sand.

References

1) Kato, S., Ishihara, K. and Towhata, I. (2001). Undrained shear characteristic of saturated sand under anisotropic consolidation, Soils and Foundations, Vol. 41, No. 1, 1-11.

2) Asaoka, A., Noda, T., Yamada, E., Kaneda, K. and Nakano, M. (2002). "An elasto-plastic description of two distinct volume change mechanisms of soils", Soils and Foundations, Vol.42, No.5, 47.

3) 中井健太郎,浅岡顕,中野正樹,野田利弘,金田一広 (2003).粒径分布の異なる砂の締固め特性に関する上負荷面カムクレイモデルに基づく一考察, 学術講演会講演論文集, Vol. 52 (20030516), 343-344

4) Ohno, S., Iizuka, A. and Ohta, H. (2006)：Two categories of new constitutive model derived from non-linear description of soil contractancy, Journal of Applied Mechanics, JSCE, Vol.9, pp.407-414.

5) Hashiguchi, K. (1989). Subloading surface model in unconventional plasticity, Int. J. Solids Struct., Vol.25, 917-945.

6) 阪上最一,柳浦良行,山田真一,榎本雅夫 (1995). 三軸圧縮条件下における細かな粒径の力学特性, 土木学会第 50 回年次学術講演集, Ⅲ-145, 290-291.

An applicability of DR-MEAM parameters for interfacial energy calculations

Student Number: 06M18027 Name: Takao ABE Supervisor: Kunio TAKAHASHI, Satoshi KOJIMA

DR-MEAM

DR-MEAM

1   Introduction

Modified Embedded Atom Method (MEAM) is a series of semi-empirical interatomic potential for calculating material properties of a large-scale molecular model. MEAM92, developed by Baskes [1], is very popular and parameter sets for 26 elements are published by this method. MEAMs show good applicability and reliable for bulk systems. However, the applicability of MEAMs to non-bulk systems is not well understood. Takahashi et al. has expanded the applicability of the MEAMs to non-bulk systems, which is called Dimer Reference Modified Embedded Atom Method (DR-MEAM) [3–5]. The reference structure used in this method has been changed from nearest neighbors of fcc to Dimer.

In order to calculate material properties of elements using MEAM calculations, it is needed to determine appropriate parameter set sets, e.g. equilibrium binding energy, exponential decay factors for the atomic densities, etc., included in the calculation. In DR-MEAM, parameter sets are determined by fitting both to bulk and cluster properties aiming for wide applicabilities of calculations.

For DR-MEAM parameter sets, Yin [5] and Tokumaru [4] have calculated and published parameter sets for Copper. They used different determining method: Yin focus on properties of cluster systems like Cu_3 Triangle and use results of DFT calculations, Tokumaru placed emphasis on bulk properties and using results of calculations by MEAM92. Additionally they published lists of candidate parameter sets as shown in Table 1,2. Since they published many candidate parameter sets for Cu, it is needed to select good parameter set among them into use based on applicabilities. But there are less previous works on evaluating the applicabilities of parameter sets, such as calculated results of material properties.

In this research, we calculate the stacking fault energy and relative properties using Yin's and Tokumaru's parameter sets, and evaluate their applicabilities for interfacial energy calculations.

2   Purpose of research

To evaluate the applicabilities of DR-MEAM parameter sets for interfacial energy calculations, we calculate the following 3 material properties using exiting 14 parameter sets for Cu, as shown in Table 1,2.

1. The stacking fault energy of Copper
2. Energy variation in slip deformation
3. Most stable structure among fcc, bcc and hcp

Stacking fault is a one of simple and typical interface structures. Experimental results of stacking fault energy can be easily obtained to refer. So the stacking fault energy are calculated as representative of interface. In addition I calculate energy variations in slip deformation from equilibrium structure to stacking fault. Stable structures are basic properties and relating above 2 properties, but it is not entertained enough. So it need to review.

Following sections, calculating methods and results of above 3 material properties are shown. For convenience to discuss, parameter sets in Table 1,2 are tagged with ID, as Y01-04 and T01-10.

3   Calculating method and results

3.1   Stacking fault energy

3.1.1   Atomic model for calculating Stacking Fault Energy

The stacking fault is described as a interfacial defect of stacked (111) planes of fcc. The schematic illustration of the stacking fault is shown Fig.1

The stacking fault energy γ_{sf} is defined as follows:

$$\gamma_{sf} = \frac{E_{sf} - E_0}{S} \qquad (1)$$

Here E_0 is the total energy of the equilibrium bulk structure, E_{sf} is the total energy of the structure involving the stacking fault, and S is the interface area of the stacking fault.

As the atomic modelfor calculating the stacking fault, 18 (111) planes contain 2×2 atoms per each, which stacked on $\langle 111 \rangle$ direction are used. E_{sf} is calculated as a sum of energies of these 72 atoms with slippage deformation in the middle of the stack, and E_0 is a sum of energies without defects.

For avoiding influences of surfaces on interfacial energy calculations, we apply periodic boundary conditions

Table 1: DR-MEAM parameters for Cu by Y.Yin [5]

id	E^0	R^0	a	A	$b^{(0)}$	$b^{(1)}$	$b^{(2)}$	$b^{(3)}$	$w^{(0)}$	$w^{(1)}$	$w^{(2)}$	$w^{(3)}$
Y01	1.01	2.22	4.42	0.48	3.88	3.00	3.95	2.95	1.0	1.1	2.1	1.1
Y02	1.01	2.22	4.42	0.48	3.88	3.00	3.85	2.75	1.0	1.6	2.3	1.4
Y03	1.01	2.22	4.42	0.52	3.95	4.80	3.35	3.95	1.0	3.1	2.1	2.1
Y04	1.01	2.22	4.42	0.49	3.88	4.40	2.97	2.95	1.0	2.1	2.1	1.1

Table 2: DR-MEAM parameters for Cu by K.Tokumaru [4]

id	E^0	R^0	a	A	$b^{(0)}$	$b^{(1)}$	$b^{(2)}$	$b^{(3)}$	$w^{(0)}$	$w^{(1)}$	$w^{(2)}$	$w^{(3)}$
T01	1.01	2.22	4.42	0.64	4.77	4.35	5.25	5.25	1.00	1.09	1.09	1.11
T02	1.01	2.22	4.42	0.64	4.77	4.31	5.25	5.25	1.00	1.09	1.09	1.11
T03	1.01	2.22	4.42	0.65	4.80	4.35	5.21	5.25	1.00	1.12	1.12	1.12
T04	1.01	2.22	4.42	0.65	4.80	4.35	5.25	5.25	1.00	1.12	1.12	1.12
T05	1.01	2.22	4.42	0.65	4.80	4.31	5.25	5.25	1.00	1.11	1.12	1.12
T06	1.01	2.22	4.42	0.64	4.77	4.29	5.23	5.25	1.00	1.09	1.09	1.10
T07	1.01	2.22	4.42	0.65	4.80	4.35	5.17	5.21	1.00	1.12	1.12	1.12
T08	1.01	2.22	4.42	0.64	4.77	4.33	5.25	5.25	1.00	1.12	1.09	1.09
T09	1.01	2.22	4.42	0.65	4.80	4.35	5.25	5.25	1.00	1.11	1.12	1.12
T10	1.01	2.22	4.42	0.64	4.77	4.29	5.25	5.25	1.00	1.09	1.09	1.10

in parallel directions to the interface. But the stacking fault is not periodic along the perpendicular direction to the interfacial plane. So this model has fixed boundaries on both ends of the perpendicular direction to the stacking fault. Schematic illustrations of the model for calculating the stacking fault energy are shown as Fig.2.
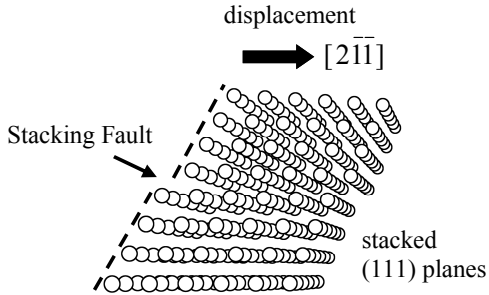

Fig. 1: Schematic illustration of the stacking fault

$R_{barrier}$ in Fig.2 is the distance between surfaces of the model and energy calculation area. To prevent influences of surfaces on calculated results of energy, $R_{barrier}$ should be chosen as large as possible. but in the aspect of calculation amount, smaller $R_{barrier}$ should be considered to reduce the number of atoms in the calculation model. From our preliminary study, $6R$, 6 times of the distance between nearest neighbor atoms in fcc, are chosen as $R_{barrier}$.

Consequently, the number of atoms in the center cell is 128. There are 4 mirror cells in each parallel directions to the interface, The total number of atoms included in the model is 10368.
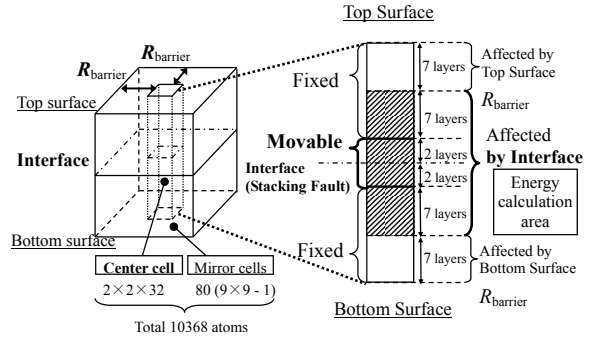

Fig. 2: Schematic Illustrations of periodic boundary conditions and fixed atom layers

3.1.2 Precisions of calculated results

In principle, we can calculate energies with expected significant figures using DR-MEAM, because equations of DR-MEAM consist of elementary functions. But limitations of numerical calculations reduce the significant figures. In calculating the stacking fault energy, the limitaions can be considered as follows: First, the significant figures of the DOUBLE PRECISION in FORTRAN is about 15 digits. Next, energy is calculated by summing interactions reduce the significant figures of the result. Because DR-MEAM has no screening functions or cut-off functions, all pair interactions between one atom and the others, i.e. 10367 atoms in this model, must be calculated. In addition, E_{sf} and E_0 are the sum of energy of 72 atoms. Therefore, the significant figures would be reduced to 8 digits. Finally subtraction in Eq.(1) decrease the significant figures to 5 digits.

3.1.3 Calculating process: initial displacement and relaxation

As shown Fig.1, the stacking fault are modelled by displacement of upper half of stacked (111) planes to $\frac{1}{3}[2\bar{1}\bar{1}]$ directions. And after this initial displacement, there are relaxation processes in which interfacial planes are reconstructed to more stable structure depending on DR-MEAM parameter sets. In the relaxation process, positions of 16 atoms upon and beneath of the stacking fault and the distance of interface, in z-direction, are changed using steepest descent method for minimize the summation energy of 72 atoms. Taking into account the precisions, calculations of steepest descent method are terminated when the amount of energy change in 1 step is less than 10^{-11} (eV). In calculation of gradient, $\Delta x = \Delta y = \Delta z = 10^{-15}$(m) are used as the difference of positions and distance to avoid local minimum.

3.1.4 Results of the stacking fault energy

Calculated values of the stacking fault energy of Copper are shown in column 1 of Table 3. Experimental values are about 30 ~ 150(mJ/m^2), depending on experimental methods, environments and etc. [2]. Calculated values of the stacking fault energy by all parameter sets agree with the experimental values. It means all parameter sets are applicable for stacking fault energy calculations.
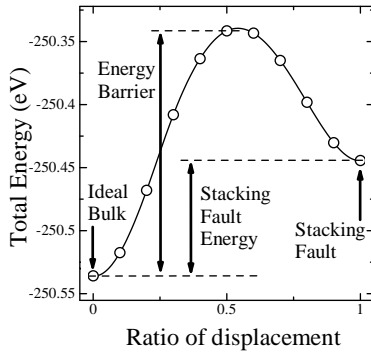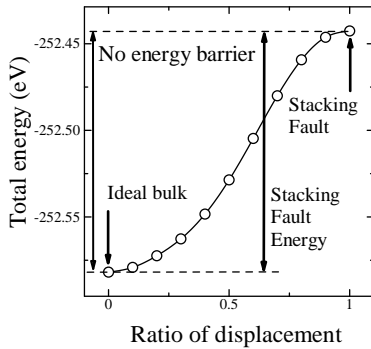

Fig. 3: Calculation result of Y01

Fig. 4: Calculation result of T01

3.2 Energy variation in slip deformation

3.2.1 Calculation model and method

The total energy of the atomic model is calculated step by step as the structure performs the slip deformation from equilibrium bulk structure to stacking fault. Regardless of initial displacement, calculation methods such as boundary conditions, the number of atoms or relaxation methods are the same with the calculations of the stacking fault energy.

3.2.2 Calculated results of energy variation

Results of energy variation are clearly classified into 2 groups, Y01-Y04 and T01-T10. As representative results, calculated results of Y01 and T01 are plotted in Fig.3, 4, respectively. The vertical axis is the total energy, and the horizontal axis is the ratio of displacement, slide to $\frac{1}{3}[2\bar{1}\bar{1}]$ direction. When the ratio equals 1.0, it is stacking fault.

The most important characteristics of these graphs is the energy barrier between ideal equilibrium and stacking fault. In other words, stacking fault is stable structure in Fig.3, but not stable in Fig. 4. However, it's difficult to discuss the applicabilities from the characteristics about the energy barrier because it's available that there are influences of relaxation conditions, i.e. no strains, no external pressures.

3.3 Stable structure of parameter sets

3.3.1 Calculation model

For determining the stable structure we calculate and compare equilibrium binding energies and distances between nearest neighbor atoms of fcc, bcc and hcp. Searching equilibrium structures, energies of structures, which have the same geometries as fcc, bcc or hcp and different distance between nearest neighbor atoms, are calculated. For avoiding the effect of surfaces we use 1289 atoms for fcc, 1243 atoms for bcc and 1261 atoms for hcp. The equilibrium distance is the distance which minimize the energy of the atom in the center of the model.

In these models we need to sum the interaction terms between the center atom and the others, about 1200 atoms. We can obtain the results of energy with the significant figures of 12 digits.

3.3.2 Results of calculating stable structure

Results of all parameter sets are shown in column 3-5 of Table 3. Here R^{eq}_{fcc} is equilibrium distance between nearest neighbor atoms of fcc, E^{eq}_{fcc} is equilibrium binding energy per atom of fcc, $\Delta E_{bcc-fcc}$ and $\Delta E_{hcp-fcc}$ are structural energy difference. If $\Delta E_{bcc-fcc} > 0$ and $\Delta E_{hcp-fcc} > 0$ then fcc is the most stable.

From experimental results, $R^{eq}_{fcc} = 2.56$(Å), $E^{eq}_{fcc} = 3.54$(eV) and the stable structure of Copper is fcc. But results of T01-T10 show that the stable structures of these parameter sets are bcc and obviously disagree with the

Table 3: Results of calculations

ID	γ_{sf} (mJ/m^2)	Energy Barrier	R_{eq}^{fcc} (m)	E_{eq}^{fcc} (eV)	$\Delta E_{bcc-fcc}$ (eV)	$\Delta E_{hcp-fcc}$ (eV)
Y01	67.310	Appear	2.5074373E-10	-3.47966495717	1.141184643E-2	1.158708470E-2
Y02	84.077	Appear	2.4948876E-10	-3.52949482140	1.368218936E-2	1.432977696E-2
Y03	147.94	Appear	2.5449382E-10	-2.95737380959	0.873000644E-2	2.633663546E-2
Y04	67.867	Appear	2.5165486E-10	-3.28715212792	1.242962083E-2	35.611491374E-2
T01	98.252	Not appear	2.5603344E-10	-3.50808138984	-2.024075324E-2	1.799456819E-2
T02	97.916	Not appear	2.5612400E-10	-3.50382063515	-2.020328896E-2	1.794176288E-2
T03	98.615	Not appear	2.5670537E-10	-3.45190782186	-2.139767365E-2	1.816454452E-2
T04	98.572	Not appear	2.5671845E-10	-3.45034029914	-2.158684096E-2	1.816041618E-2
T05	98.041	Not appear	2.5685560E-10	-3.44556520975	-2.154102968E-2	1.808228157E-2
T06	101.46	Not appear	2.5623170E-10	-3.50087565242	-2.006043339E-2	1.772346210E-2
T07	99.215	Not appear	2.5667833E-10	-3.45503249615	-2.102147897E-2	1.826629808E-2
T08	96.659	Not appear	2.5602480E-10	-3.50773976657	-2.016548630E-2	1.767586163E-2
T09	98.316	Not appear	2.5678393E-10	-3.44841020439	-2.158602665E-2	1.812724290E-2
T10	96.889	Not appear	2.5623869E-10	-3.49998253802	-2.016125718E-2	1.772127887E-2

experimental results. In addition, Y03 is doubtful, because E_{fcc}^{eq} differs from experimental results too much. Theese suggest that T01-T10 and Y03 have less applicabilities than the others.

4   Discussions

Results of stable structures show that the stable structure of T01-T10 are bcc, and imply that parameter sets by Tokumaru have less applicabilities than by Yin. The difference of stable structure should leads to the results of energy variation in slip deformations in which the stacking fault is unstable. Tokumaru had used 2 properties of bulk, equilibrium energy (eV) and equilibrium distance between nearest neighbor atoms (m) of ideal fcc bulk, and 6 properties of clusters, binding energy (eV) and distance (m) of Cu$_3$, Cu$_4$ Tetragon and Cu$_4$ Tetrahedron, as the fitting values in determining DR-MEAM parameter sets. On the other hand, Yin had used equilibrium energy (eV) , equilibrium distance between nearest neighbors (m), bulk modulus of fcc bulk (N/m^2) and binding energy (eV) distance (m) and bond angle (degree) of Cu$_3$ Liner, Cu$_3$ Triangle and Cu$_4$ Tetrahedron. Comparing these lists of properties used in determining parameters suggests that the lack of properties including dimensions relating geometries of crystallines, i.e. bulk modulus or angle, leads changing the stable structures of parameter sets by Tokumaru, which determined by fitting equilibrium energies and distances of fcc bulk and clusters, to bcc.

From another point of view, the relations between the properties used in determining parameters and the stable structures are very interesting in point of expanding applications to alloys or compounds. But for more discussions, we need another research about DR-MEAM parameters determining methods.

In parameter sets by Yin, Y03 is less applicable than the others. The equilibrium distance between nearest neighbors of Y03 are the most close to the experimental value. However, the equilibrium energy clearly disagree

with the experimental results. It confirm the predicted limitation of Yin's method in ref. [5].

There are not so large difference between Y01, Y02 and Y04. $\Delta E_{hcp-fcc}$ of Y04 are 10 times larger, but the stacking fault energy do not so different from the others. It needs other calculated results to discuss about this difference in more details.

5   Conclusion

The parameter sets by Tokumaru have less applicabilities for interfacial energy calculations than the parameter sets by Yin. One parameter set by Yin, i.e. Y03, has less applicability than the others.

Applicabilities of Y01, Y02 and Y04 for calculating interfacial energy are almost the same. For more details, it is needed to calculate other properties and evaluate them.

Reference

[1] M. Baskes. Modified embedded-atom potentials for cubic materials and impurities. *Physical Review B*, 46(5):2727–2742, 1992.

[2] P. Gallagher. The influence of alloying, temperature, and related effects on the stacking fault energy. *Metall. Trans.*, 1(9):2429–2459, 1970.

[3] K. Takahashi. Dimer Reference Embedded Atom Method. *Journal of Computational and Theoretical Nanoscience*, 1(2):221–226, 2004.

[4] K. Tokumaru. A procedure of determining parameters by adapting to the results calculated by meam'92. Master's thesis, Tokyo Institute of Technology, 2007.

[5] Y. Yingchen. *Development of a Modified Embedded Atom Method for Copper Clusters*. Doctoral dissertation, Tokyo Institute of Technology, 2006.

Application of Information and Communication Technology in Cultural World Heritage Site; Case of Luang Prabang, Lao PDR

Student Number: 06M18040   Name: Shingo ENOKI   Supervisor: Jun-ichi TAKADA, Shinobu YAMAGUCHI

1   Introduction

The World Heritage Sites attract a lot of attention in recent years. It promotes the economic development through increased tourism, but at the same time, it can cause problems such as destruction of environment due to rapid development. To control such problems and promote regional development through maximizing positive effect of becoming world heritage site, a lot of discussions have been conducted.

Among such discussion, introducing Information and Communication Technology (ICT) to promote sustainable development of world heritage site gained attention in 2004 in Lao P.D.R. Tokyo Institute of Technology in cooperation with Lao government and UNESCO conducted need assessment and five main activity components were identified based on its need assessment result. As the third year of the project, the author participated in the activities since spring 2007, particularly in the following two important activities; 1) Development of building authorization database of the local institution, 2) Setup of Internet server for the heritage database application. These activities have particular significance since they are of the urgent needs of the local government and community, and thus the successful end results are expected to contribute to the development and management of the town of Luang Prabang through introduction of ICT. At the same time, these activities are planned and implemented as a form of training of local ICT team, contributing to the local human resources development.

2   Background

2.1   Project Site

Lao People's Democratic Republic, or Laos, is a developing country located in south-east Asia. The country's population is about 6.5 million and GDP per capita is around 1,900 USD[1]. ICT infrastructure and its utilization are still under development in Laos. The project site, Luang Prabang is a regional center of northern Laos, with a population of 65,000. The town used to be the capital of kingdom which possesses variety of traditional temples and colonial buildings have been built. Luang Prabang was inscribed in the list of the world cultural heritage sites in 1995 with its valuable mixture of Lao tradition and French colonial culture in its peculiar landscape. Since the inscription, the number of tourists has continuously increased and the town has been experiencing both positive and negative effects of its development.

2.2   Project Background and Significance of the Study

Tokyo Tech has established tri-partite collaboration with UNESCO and Lao government since 2004, aiming at contributing to the sustainable regional development from technical aspect. During the initial need assessment at the site, introduction of ICT was considered as one of the most needed and missing areas of intervention at the World Heritage site of Luang Prabang. And thus, with the request of UNESCO, the leading agency of world heritage preservation and management and experts of Lao government, Tokyo Tech team together with newly established local ICT team conducted extensive needs assessment for the project. In this context, this research project is the local needs based and its development has been recognized and appreciated by the Lao government. The specific activities are planned and implemented particularly in close cooperation with MdP (La Maison du Patrimoine, Heritage House). MdP is a local governmental institution particularly responsible for the conservation and management of heritage zone of the town Luang Prabang.

2.3   Basic Needs in ICT in Luang Prabang

In earlier stage of the project, based on the result of need assessment mentioned above, the following areas of needs regarding ICT were identified. These needs are considered underlying significance to plan and implement the project activities.

Need for long-term preservation of data: In Luang Prabang, abundant useful information on heritage was accumulated during the decade in the form of photos and drawings. Such paper-based information needed to be preserved as digital data to avoid quality deterioration.

Need for an effective data utilization in daily operation: Accumulated important data was under utilized due to absence of database system. Initial effort of creating database was found at individual basis and thus, institutional database system was in serious need to promote an effective data utilization.

Need for information sharing within and among local institutions: Information sharing by introducing client/server system enables to manage the data by concentrating on to the server which was previously stored on individual PCs. This system promotes the consistency of data.

Need for information dissemination for general public: Traditionally speaking information was not to be disseminated but to be kept in the institutions. Given this situation, town of Luang Prabang had no official information center nor website for public and heritage information. This limits activities for the tourists as well as the residents, and thus promoting information dissemination was found to be urgent.

Need for local human resources development in ICT field: As one of the most urgent and important needs was human resource development at local institutions for effective and sustainable implementation of ICT activities. Such human resource was undoubtedly needed to promote locally applicable and sustainable ICT utilization.

3 Project Implementation

Given the important and urgent needs in ICT areas, the project identified five major project components as specific activities: 1) Establishment of database management system; 2) Establishing network among institutions; 3) Creating website for town of Luang Prabang; 4) Establishment and management of local ICT Center; and 5) Training of local human resources. As the third year of the project activities, and as a member of Tokyo Tech team, the author has been involved especially in the development of database system and setup of Internet server.

3.1 Summary of Initial Stage of the Activities

At the initial stage, local ICT team was organized to develop future experts in ICT field in Luang Prabang. Tokyo Tech team provided need-based various types of training. The training covered the creation of the static website, database application programming. Prototype database application was also created in the training. In order to avoid illegal use of software together with local availability, Free and Open Source Software (FOSS) were utilized in the project activities.

In addition, the first local ICT center was established in July 2006, as an important outcome of the project. In the ICT center, database application and website which are the product of series of training and the project activities are available for visitors, both to tourists and local residents.

3.2 Authorization Database

This section focuses on the creation of authorization database. Since the beginning of the project, our counterpart institution, MdP found one of the most important task is to regulate the development of the town in line with management plan of the world heritage site. In case of Luang Prabang, its landscape together with natural environment is of particular importance as the heritage site and thus, monitoring and regulating rapid changes of the landscape due to constructions and unwanted restoration is the vital task of responsible institution.

1) Significance of Authorization Process

Authorization process of MdP is an operation to give authorization for the construction or restoration of the buildings located in heritage conservation areas. The owners and/or residents who wish to build or restore the building have to apply to local government for authorization. MdP provides approvals and/or recommendations regarding building plan to fit to heritage townscape by following the heritage regulations.

2) Process of Development

The development of authorization database was conducted in close cooperation with Architecture and Urban Development section of MdP. The local ICT team has played a major role in development. Tokyo Tech team including the author has provided continuous assistance in the development process.

Workflow of authorization process was identified through discussion with relevant staff members. Then the database table structure was designed by using database normalization scheme. Subsequently, the local ICT team started development of UI and basic functions and had a periodic meeting with MdP staffs. Currently, most of the fundamental functions have been already implemented.

3) Impact of Authorization Database

The authorization database provides the way of long-term preservation of accumulated paper documents. Storage space will be also saved by digitization. In

addition, the authorization database can provide identical sets of data to the users. It also enhances the efficiency of search and analysis process with customized User Interface (UI). Creation of the database will show a significant presence of local ICT team. It also means that the team has reached certain level of skills in ICT so as to develop the mission-critical database application. Since the authorization database is a pilot database for practical operation, it is expected to stimulate further utilization of ICT for the daily operation. Moreover, this database application is expected to promote information sharing between institutions.

3.3 Internet Server Set-up

Throughout the project activities, accumulated information in MdP was compiled into the database server. However, currently the server is accessible only in ICT center due to cost and limited bandwidth of Internet. Therefore Internet server setup is highly required to disseminate the information to general public.

1) World Heritage Network

The Internet server is planned to be set up in World Heritage Network (WHN)[2].

WHN is a website for world heritage communities, site managers and other conservation professionals. The purpose of WHN is to provide a meeting place for sharing knowledge about heritage management and as we all opportunities to learn and experiment with information technologies.

2) Technical Issues

Server will be set up in following processes; 1) Software installation and configuration, 2) Data upload to WHN server, 3) Test and publishment.

Regarding process 1, there were technical issues caused by the difference in Operating System (OS) and software version of servers in WHN and ICT center. Currently the software version was upgraded and the setup process of the server in FreeBSD has been established by the author. The installation will be done by remote access through Internet.

Process 2, Data upload is another technical issue. Upload from ICT center is not realistic because the bandwidth is 64 kbps, though data size is up to 5 GB. The realistic way is high speed Internet or sending storage media such as DVD.

Since the WHN server is published in Internet, security is the important issue. To conduct a sufficient management for security, additional training will be provided to the local ICT team.

3) Impact of Internet Server Set-up

As mentioned above, it has an impact that the general public from all over the world can access to the database application. This is a powerful way to disseminate valuable information. Furthermore, through participating WHN, it is expected to share the knowledge and experiences with ICT related professionals in other world heritage sites.

4 Findings and Issues

Through intensive participation to the project activities with local ICT team in introducing ICT in heritage town of Luang Prabang, the following findings and issues may be highlighted.

Continuous training provided local ICT team members motivation to acquire skills: It is evident that the local ICT team members have high motivation in learning and acquiring new skills. They understand the importance of learning to make project activities sustainable. As leading ICT members in the town, they are trying to become the leading local human resource for ICT. It is understood that compared to the beginning of the training activities, their understanding and utilization of English has greatly improved. The team leader visited Tokyo Tech to learn more specific skills this year. The youngest member has challenged to take exam to be enrolled in Masters' program in Japanese university. These examples well illustrate high motivation for further learning.

ICT introduction to Luang Prabang receives attention and thus promotes ICT utilization: The project activity has been gaining attention from mass media and external organizations for its locally driven approach and effective utilization of ICT. For example, local brochure "Stay Another Day - Laos" has given an account of the ICT center. Many foreign organizations also visited and provided positive comments for local ICT Center. Further, as the internet environment rapidly develops in Luang Prabang, business owners pay more attention to internet as an advertisement tool. This gives the ICT team small business opportunities through creating database system for guesthouses management. Another significance of this finding is that it can promote spread of ICT utilization.

Support for Lao language is improving in ICT field: Previously, OS did not support direct input of Lao. To input Lao, additional software such as "Lao Script for Windows" was needed[4]. But recently, several Linux distributions and Windows Vista supports direct input of Lao. Lao localized office software was also developed by Science, Technology and Environment Agency (STEA), Lao government. Thus, ICT situation in Laos is rapidly improving. Under this situation, MdP staff members seem to be motivated more and more to make maximum use of the database system for their daily operation. At individual basis, it is observed that purchase and use of PC for study and business are increasing rapidly.

Language training is a must for acquisition of new technical skills: Most of the information regarding FOSS is available in Internet, only in English. Particularly updated information is seldom available in Internet in Lao and the local team learned from English documents. Although their English skills are progressing, understanding new concepts with technical expressions are still challenging. Continuous training for English along with ICT training is necessary to make maximum effects.

Instability of basic ICT infrastructure prevented smooth shift from paper-based system to computer-based system: In the town of Luang Prabang, instability of infrastructure such as electricity and Internet connectivity is often observed. Electricity failure still occurs at least once a week. Internet connectivity is not stable throughout the day. Due to such a situation, the training and other activities were delayed or suspended from time to time. This is one of the reasons that shifting paper-based system to computer-based system has difficulty. Off course, other reason such as financial difficulty causes insufficient computer installation and thus, prevents the computer-based system to be the main system. Considering this situation, combined usage of both systems seems to be realistic at current stage of Luang Prabang.

5 Discussion on Sustainability

Sustainability question of the project is always important since any kind of activities need to be transferred to the local institutions as localized activities. This section touches upon important aspects when considering sustainability of this development project. This analysis is based on experiences of the author.

Human resource aspect: Human resource development is always a key factor for project sustainability. In this project, the local ICT team was continuously trained for three years. With such experiences the team is expected to be converted as the Communication Unit of MdP. This indicates that skills of local ICT members are recognized by local institutions, and thus expected to continue forthcoming ICT related activities.

Financial aspect: To make the activity sustainable after the initial stage of the project with external support, sufficient funding is crucial. This question was considered important from the beginning of the local ICT Center operation. Income from the ICT Center covers its running cost. Besides, governmental support is also expected since the team will be kept as Communication Unit of MdP.

Technical aspect: Technical aspect such as stability of electricity, Internet connectivity and availability of computer equipments is drastically improving compared to the beginning period of the project. Further, as mentioned earlier, support of Lao language is available more and more when introducing FOSS. It is important to pay attention to the rapid change in available technology locally. Careful analysis of available infrastructure and technology, realistic decisions can be made to recommend and introduce most reasonable application.

Cultural aspect: Cultural aspect is also significant. Laotians are considered to prefer harmony avoiding argument. Therefore, it is sometimes difficult to confront with project counterpart when encountering the problems. Understanding their culture to promote a better communication is highly required for proper and sustainable implementation. Further, it is worth mentioning that Ministry of information was called as Ministry of Propaganda only until a decade ago.

6 Conclusion

Based on local need assessment, important five areas are identified in introducing ICT in the world heritage site of Luang Prabang. Among continuous research and project activities since 2004, this thesis highlighted two main activity components: 1) establishing authorization database; and 2) internet server set-up. Both components are based on urgent needs of Luang Prabang to promote its sustainable development. Further such activities are within the framework of local human resources development using FOSS for its operation. The author's intensive experience of working closely with local ICT team in developing above mentioned activities, identified major findings as well as issues to be tackled for further sustainable operation of ICT application in Luang Prabang. The study also discussed four important aspects, namely, human resources, financial, technical and cultural aspects as significant factors in introducing and sustaining ICT activities to contribute to the development and management of Luang Prabang.

References

[1] CIA, "The World Factbook -Laos-", https://www.cia.gov/library/publications/the-world-factbook/geos/la.html, last updated on Jan 17, 2008.

[2] Center for Information Media and Society, "World Heritage Network", http://worldheritagenetwork.org/

[3] "Lao Script for Windows", http://www.laoscript.net/, last updated on Dec 6, 2007.

Fundamental Research on the Hydration Reaction of Steel Slag Hydratiod Matrix (SSHM)

Student Number: 06M18056　Name: Ippei SUZUKI　Supervisor: Nobuaki OTSUKI

1. Introduction

Recently, the effective use of by-products and the depletion of natural resources such as lime stones, quartz rocks, and other aggregates are serious social issues in the engineering and construction field. With this as background, the steel slag hydratiod matrix (SSHM) was developed. It is made from steel slag and blast furnace slag fine powder (BFS) which are by-products from ironworks, and fly ash (FA) which are by-products from thermal power plants. SSHM is solidified substance that is made from slag aggregates and uses slaked lime (CH), FA and BFS as bonding materials. Because of this, its use as an alternative to concrete is examined.

There are some researches about FA and BFS because their use is increasing as a concrete mixture material. Osawa[1] made a study about the reaction ratio of FA by the selective dissolution method that uses hydrochloric acid-sodium carbonate solution. It was reported that when the FA curing temperature and fineness are high and a low replacement ratio is used, the reaction ratio increases. Kondo[2] on the other hand, made a study about the reaction ratio of BFS by the selective dissolution method that uses salicylic and methanol mixture. It is reported that when the BFS curing temperature and fineness are high and a low replacement ratio is used, the reaction ratio increases.

As stated above, the reactions of BFS and FA which are main ingredients for SSHM have temperature dependence. These materials are reported to demonstratio different strength performance depending on the curing temperature. Therefore its use in tropical regions like Southeast Asia is noteworthy. However, the researches that concerns the strength characteristics of SSHM at different curing temperature and hydration reaction mechanism in situations in which CH, FA, and BFS coexist are not yet known. Therefore it is the aim of this research to understand the influence of curing temperature to the strength characteristics of SSHM and to clarify the relationship of strength to the reaction mechanisms of the composition compounds.

2. Outline of experiments

2.1 Materials used

Table2.1 and 2.2 shows the chemical composition of FA and BFS.

CaO	SiO_2	Al_2O_3	FeO	MgO	TiO_2
17.2	38.8	27.5	9.9	2.8	3.9

Table 2.1 Chemical composition of FA (unit:%)

CaO	SiO_2	Al_2O_3	MgO	S
43.9	32.4	13.9	6.4	1.6

Table 2.2 Chemical composition of BFS (unit:%)

2.2 Method of manufacturing the test specimen

In this research, two types of specimens prepared. Table 2.3 and 2.4 shows the mix proportion of the specimens. The water/powder ratio was fixed at 40%. The mixing was done at 20 . Distilled water was used as mixing fluid. Mixing was done using two-liter mortar mixer. After all the ingredients were added, mixing was done at low speed for 30 seconds and was elevated to high speed for 150 seconds. Styrene bottles (50cc) were then filled with the mixture and sealed. After 72 hours curing time, the hardened samples were demolded and cured underwater until the target ages were reached. The curing temperature was set at three levels (20 , 30 , and 40).

After curing time was reached, a test piece was then taken from the centers of the samples and was soaked in acetone for 24 hours. This is done to stop the hydration within the test piece. The test piece was then crushed to produce powder passing through the 150μm sieve. This powder becomes the hydration test specimen.

W/P	CH	BFS	FA	W	Slag
40	86	484	163	296	1466

Table 2.3 mix proportion of specimen (For the measurement of compressive strength)

W/P	CH	BFS	FA	W
40	151	845	284	518

Table 2.4 mix proportion of specimen (For the investigation of hydration mechanism)

3. Investigation of the influence of temperature on the strength characteristics of SSHM

The compressive strength and pore structure of SSHM cured at different temperature were measured. These results are concerned from the view points of hydration products and reaction ration of composition compounds in chapter 4 and 5.

3.1 Measurement of compressive strength

The cylindrical test piece of ⌀50mm×100mm (paste + slag aggregate) is made and the compression test following JIS A1108 "Concrete compression examination" was performed. The test piece was then set up in the compression strength machine (500kN compression examination machine AYC-500P), and then applied with load (0.6±0.4 N/mm² per second). Fig 3.1 shows the results of the compression test. At

the curing temperature 20 and 30 , compressive strength increased even on the 56th day. And the case of 30 curing temperature shows higher compressive strength than the case of 20 curing temperature. However, an increase in compressive strength stagnated in the 40 curing temperature after the 14th day, and since then compressive strength values are way below the compressive strength of those cured at 20 , though the compressive strength at 1st and 3rd day is equal to the that of 30 curing temperature.

3.2 Measurement of pore structure

It is said that there are a close relationship between compressive strength and pore structure. Therefore the pore structure of SSHM on the 28th day was measured by using mercury porosimetry. Fig 3.2 shows the results. Similar to the results of compressive strength, it is confirmed that in the case 40 temperature, both amounts of total pore and minute pore size increased compared with the case of the 20 and 30 curing temperature.
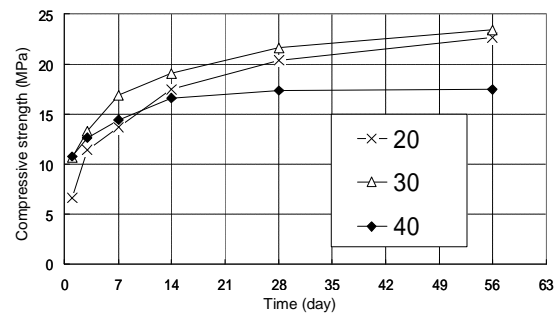
Fig 3.1 Compressive strength of SSHM at different curing temperature
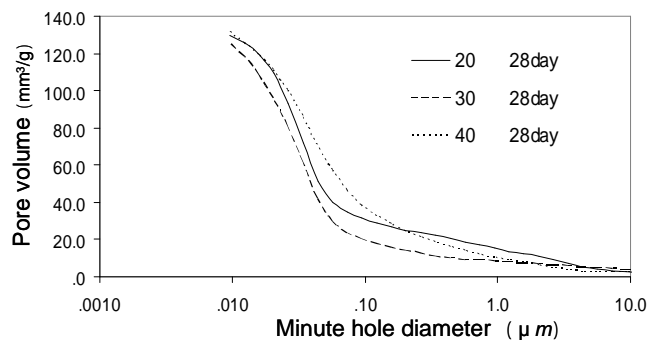

Fig 3.2 Pore structure of SSHM

4. Investigation of the hydration products of SSHM

First, to clarify the results of strength characteristics,

the hydration products of SSHM were investigated.

4.1 Identification of hydration products of SSHM.

X-ray diffraction instrument (XRD) was used for identification of the hydration products. The range of 5° 70° was done and qualitative analysis was done at operation speed 2°/min.

Fig 4.1 shows the hydration products generatiod in the SSHM. The peak that appears at about 9.1° is Ettringite 3CaO Al$_2$O$_3$ 3CaSO$_4$ 32H$_2$O , and the needle crystal generatiod by the hydration of the ordinary Portland cement. The peak that appears at about 9.9° is Monosulfate (3CaO Al$_2$O$_3$ CaSO$_4$ 12H$_2$O that shifts from Ettringite. The peak at about 11.5° is Calcium Aluminate ( ) hydratio (4CaO Al$_2$O$_3$ 13H$_2$O), and the hydration product that can be generatiod even with the hydration of the ordinary Portland cement. The peak that appears at about 10.6° is thought to be a solid solution for the Monosulfate and Calcium Aluminate ( ) hydratio [4]. Moreover, the broad peak at about 29.4° was confirmed to be C-S-H. At different curing temperature, there was no difference in the kind of the hydration products and peak intensity.

Crystal	Chemical formula	Diffraction angle (deg, CuK)
Ettringite	3CaO Al$_2$O$_3$ 3CaSO$_4$ 32H$_2$O	9.1
Monosulfate	3CaO Al$_2$O$_3$ CaSO$_4$ 12H$_2$O	9.9
C$_4$AH$_{13}$	4CaO Al$_2$O$_3$ 13H$_2$O	11.5
Solid solution C$_4$AH$_{13}$-Monosulfate	4CaO Al$_2$O$_3$ 13H$_2$O + 3CaO Al$_2$O$_3$ CaSO$_4$ 12H2O	10.6

Fig 4.1 Hydration products generatiod in SSHM

5. Investigation of the reaction ratio of composition compounds of SSHM

Next, to clarify the results of the strength characteristics, the reaction ratio of composition compounds were investigated. However, the reactions in situation in which three kinds of composition compounds coexist have never been investigated. Therefore the reaction ratio was measured by following proposed methods.

5.1 Measurement of reaction ratio of Slaked Lime

The reaction ratio of CH was determined using Differential Scanning Calorimetry (DSC). The amount of CH (calcium hydroxide) was measured by dehydration between 400 500 .

The Fig 5.1 shows the reaction ratio of CH. The reaction ratio of CH increases as curing time increases, and also as curing temperature rises.

5.2 Measurement of reaction ratio of FA

In the measurement of the reaction ratio of FA, the application of the selective dissolution method that used hydrochloric acid-sodium carbonate solution by Osawa[1] was adopted. The procedure of this method is shown below. Fig5.2 BFS, CH and the hydration products dissolved while FA was hardly dissolved using this method. Therefore the reaction ratio of FA was determined by measuring the amount of the residue extracted.

The Fig 5.3 shows the reaction ratio of FA. The reaction ratio of FA increases as curing time increases, and also as curing temperature rises.

5.3 Measurement of reaction ratio of BFS

Salicylic and methanol mixture previously mentioned are generally used for the measurement of the reaction ratio of BFS. However, because FA and BFS coexist in the SSHM mixture, therefore an accuratio fixed quantity would be difficult to be measure. Therefore in this research, the application of the method of measuring the BFS by DSC used by Imoto[3] was adopted. The enthalpy change (generation of heat) from the glass phase to Melilite (solid solution for Gehlenite and Akermanite) by crystallization happens at about 900 . This heat generation was measured by DSC.

Fig 5.4 shows the reaction ratio of BFS. At 20 and 30 curing temperature, the reaction ratio increases as curing time increases with 30 showing higher reaction ratio than 20 . However, at 40 curing temperature, the reaction ratio of BFS stagnates after 14th day and the values are less than those cured at 30 .

5.4 Influence of temperature on the reaction ratio of composition compounds.

To summarize the phenomenon happed at 40 curing temperature, it is assumed that following phenomenon happed.

At 40 curing temperature, the reaction of FA is promoted thus consuming the CH priority. The reaction of BFS making stagnated after 14th day, because CH is insufficient. Therefore, the pore structure become less tight and compressive strength

dose not increased after 14th day.

To avoid these situations, using a low heat Portland cement (LPC) which can supply Ca(OH)$_2$ for a long term as alkali stimulant is suggested.
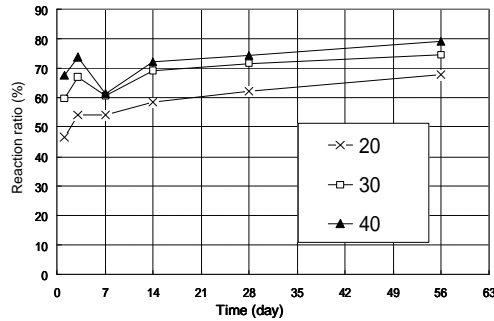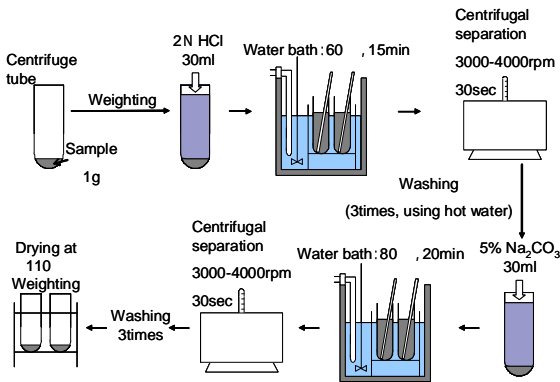

Fig 5.1 Reaction ratio of CH

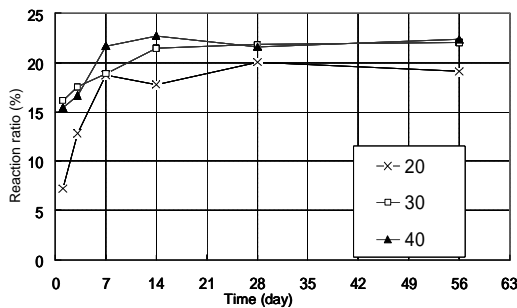Fig 5.2 Flow chart of the measurement for unreacted FA
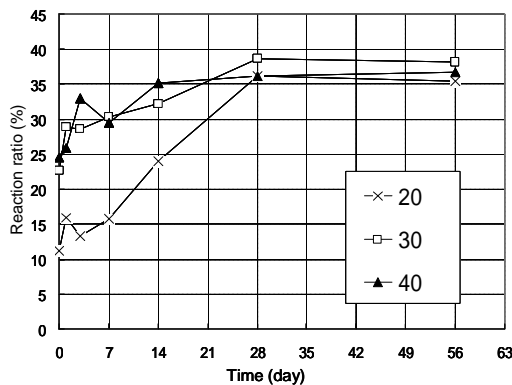

Fig 5.3 Reaction ratio of FA

Fig 5.3 Reaction ratio of BFS

6. Conclusions

[1] Compressive strength of the SSHM at curing temperature of 20 and 30 shows more than 20MPa at 28th day, and the compressive strength is increased even after the 28th day. However, compressive strength at the 40 curing temperature is not increased after the 14th day and fall well below the compressive strength of those cured at 20, though the compressive strength at the 1st and 3rd day was equal to that of 30.

[2] The hydration products generatiod in the SSHM were Ettringite, Monosulfate, Calcium Aluminate ( ) hydratio, solid solution for the Monosulfate and Calcium Aluminate ( ) hydratio, and C-S-H. At different temperature, there was no difference in the kind of hydration products.

[3] The reaction ratio of FA and CH is increased as curing temperature rises. The reaction ratio of BFS is increased at 20 and 30. The reaction ratio at 30 curing temperature shows higher value than that at 20 curing temperature. However, at 40 curing temperature, the reaction ratio is stagnated after the 14th day. The value of the reaction ratio fall well below that at 20 curing temperature after the 28th day. Therefore, at 40 curing temperature, it is recommended to use a low heat cement as alkali stimulant.

References

[1] Eiya Oosawa,: Reaction ratio of fly ash in the hydration of fly ash-cement system Cement concrete thesis collection No.53, pp.96-101, 1999

[2] Renichi Kondo:Research on quation ratio slag in fixed quantity and cement of blast furnace slag, Pottery industry society magazine Vo.77, No.2, pp.39-46, 1969

[3] Harutake Imoto:Measurement of blast furnace slag substitution ratio of cement with DSC, Concrete engineering annual thesis collection, Vol.28, No.1, Page29-34, 2006

[4] A.Lagosz, J.Malolepszy, S.Garrault Hydration of tricalcium alminate in the presence of various amounts of calcium sulphite hemihydratio, Cement and Concrete Research Vol.36, pp.1016-1022, 2006

Array Calibration Method for Angle-of-Arrival Estimation in Multipath Environment

Student Number: 06M18062   Name: Daiji TOMITA   Supervisor: Jun-ichi TAKADA

,   ,   ,   ,

.

,   ,

.   ,

.   ,

,   .

1 Introduction

Modern multi-antenna communication systems are highly dependent on the spatial characteristics of the propagation channel. Consequently, it is necessary to know a detailed knowledge of the propagation channel as a prerequisite in order to evaluate the performance of systems. This can be achieved by channel sounding assisted by high resolution estimation algorithms. By employing high resolution algorithms, one tries to estimate multipath parameters such as multipath delay, doppler shift, angle-of-arrival (AoA) and angle-of-departure (AoD). The resolution and reliability of algorithms are highly depended on the presounding calibration which aims to provide a precise knowledge of the measurement device. Obviously for the precise estimation of AoA and AoD, calibration of the antenna array has the prime importance.

In this paper, array response can be measured in an anechoic chamber using a reference wave. Since the continuous data is not available, the measurement data is interpolated by effective aperture distribution function (EADF). Later, how to apply those response data will be described.

2 Signal model

The received signal model of array antenna is shown in Eq.1.

$$\mathbf{x}(t) = \mathbf{a}(\theta, \phi)s(t) + \mathbf{n}(t) \tag{1}$$

where $\mathbf{x}(t)$ is received signal, $\mathbf{a}(\theta, \phi)$ is array response, $s(t)$ is transmitted signal and $\mathbf{n}(t)$ is noise. Equation1 means a single path model.

Multipath model is shown in Eq.2.

$$\mathbf{x}(t) = \sum_{k=1}^{K} \mathbf{a}(\theta_k, \phi_k)s_k(t) + \mathbf{n}(t) = \mathbf{A}\mathbf{s}(t) + \mathbf{n}(t) \tag{2}$$

where $\mathbf{A} = [\mathbf{a}(\theta_1, \phi_1), \mathbf{a}(\theta_2, \phi_2), \cdots, \mathbf{a}(\theta_K, \phi_K)]$, $\mathbf{s}(t) = [s_1(t), s_2(t), \cdots, s_K(t)]^T$ and K is the path number. The angles, θ and ϕ are defined as Fig.1.
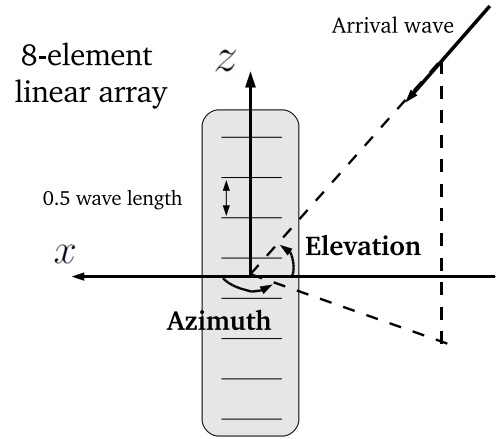
Fig. 1: The definition of AoA.

3 Sounder system

The properties of sounder system are described in this section and the parameters are shown in Table.1.

Table 1: The parameters of system

Center frequency	2.2255 [GHz]
Chip rate	30 [Mbps]
Communication system	Spread spectrum (M-sequences)
Modulation system	BPSK
Transmitter antenna	Horn antenna (10 [dBi])
Antenna input power	-7.7 [dBm]
Receiver antenna	8-element linear array
Baseband output	I, Q
Dynamic range	-60 ∼ -110 [dBm]
Array element interval	0.5 wavelength

3.1 Requirements for channel sounding

Channel model is based on measurement data. For stochastic channel models, parameter values can be obtained from extensive measurement campaigns, while for deterministic models, the prediction qualities can be checked by comparisons with measured data. The measurement property, impulse response of wireless
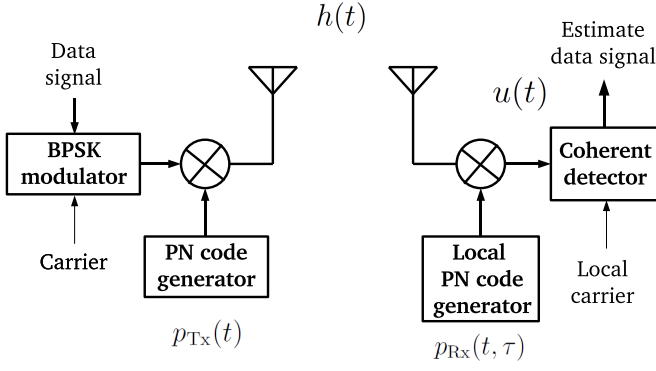
Fig. 2: Model of BPSK system[1].

Fig. 3: Transmitter antenna (Tx).

Fig. 4: Receiver antenna (Rx).

channels, better known as channel sounding, is thus a fundamental task for wireless communications[2].

3.2 Correlative sounders

A time domain measurement directly measures the impulse response. Then, the measured impulse response $\mathbf{u}(t)$ is the convolution of the true channel impulse response $\mathbf{h}(t)$ with the impulse response of the sounder $R(t, \tau)$:

$$\mathbf{u}(t) = \mathbf{h}(t) * R(t, \tau) \qquad (3)$$

where the effective sounder impulse response $R(t, \tau)$ is the convolution of the transmitted pulse shape $p_{\text{Tx}}(t)$ and the Rx filter impulse response $p_{\text{Rx}}(t, \tau)$:

$$R(t, \tau) = p_{\text{Tx}}(t) * p_{\text{Rx}}(t, \tau) \qquad (4)$$

where τ is a time shift of the sliding correlator. $R(t, \tau)$ is similar to the delta function, therefore the impulse response and the transfer function can be obtained using Eq.3. The model of sounder system is shown as Fig.2. In practice, pseudo noise (PN) sequence is utilized in this sounding sequence which is well-known from code division multiple access (CDMA) using maximum length PN-sequences created by means of a shift register with feedback[2].

3.3 Transmitter and receiver antennas

In this measurement, the horn antenna is used as transmitter antenna shown in Fig.3 and the linear array antenna is used as receiver antenna shown in Fig.4. Especially, the coordinate of receiver antenna is described in Fig.1. The receiver anttena can not estimate the horizontal angle since the vertical antenna is utilized. Therefore, linear array data need to be compound such as cylindirical antenna when the azimuth angle is required to be estimated.

4 Calibration theory

4.1 Random errors and systematic errors

Most of experimental uncertainty is due to either random errors or systematic errors. Random errors are statistical fluctuations in the measured data due to the precision limitations of the measurement device. Random errors usually result from the experimenter's ability not to take the same measurement in exactly the same way to get exactly the same number. Systematic errors, by contrast, are reproducible inaccuracies that are consistently in the same direction. Systematic errors are often due to a problem which persists throughout the entire experiment. Systematic errors of antenna array measurement can be excluded by calibration.

4.2 Necessity of the transfer function

The transfer function $\tilde{\mathbf{h}}(f)$ or impulse response $\mathbf{h}(t)$ of propagation path is one of the most fundamental and most important quantities for equalizing the distortions caused by multipath propagation. The former, transfer function is the frequency domain samples. In this measurement, a wideband signal(refer to Table.1) has many frequency bins and array response can also change with frequency. Therefore it is necessary to use transfer function as narrow band.

4.3 Array response

The MIMO (Multiple Input Multiple Output) signal model can also be described like Eq.5 using the transfer matrix $\tilde{\mathbf{H}}(f)$.

$$\tilde{\mathbf{x}}(f) = \tilde{\mathbf{H}}(f)\tilde{\mathbf{s}}(f) + \tilde{\mathbf{n}}(f) \qquad (5)$$

where $\tilde{\mathbf{x}}(f)$ is the received signal, $\tilde{\mathbf{H}}(f)$ is the transfer matrix, $\tilde{\mathbf{s}}(f)$ is the transmitted signal, and $\tilde{\mathbf{n}}(f)$ is noise
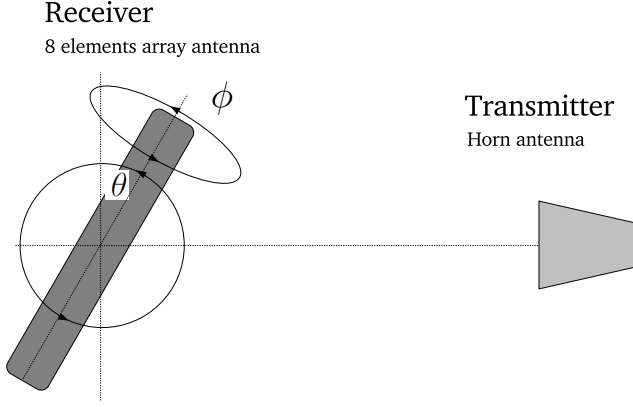
Fig. 5: Array response measurement.

in frequency domain respectively.

Then, the transfer function $\tilde{\mathbf{H}}(f)$ can be described like Eq.6.

$$\tilde{\mathbf{H}}(f) = \tilde{\zeta}(f)\tilde{\mathbf{a}}_\mathrm{t}(\theta,\phi)\tilde{\mathbf{a}}_\mathrm{r}^T(\theta,\phi) \quad (6)$$

where $\tilde{\zeta}(f)$ is the complex amplitude, $\tilde{\mathbf{a}}_\mathrm{t}(\theta,\phi)$ is the array response of transmitter antenna and $\tilde{\mathbf{a}}_\mathrm{r}(\theta,\phi)$ is the array response of receiver antenna in frequency domain. These two array responses are unique. Since, the array antenna is utilized only at receiver side in this measurement, $\tilde{\zeta}(f)$ and $\tilde{\mathbf{a}}_\mathrm{t}(\theta,\phi)$ are regarded as coefficient α like below.

$$\tilde{\mathbf{h}}(f) = \alpha\tilde{\mathbf{a}}_\mathrm{r}(\theta,\phi) + \tilde{\mathbf{n}}(f). \quad (7)$$

If SNR (Signal to Noise Ratio) is sufficiently high that noise can be neglected ($\tilde{\mathbf{n}}(f) \simeq \mathbf{0}$), the array response $\tilde{\mathbf{a}}_\mathrm{r}(\theta,\phi)$ is settled like Eq.8.

$$\tilde{\mathbf{h}}(f) \propto \tilde{\mathbf{a}}_\mathrm{r}(\theta,\phi). \quad (8)$$

Therefore, the transfer function $\tilde{\mathbf{h}}(f)$ has same effect as the array response $\tilde{\mathbf{a}}_\mathrm{r}(\theta,\phi)$[3].

4.4 Array response measurement

It is necessary to measure two dimensional array response, azimuth and elevation. The range of azimuth and elevation are 63° to 117° by 9°, −90° to 90° by 5° respectively. The schematic figure about array response measurement is described in Fig.5.

4.5 Effective aperture distribution function (EADF)

Effective aperture distribution function (EADF) represents how to model the array response of antenna arrays as a function of the azimuth and elevation angles of incoming waves. An antenna array response due to a far field source can be modeled by measuring the directional characteristic of antenna in an anechoic chamber. The array response can be measured by moving the antenna array. The array response can be expressed by an Inverse Fast Fourier Transform (IFFT) of the previous measured data. This Fourier series are referred to as the effective aperture distribution

function[4].

The l-th array array response $\tilde{\mathbf{a}}_\mathrm{r}(\theta,\phi,l)$ is stored in the matrix $\tilde{\mathbf{A}}$. The periodicity of the array response can be ensured in both dimentions. If the 2D-periodic array response defined as $\tilde{\mathbf{A}}_\mathrm{r}$ which can be as follows.

Using the discrete Fourier transform, the elevation transformation matrix can be defined as

$$\mathbf{D}_1 = \mathrm{e}^{-j2\pi\boldsymbol{f}_1\theta'} = \mathrm{e}^{-j2\pi\boldsymbol{\mu}_1\Delta f_1\mathbf{n}_1\Delta\theta'} = \mathrm{e}^{-j2\pi\boldsymbol{\mu}_1\mathbf{n}_1/N_1} \quad (9)$$

$$\Delta\theta' = \frac{2\pi}{N_1}, \quad \Delta f_1 = \frac{1}{2\pi}, \quad \theta' = \theta - \pi \quad (10)$$

$$\boldsymbol{\mu}_1^T = \mathbf{n}_1 = [-\frac{N_1}{2}, \cdots, \frac{N_1}{2} - 1] \quad (11)$$

where $N_1' = \pi/\Delta\theta + 1$, $N_2 = 2\pi/\Delta\phi$ and $N_1 = 2(N_1' - 1)$. The azimuth transformation matrix is also defined as

$$\mathbf{D}_2 = \mathrm{e}^{-j2\pi\phi\boldsymbol{f}_2} = \mathrm{e}^{-j2\pi\mathbf{n}_2\Delta\phi\boldsymbol{\mu}_2\Delta f_2} = \mathrm{e}^{-j2\pi\mathbf{n}_2\boldsymbol{\mu}_2/N_2} \quad (12)$$

$$\Delta\phi = \frac{2\pi}{N_2}, \quad \Delta f_2 = \frac{1}{2\pi} \quad (13)$$

$$\boldsymbol{\mu}_2 = \mathbf{n}_2^T = [-\frac{N_2}{2}, \cdots, \frac{N_2}{2} - 1]. \quad (14)$$

Therefore, the EADF of the l-th antenna can be obtained as

$$\mathbf{E}_l = \frac{1}{\sqrt{N_1 N_2}}\mathbf{D}_1\tilde{\mathbf{A}}_\mathrm{r}\mathbf{D}_2. \quad (15)$$

The complex exponentials of EADF after transforming to the beam domain are defined for elevation and azimuth as

$$\mathbf{d}_{\mathrm{b}1}(\theta') = \mathrm{e}^{j\boldsymbol{\mu}_1\theta'} \quad (16)$$

$$\mathbf{d}_{\mathrm{b}2}(\phi) = \mathrm{e}^{j\phi\boldsymbol{\mu}_2} \quad (17)$$

$$\boldsymbol{\mu}_1 = [-\frac{N_{\mathrm{a}1} - 1}{2}, \cdots, \frac{N_{\mathrm{a}1} - 1}{2}] \quad (18)$$

$$\boldsymbol{\mu}_2 = [-\frac{N_{\mathrm{a}2} - 1}{2}, \cdots, \frac{N_{\mathrm{a}2} - 1}{2}]^T \quad (19)$$

where $N_{\mathrm{a}1}$, $N_{\mathrm{a}2}$ are the required number of samples in $\mathbf{E}_l$.

The l-th array array response $\tilde{\mathbf{a}}_\mathrm{r}(\theta,\phi,l)$ are defined in the following equation,

$$\tilde{\mathbf{a}}_\mathrm{r}(\theta,\phi,l) = \frac{1}{\sqrt{N_{\mathrm{a}1} N_{\mathrm{a}2}}}\mathbf{d}_{\mathrm{b}1}\mathbf{E}_l\mathbf{d}_{\mathrm{b}2}. \quad (20)$$

Calibration data $\tilde{\mathbf{a}}_\mathrm{r}(\theta,\phi,l)$ is substituted for $\tilde{\mathbf{a}}_\mathrm{r}(\theta,\phi)$in Eq.7.

5 Numerical example

5.1 Calculation of the transfer function

In this research, since the wideband signal is used, the transfer function of array antenna is required. The impulse response is not ideal since the PN is utilized. Therefore, $\mathbf{u}(t)$ should be retured to the data before going to the correlator. Essentially, $\mathbf{u}(t)$ must be the impulse response $\mathbf{h}(t)$ in Eq.3, however autocorrelation function $R(t)$ is not equal to one since PN series are utilized. Therefore, Eq.1 can be transformed in frequency domain using Fourier transform.

$$\mathcal{F}\{\mathbf{u}(t)\} = \mathcal{F}\{\mathbf{h}(t) * R(t,\tau)\}$$
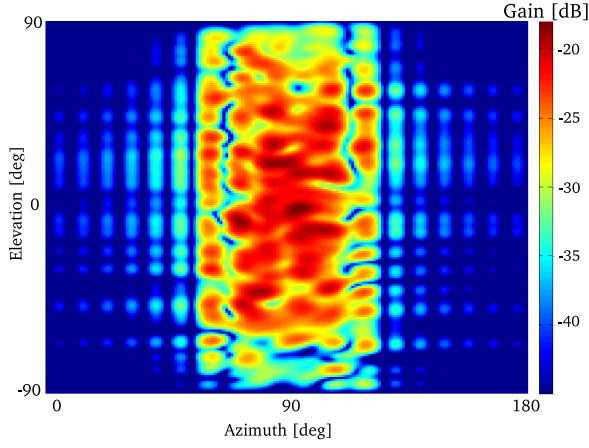$$\tilde{\mathbf{u}}(f) = \tilde{\mathbf{h}}(f)S(f). \quad (21)$$

Fig. 6: The array response after interpolation.

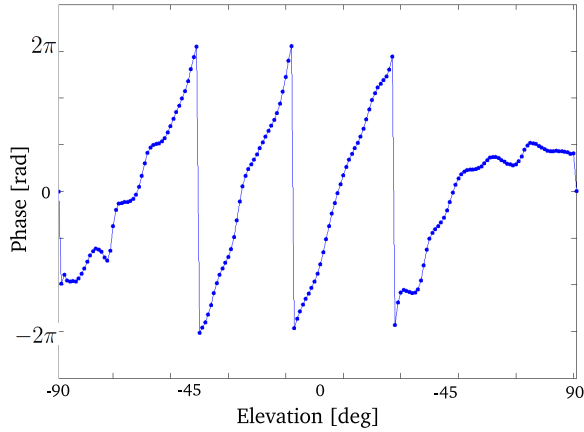Fig. 8: Beamforing output of broad side path.

Fig. 7: The phase data after interpolation

$S(f)$ is the output of back to back connection $\tilde{\mathbf{u}}_{\mathrm{dir}}(f)$. Then, the desired transfer function $\tilde{\mathbf{h}}(f)$ can be obtained when $\tilde{\mathbf{u}}(f)$ is divided by $\tilde{\mathbf{u}}_{\mathrm{dir}}(f)$.

5.2 Reconstruction of array response using EADF.

Transfer function known as the discontinuous measurement data can be transformed to the continuous function using EADF wherein the calculation was discribed in 5.1. Figure.6,7 can be calculated by the method in 4.5 and also mean desired array response of amplitude and phase respectively. These figures show EADF can be interpolated in two dimentions. Therefore, reconstruction data $\tilde{\mathbf{a}}_{\mathrm{r}}(\theta, \phi, l)$ can be substituted for $\tilde{\mathbf{a}}_{\mathrm{r}}(\theta, \phi)$ in Eq.7. When it is necessary to concentrate to small values, it can be realized by increasing the number of samples $N_{\mathrm{a}1}$, $N_{\mathrm{a}2}$ in $\mathbf{E}_l$ (refer to 4.5).

5.3 Beamforming using reconstructed array response

In this section, beamformimg result is presented. In order to provide the reliability of reconstructed array response, beamforming is implemented. Wideband signal is used in this measurement, therefore each frequency bin is processed by a narrowband processor structure. After narrowband processing on each fre-

quency bin, the beamforming output is converted to time domain by IFFT. The beamforming result is shown in Fig.8 which presents a broadside test($\phi = 90°$). The path is received in $\theta = 90°$ (elevation=0°), therefore, the interpolation methodology can be concluded to be appropriate.

6 Conclusion

The methodology of the array antenna calibration for the multipath environment was described. Since the wideband signal was used in the measurement, the array calibration was applied to each narrow band of the transfer function. Essentially, this methodology aims to be utilized for high resolution AoA estimation, therefore the angle interval in the array response measurement needs to be concentrated to very small values. However, this measurement can not be implemented since it is time consuming. Therefore, the response is measured discontinuously. Then, the discontinuous array response could be interpolated using EADF. Calibration data $\tilde{\mathbf{a}}_{\mathrm{r}}(\theta, \phi, l)$ in Fig.6 can be used for $\tilde{\mathbf{a}}_{\mathrm{r}}(\theta, \phi)$ in Eq.7. Then, the beamforming output result is shown in Fig.8 and it is proved that the reconstructed array response was appropriate to be utilized for the AoA estimation.

References

[1] S. Haykin, "Communication systems 4th edition", Wiley, 2001

[2] A. F. Molisch, "Wireless communications", John Wile & Sons Ltd, 2005

[3]   ,"   "
     .   .
          33   , 2006   10

[4] F. Belloni, A. Richter, V. Koivunen, "Reducing excess variance in beamspace methods for uniform circular array", IEEE CNF, Statistical Signal Processing, 2005 IEEE/SP 13th Workshop, pp.940-943, July.2005

Selective Catalytic Reduction of Nitrogen Monoxide
by CeO$_2$-added Nb/TiO$_2$ Catalysts

Student Number: 06M18091   Name: Megumu MAKII   Supervisor: Hirofumi HINODE

CeO$_2$ 添加 Nb/TiO$_2$ 触媒による NO 選択還元

牧井　恵

　本研究では、過剰酸素存在下でプロピレンを還元剤とする NO 選択還元を目的とした触媒の開発を行った。チタニア担持ニオブ触媒は、350°C 付近で約 60%NO を N$_2$ へと還元した。また、チタニア担持ニオブ触媒へ酸化セリウムを機械的に混合したところ、活性が向上し、320°C 付近で約 80%NO を N$_2$ へと還元できた。反応系に水蒸気が存在しても同様の転化率が得られ、水蒸気による失活は観測されなかった。NO が酸化して生成した NO$_2$ とプロピレンが反応して N$_2$ を生じる反応機構が推定される。

1. Introduction

Air pollution by nitrogen oxides (NO$_x$) emitted from mobile and stationary sources is one of serious environmental problems to be solved because NO$_x$ contribute to the formation of acid rain, global warming, photochemical smog, and depletion of ozone layer.

Lean-burn gasoline or diesel engines have highly attracted attention due to their fuel efficiency. However, the presence of excess O$_2$ in exhaust gas from these engines suppresses NO reduction activity. Therefore, a higher conversion of NO to N$_2$ in the presence of O$_2$ is desirable. Among several methods that can be used, selective catalytic reduction with hydrocarbons (HC-SCR) is currently the most studied technology for NO reduction.

For this purpose, supported noble metals, zeolite-based catalysts, and alumina-based catalysts have been reported [1-3]. Activity of various metals supported on TiO$_2$ has been investigated [4-6]. In this study, the catalytic activity of Nb-supported TiO$_2$ (Nb/TiO$_2$) catalyst and the effect of support for HC-SCR of NO by C$_3$H$_6$ in the presence of O$_2$ was investigated.

It was also suggested that NO reduction possibly occurred via the formation of NO$_2$ on M/TiO$_2$ catalysts [4-6]. Metal oxide was thought to accelerate the formation of NO$_2$. Therefore, research aiming at increasing activity of the catalyst further by adding metal oxide to catalyst has been performed. Mn$_2$O$_3$ was effective in promoting Nb/TiO$_2$ or Cu-ZSM-5 catalyst activities [5,7]. D. Niakolas et al reported that addition of CeO$_2$ on Au/Al$_2$O$_3$ resulted in the highest catalytic activity improvement when compared with several other metal oxides (Cr$_2$O$_3$, Co$_3$O$_4$, Mn$_2$O$_3$, CuO, Fe$_2$O$_3$, SnO$_2$ NiO, ZnO, and V$_2$O$_5$) [8]. Based on these reports, CeO$_2$ was selected as oxide that would be added to the catalyst, and the activity of developed catalyst was tested. CeO$_2$-added Nb/TiO$_2$ catalyst was prepared by several methods, i.e., co-impregnation, consecutive impregnation, and mechanically mixing.

2. Experimental

2.1 Materials

Nb/TiO$_2$ catalysts were prepared by impregnation method from reference catalysts supplied by Catalysis Society of Japan, which were JRC-TIO-4 (TiO$_2$④), JRC-TIO-6 (TiO$_2$⑥), and JRC-TIO-7 (TiO$_2$⑦). NH$_4$[NbO(C$_2$O$_4$)$_2$(H$_2$O)$_2$](H$_2$O)n was supplied by Companhia Brasileira de Metalurgia e Mineração (Brazil). The precursors were added into 300 mL of ion-exchanged water and stirred at room temperature for 24 hours. Then the impregnated catalyst was dried up at about 70°C for 24 hours, and calcined at 550°C for 5 hours under air flow.

(Ce+Nb)/TiO$_2$ was prepared by co-impregnation method from TiO$_2$⑦. NH$_4$[NbO(C$_2$O$_4$)$_2$(H$_2$O)$_2$](H$_2$O)n and Ce(NO$_3$)$_3$6H$_2$O were used as precursors to impregnate TiO$_2$ with Nb and Ce simultaneously.

(Ce-Nb)/TiO$_2$ was prepared by consecutive impregnation method from TiO$_2$⑦. Nb/TiO$_2$ was prepared first, then Nb/TiO$_2$ was impregnated with Ce by using Ce(NO$_3$)$_3$・6H$_2$O as precursor.

CeO$_2$ + Nb/TiO$_2$ was prepared by mixing CeO$_2$ and Nb/TiO$_2$ mechanically. CeO$_2$ was prepared by calcination of Ce(NO$_3$)$_3$・6H$_2$O (WACO Chemical Inc., Japan) at 550°C for 5 hours under air flow. CeO$_2$ and Nb/TiO$_2$ were mechanically mixed, then calcined at 550°C for 3 hours under air flow.

All catalysts were pelletized, crushed, and sieved to 0.71-1.00 mm.

2.2 Catalytic Activity Measurements

The catalytic activity was measured with a fixed-bed flow reactor by passing a reactant gas containing 1500 ppm of NO, 10% of O$_2$, 1500 ppm of C$_3$H$_6$, and helium as balance gas with a total flow rate of around 4.0 mL/s over 1.0 g of catalyst. The analysis of NO and NO$_2$ were made by NOx analyzer (NOA-305A, Shimadzu Corp.). N$_2$O and CO$_2$ were analyzed by gas chromatographs (GC-8A, Shimadzu Corp. and GC-390, GL Science Co.,

respectively). The reaction temperature was increased with a step of 50°C from 150°C to 550°C.

The influence of water vapor on the activity of catalyst was investigated by introducing 5 vol.% of water vapor during the reaction. Gas composition and analysis apparatus were the same as stated above.

2.3 XRD Characterization

Characterizations of supports and catalysts were done by XRD analysis (Multi Flex, Rigaku Corp.). The mass fraction of anatase structure of each TiO_2 support was determined by the following equation [9],

$$X_A = \frac{100}{(1+1.26 I_R/I_A)} \quad [\%]$$

where X_A is the mass fraction of anatase, and I_A and I_R are the intensities of anatase (101) reflection and rutile (110) reflection, respectively.

3. Results and Discussion

3.1 XRD Characterization

Each TiO_2 support has different mass fraction of anatase structure (Table 1). TiO_2 has three crystalline forms, which are anatase, rutile, and brookite. However, no evidence of brookite presence was observed in these supports.

Table 1 Mass fraction of TiO_2 crystalline forms of used supports

Supports	Anatase percentage [%]	Rutile percentage [%]
$TiO_2$④	74	26
$TiO_2$⑥	1	99
$TiO_2$⑦	97	3

3.2 Catalytic Activity of Nb/TiO₂

Figure 1 shows the effect of Nb loading level on the catalytic activity of Nb/TiO₂⑦ catalyst for NO reduction to N_2. Catalysts loaded with Nb showed higher catalytic activity than that of TiO_2 only, and the temperature at which conversion of NO to N_2 reached the highest value shifted to lower temperature (from 400°C to 350°C). Optimum loading level of Nb for $TiO_2$⑦ was 15wt.%, and the highest conversion of NO to N_2 for this catalyst was 63% at 350°C.

Catalysts prepared from $TiO_2$④ and $TiO_2$⑥ showed similar behavior as those prepared from $TiO_2$⑦. Optimum loading levels of Nb for $TiO_2$④ and $TiO_2$⑥ were 7wt.% and 5wt.%, respectively, and the highest conversions of NO to N_2 for these catalysts were 64% and 58%, respectively (at 350°C). Catalyst prepared from $TiO_2$④ or $TiO_2$⑦, which has mainly anatase form, showed a slightly higher catalytic activity than that

prepared from TiO_2 ⑥, which has mainly rutile form. From this result, it is concluded that the crystalline property of support (TiO_2) does not have an important effect on the catalytic activity.
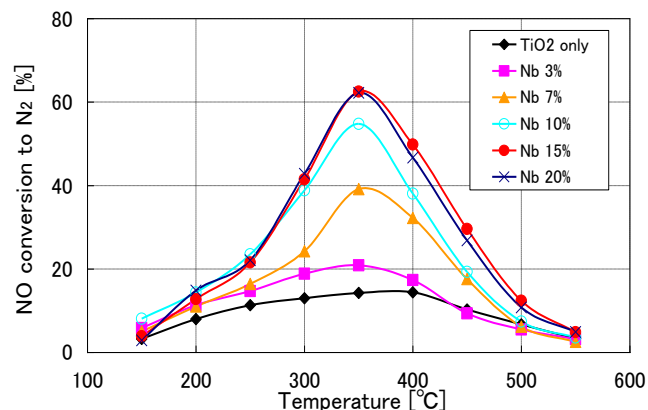

Fig. 1 Influence of Nb loading levels on Nb/TiO₂⑦

Figure 2 shows the conversion of NO to N_2, N_2O, and NO_2, and the conversion of C_3H_6 to CO_2 over Nb(15wt.%)/TiO₂⑦. All catalysts prepared from $TiO_2$④, $TiO_2$⑥, and $TiO_2$⑦ showed similar behavior. Small amount of N_2O was produced only in the low temperature region (T<400°C). NO_2 existed throughout the temperature range used in this experiment, although the concentration remained very low in the temperature at which the conversion of NO to N_2 at the highest. This result suggests that NO was oxidized to NO_2 before it subsequently reduced to N_2. Up to 550°C, the conversion of C_3H_6 to CO_2 showed similar tendency as the conversion of NO to N_2 in which the conversion increased with increasing temperature up to 350°C and decreased at higher temperature.
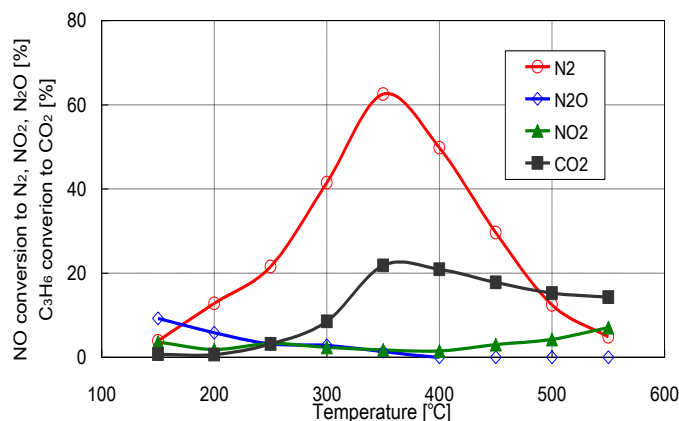
Fig. 2 NO conversion to N_2O, N_2, and NO_2, and C_3H_6 conversion to CO_2 over Nb(15wt.%)/TiO₂⑦

3.3 Catalytic Activity of (Ce+Nb)/TiO₂ and (Ce-Nb)/TiO₂

Influence of Ce loading levels on the catalytic activities were investigated for co-impregnated $(Ce+Nb)/TiO_2$ and consecutively impregnated $(Ce-Nb)/TiO_2$ catalysts, and it was found that the optimum loading level of Ce was 5 wt.% for both catalysts. However catalytic activities of $(Ce5\%+ Nb15\%)/TiO_2$ and $(Ce5\%-Nb15\%)/TiO_2$ with the best performance for co-impregnated catalyst and consecutively impregnated catalyst, respectively, could not reach that of Nb/TiO_2 only (shown in Figure 3). It is possible that CeO_2 covered Nb active site by impregnation and oxidized C_3H_6 to CO_2 before C_3H_6 could function as reductant. This could lead to the decrease of catalytic activity.
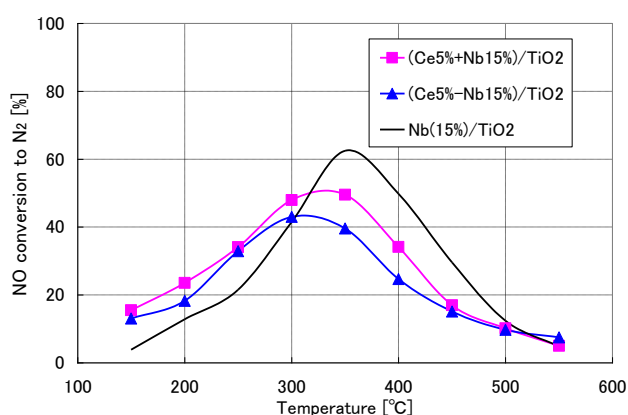
Fig. 3 Comparison of $(Ce+Nb)/TiO_2$, $(Ce-Nb)/TiO_2$, and Nb/TiO_2 catalyst activities

3.4 Catalytic Activity of CeO₂+Nb/TiO₂

Figure 4 shows the conversion of NO to N_2 over mechanically mixed $CeO_2+Nb(15wt.\%)/TiO_2$ catalyst. Catalysts mixed with CeO_2 showed higher catalytic activity than that of Nb/TiO_2. Maximum conversion of NO to N_2 reached 80% on mechanically mixed $CeO_2 + Nb/TiO_2$ (2:1), (1:1), and (1:4) catalysts. The temperature at which NO converted to N_2 reached the highest value was 350°C for $CeO_2 + Nb/TiO_2$ (1:4) catalyst, and the maximum conversion shifted to lower temperature for catalysts with higher CeO_2 ratio such as $CeO_2 + Nb/TiO_2$ (2:1) and (1:1) catalysts.

Figure 5 shows the conversion of NO to N_2, N_2O, and NO_2, and the conversion of C_3H_6 to CO_2 over mechanically mixed $CeO_2+Nb/TiO_2(1:1)$ catalyst. Small amount of N_2O was produced only in the low temperature region (T < 400°C). NO_2 formation decreased in the temperature region where the conversion of NO to N_2 was high, and increased again in higher temperature region (T > 350°C) where the conversion of NO to N_2 decreased. This result suggests that NO was oxidized to NO_2 before it was subsequently reduced to N_2. NO_2 formation was accelerated at higher temperature because of the oxidation

ability of CeO_2. Equilibrium between NO_2 and NO suppressed NO_2 formation at temperature higher than 450°C. Up to 300°C, the conversion of C_3H_6 to CO_2 showed similar tendency with the conversion of NO to N_2 in which the conversion increased with increasing temperature (mountain-shape peak). It means C_3H_6 was used as reductant to produce N_2. At temperature higher than 300°C, the conversion of C_3H_6 to CO_2 increased linearly, and then reached 100% at 400°C. In this region, C_3H_6 was probably just oxidized by reaction with O_2. Compared with Nb/TiO_2 catalyst, C_3H_6 conversion and NO_2 formation of $CeO_2+Nb/TiO_2(1:1)$ catalyst were higher. The higher formation of NO_2 was thought to be the cause of higher catalytic activity.

Additionally, the two-bed catalyst in which CeO_2 and Nb/TiO_2 were packed separately was also tested. For two-bed catalyst, CeO_2 was packed in the first bed to oxidize NO to NO_2, and Nb/TiO_2 in the second bed to reduce NO_2 to N_2 selectively. The result showed a much lower activity for the two-bed catalyst. From this finding, it was thought that NO_2 molecule in gas-phase is not the key intermediate, and the contact between CeO_2 and Nb/TiO_2 is necessary for higher activity.
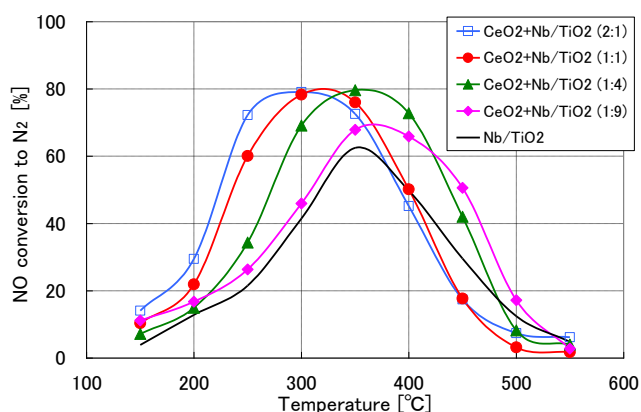

Fig.4 Influence of $CeO_2 : Nb/TiO_2$ ratio on mechanically mixed CeO_2+Nb/TiO_2 catalyst
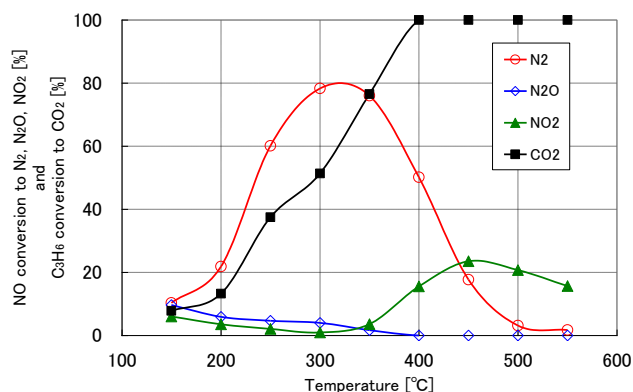
Fig. 5 NO conversion to N_2O, N_2, and NO_2, and C_3H_6 conversion to CO_2 over $CeO_2+Nb/TiO_2(1:1)$

Catalyst should be resistant to water vapor for practical use because exhaust gas normally contains water vapor. Figure 6 shows comparison of mechanically mixed $CeO_2+Nb/TiO_2(1:1)$ catalyst activity with or without the presence of water vapor. Because of the water vapor, the conversion of NO to N_2 shifted to higher temperature slightly although no serious activity inhibition was observed. For mechanically mixed Mn_2O_3+Nb/TiO_2 catalyst, it is reported that water vapor promoted the catalytic activity by the inhibition effect of water vapor on C_3H_6 oxidation [5]. However, in this experiment, C_3H_6 combustion started at lower temperature in the presence of water vapor. Water vapor caused no promotion effect on the activity over $CeO_2 +Nb/TiO_2(1:1)$ catalyst. It is also known that the effect of water vapor depends not only on the catalyst but also strongly on the reductant and the reaction temperature [10]. NO conversions to N_2O and NO_2 profile (not shown in the figure) were similar regardless of the existence of water vapor.
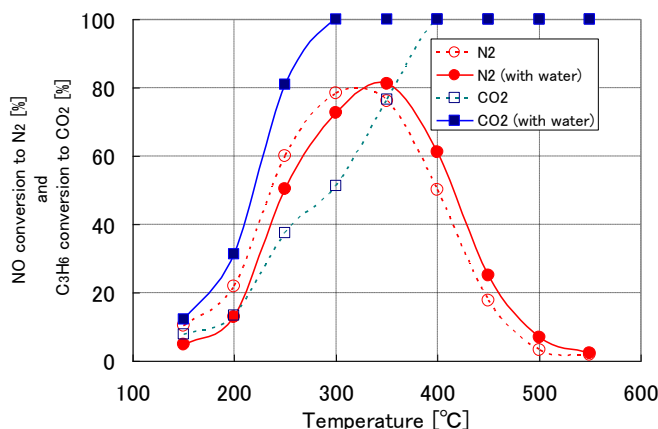
Fig.6 Influence of water vapor on mechanically mixed $CeO_2 + Nb/TiO_2$ (1:1) catalyst

4. Conclusions

Nb/TiO_2 exhibited the selective catalytic reduction of NO to N_2 by C_3H_6 in the presence of O_2. Nb loaded catalyst showed higher catalytic activity than that of TiO_2 only. The highest conversion of NO to N_2 for Nb/TiO_2 was about 60% at 350°C. The crystalline forms of TiO_2 support did not influence the activity of the catalysts significantly.

The effect of CeO_2 addition to Nb/TiO_2 catalyst depends on the preparation method. For co-impregnated $(Ce+Nb)/TiO_2$ and consecutively impregnated $(Ce-Nb)/TiO_2$ catalysts, catalytic activities were lower than that of Nb/TiO_2 catalyst. CeO_2 added by impregnation was thought to cover active site of Nb/TiO_2. On the other hand, mechanically mixed CeO_2+Nb/TiO_2 catalyst promoted Nb/TiO_2 catalyst activity and the maximum conversion of NO to N_2 was 80% at around

320°C. Although containing the same component as mechanically mixed catalyst, two-bed catalyst showed much lower activity. It means the contact between CeO_2 and Nb/TiO_2 is necessary to promote activity. The key intermediates must be short-lived compounds such as R-ONO and R-NO_2, and not the NO_2 molecule in gas-phase. Mechanically mixed $CeO_2+Nb/TiO_2(1:1)$ catalyst showed resistance against the deactivation caused by water vapor.

References

[1] M. Haneda et al; "Infrared of catalytic of NO by propene over Ag/TiO2-ZrO2," Catal. Today, **42**, 127-135 (1998)

[2] M. Iwamoto et al; "Influence of sulfur dioxide on catalytic removal of nitric oxide over copper ion-exchanged ZSM-5 zeolite," Appl. Catal., **69**, L15-L19 (1991)

[3] H. Hamada et al; "Transition metal-promoted silica and alumina catalysts for the selective reduction of NO with propane," Appl. Catal., **75**, L1-L8 (1991)

[4] J. Mitadera; Master Thesis, Tokyo Institute of Technology (2003)

[5] H. Kawai; Master Thesis, Tokyo Institute of Technology (2004)

[6] C. Tang, Master Thesis, Tokyo Institute of Technology (2006)

[7] M. Misono et al, "Reduction of nitrogen oxides with hydrocarbons catalyzed by bifunctional catalysts," Catal. Today, **38**, 157-162 (1997)

[8] D. Niakolas et al "Influence of metal oxides on the catalytic behavior of Au/Al2O3 for the selective reduction of NOx by hydrocarbons," Catal. Today, **112**, 184-187 (2006)

[9] R.A.Spurr, H.Myers; "Quantitative analysis of anatase-rutile mixtures with X-ray diffractometer," Anal. Chem., **29**, 760 (1957)

[10] K. Sato et al, "Catalytic performance of silver ion-exchanged saponite for the selective reduction of nitrogen monoxide in the presence of excess oxygen," Appl. Catal. B, **13**, 27-33 (1997)

Ca leaching Deterioration Behavior in Cement-Based Materials by electro-chemical acceleration method

Student number: 06M18100 Name: Masaya MATSUDO Supervisor: Nobuaki OTSUKI
電気的促進法によるセメント系材料の Ca 溶脱特性
松土真也

セメント系材料からの Ca 溶脱現象による劣化は 100 年単位に亘る生じるため, 促進手法が必要となる. 本研究では電気的促進法と実現象に近い拡散法を繰り返し行う手法を採用した. 本手法では促進倍率を実時間に換算できるという利点を有し, 100 年の供試体について, 本手法の妥当性が物理的変質により示されている. しかしながら, 電気的促進法は電場で Ca 溶脱を促進するため, 実際の拡散場での溶脱現象とは異なる. そのため, 電気的促進法を適用した供試体について, 化学的・物理的変質を測定し, 電気的促進法の検証を行なった. その結果, 長期的(本研究では拡散換算期間 20 年)には電気的手法は拡散場による溶脱に近づくことが示された.

1. Introduction

Deterioration due to calcium(Ca) leaching from cement-based materials progress very slowly compared to other types of deteriorations. However, in the design of special concrete structures with service life of more than a hundred years such as dams and nuclear waste repositories, it is important to consider the effect of Ca leaching from the view point of durability.

To investigate the mechanism of Ca leaching, there is a need to propose a technique. The proposed method performs repeated Electro-chemical and Diffusion Method (called EDM from here on). The merit of EDM not only accelerates deterioration of Ca leaching but also converts acceleration time into real time (called Diffusion Conversion Time). However, the electro-chemical method in EDM uses electric field for Ca leaching. So it is different from diffusion test which is closer to the real phenomenon. From those backgrounds, the objectives in this study are as follows: (1) to investigate the differences between EDM and diffusion only method in 1 year specimen. (2) to investigate the specimens deterioration after diffusion conversion time reach 20years by EDM.

2. Outline of experiment
2.1 Test methodology

In this section, the outline of the experiments for the study is presented.

The mix proportions in this study are shown in

Table.1. The specimens are cured for 56 days under sealed condition with temperature of 50℃. The specimen setup is shown in **Fig.1.**

Table.1. mix proportions

Specimen number		kg/m³				
		W	C	S	W/C	s/c
1	OPC	360	1200	1200	0.30	1.0
2	OPC	457	1062	1062	0.43	1.0
3	OPC	500	1000	1000	0.50	1.0
4	OPC	554	923	923	0.60	1.0
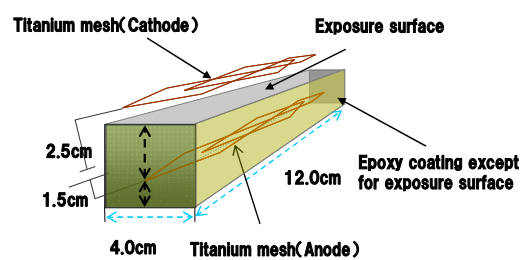
Fig.1. The images of specimens

① Specimen number2 in Table.1 was adopted for the diffusion test for 1 year. In the diffusion test, specimens are soaked in distilled water. The water is changed every two weeks, and the amount of the Ca that leached in water is measured. On the other hand, another specimen with the same proportion was accelerated by EDM. The method was changed every two weeks. Both specimens were set to have the same amount of Ca that leached out. The specimens were measured at points every

2mm from exposure surface.

② Ca leaching for the specimens in **Table.1** were accelerated by EDM. By EDM, it is assumed that leaching rate during electro-chemical method is equal to the average of the back and forth leaching rate during diffusion test. With this, the acceleration time can be converted into real time. In this study, the specimens specified in Table1 were accelerated by electro-chemical method until real time reached 20 years by EDM. The specimens were measured at points every 5mm from the exposure surface until 2cm depth is reached.

2.2. Items of investigation

Chemical deterioration was evaluated by the following methods:
・Ca leaching ratio: ion chromatography
・Ca(OH)$_2$: differential thermal analysis
・Ettringite, monosulfate, non reactive alite, belite: XRD
・Ca/Si ratio: EDX
Physical deterioration was evaluated by the following methods:
・Total Porosity
・Porosity(0.01 μ m ～ 10 μ m):Mercury press fit method
・Minute compressive strength

3. Results and Discussion
3-1. Investigation on investigate the differences between EDM and diffusion only method in 1year

Specimen number 2 in Table.1 was used to conduct both EDM and diffusion test. The two specimens were compared with each other. In the real phenomenon, it is known that Ca leaching occurs using the diffusion field, and deterioration due to Ca leaching occurs near the surface. Also, deterioration gradually progresses to the deeper part. Therefore this section focuses on the specimens that underwent EDM and diffusion methods.
The result of Vickers Hardness is shown in **Fig.2**. Near the exposure surface (0-4mm), the values of Vickers Hardness for both methods are quite similar to each other. However, in the middle part (4-20mm), EDM is stronger than diffusion specimens. In the deeper part (20-25mm), the values become similar. Thus it confirmed that in the EDM specimen, the result can be divided into three

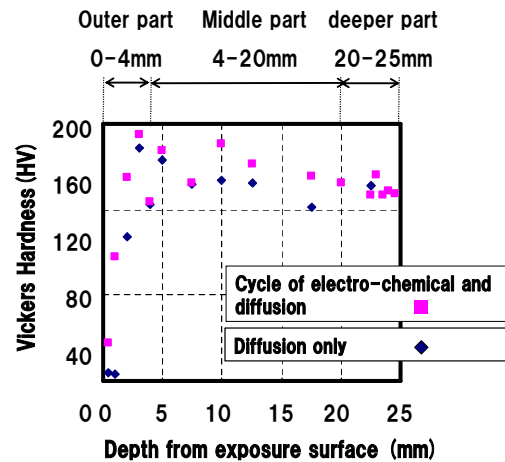parts, outer part(0-4mm), middle part(4-20mm) and deeper part(20-25mm).

Fig.2. Vickers Hardness

The results of porosity test are shown in **Fig.3, 4**. In diffusion method, at the part near the exposure surface, porosity is larger. It is the same phenomenon that is already known. However, the porosity in EDM and diffusion are different except for the outer part. In outer part, the porosity became large. And it was quite similar to the results of diffusion only specimen. However, in the middle part, the porosity became smaller than initial value. In the deeper part, total porosity was same, however a part of porosity became large.

Thus it was confirmed that the outer part can be applied with the electro-chemical method. However, in the middle and outer part, there is a need to investigate more about the specimens.
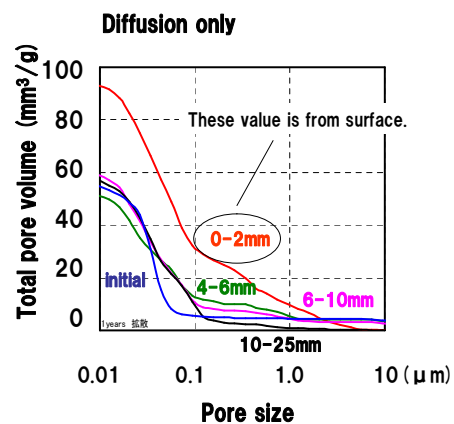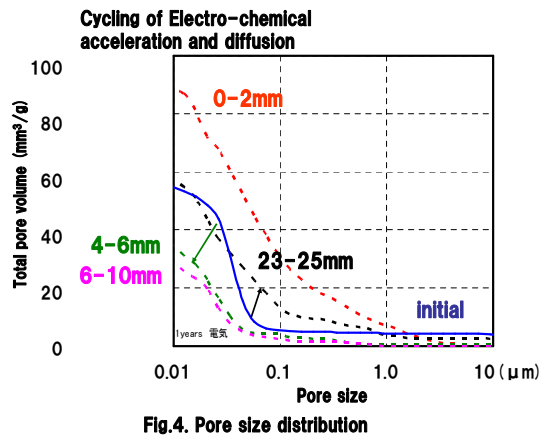

Fig.3. Pore size distribution

Fig.4. Pore size distribution

The results of reaction rate of alite and belite are shown in **Fig5**. It shows that the reaction rate using EDM at the middle part is larger than diffusion specimen. Thus in the middle part, hydration occurred and the porosity was decreased.
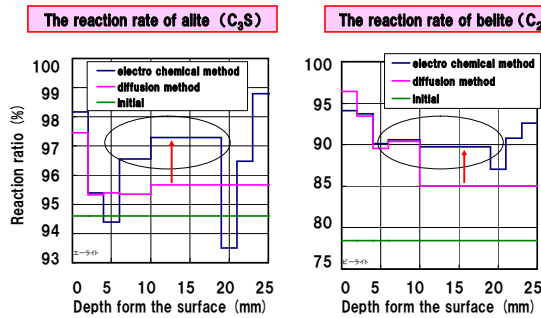

Fig.5. reaction rate of alite and belite

The results of ettringite are shown in **Fig6**. A generation of ettringite was confirmed in the deeper part. It caused the SO_4^{2-} ion to move to the anode in mortar, and monosulfate changed into ettringite in the outer part. In the outer part, it was difficult to use EDM.
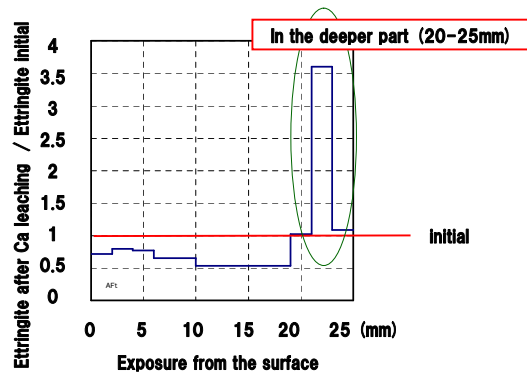
Fig.6. Ettringite

3-2. Investigation on the specimens deterioration after diffusion conversion time reaching 20years by EDM

Initially, the result between EDM and diffusion method in 1year was compared. However, actual deterioration occurs in longer time. Therefore, there is a need to confirm mortar deterioration in longer time.

The specimen in Table.1 was used to conduct the EDM until real time reached 20 years. The results of porosity are shown in **Fig.7**. Regardless of water cement ratio, the porosity is increased near the surface. These tendencies are quite similar to diffusion field which is similar to actual phenomenon
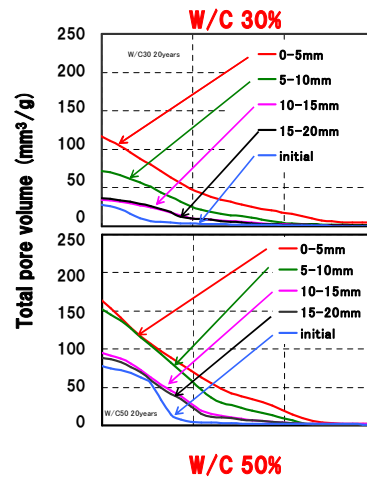
.

Fig.7 Pore size distribution

The result of porosity of mortar (W/C60%) is shown in **Fig.8**. The first one is the diffusion conversion time of 12 years and the other is 20 years. It confirmed that if time is longer, the porosity is larger near the exposure surface. The tendency is also similar to the real diffusion phenomenon.
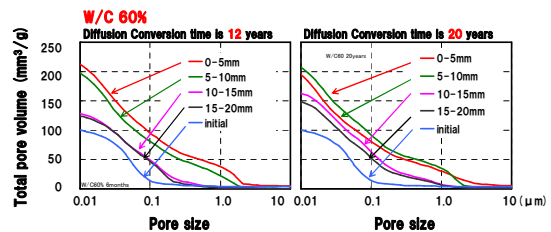

Fig.8 Pore size distribution

The hydration rate of alite and belite are shown in **Table.2**. It is confirmed that the hydration rate of both alite and belite became nearly 100% in every part. In Objective1, specimens in 1year still have

43

non reactive alite and belite. Thus hydration occurred while Ca leaching occurs. However, in 20 years specimen, alite and belite are almost exhausted. Thus it is thought that in 20 years specimen the Ca leaching deterioration becomes similar to real diffusion specimen.

Table.2. reaction rate of alite and belite

W/C 60%	0-5	5-10	10-15	15-20 (mm)
alite	99.4	99.6	99.9	99.7 (%)
belite	99.8	99.8	95.3	98.8 (%)

Other deteriorations are shown in **Fig.9**. All graphs show that near the surface, the deterioration became bigger. It was also similar to real diffusion specimen.
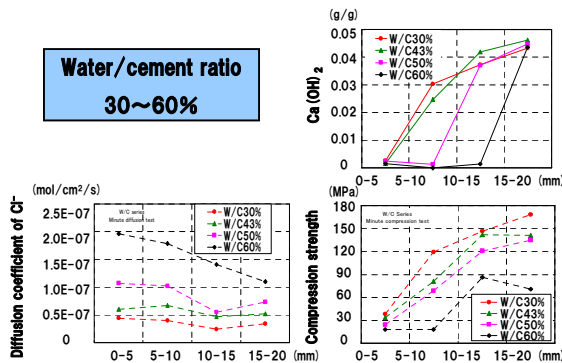

Fig.9. deteriorations due to Ca leaching

However, it is known that when Ca leaching occurred, first, chemical deterioration occurs like that of Ca(OH)$_2$. Then porosity became large and finally the deterioration of compression strength and diffusion coefficient occurs. Thus if the porosity is known, these deterioration can be predicted. Therefore the porosity is important. And in 20 years specimen, the porosity became similar to the real phenomenon, thus other deteriorations also became similar to the real phenomenon. Finally it is estimated that deterioration by EDM becomes similar to diffusion method in 20 years.

3-3. 100years specimen

The 100 years uniaxial compressive strength results of concrete deterioration due to Ca leaching are shown in **Fig.10.** The real concrete member of a waterworks structures in 100 years is compared to specimen with 101 years Ca leaching by EDM. This graph shows that the uniaxial compressive

strength of prediction specimen corresponds with the real concrete member. It is confirmed that the EDM is applicable in long term prediction.
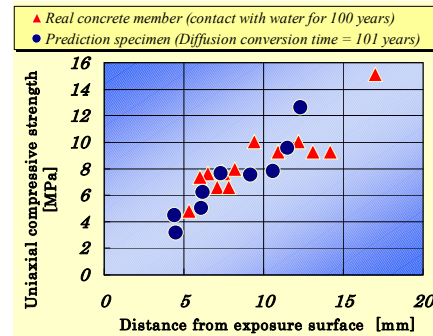
Fig.10. Uniacial compressive strength

Summary

① It was confirmed that EDM provides a close simulation of the real diffusion deterioration phenomenon near the exposure surface (0-4mm) in 1year specimen. However, in middle part (4-20mm), the hydration of alite and belite occurs during EDM. Thus the porosity is decreased compared to specimens that underwent diffusion.

② It is estimated that even in the middle part, deterioration became similar to diffusion method in 20years. The porosities of EDM were quite similar to real diffusion deterioration regardless of water cement ratio. This is evidenced by exhaustion of alite and belite. Thus it is thought that in 100years specimen by EDM, the physical deterioration became similar to real concrete members.

References

[1]Hiroshi MINAGAWA, Doctoral thesis in Tokyo Technology of Institute 2002

[2]Masaki DAIMON et, al., Cement Technique report, No.41, pp221-224, 1987.12

[3]Takeshi YAMAMOTO et, al., Report of Central Research Institute of Electric Power Industry p.2, 2007

OUTDOOR URBAN SCALE MODEL EXPERIMENTS
ON THE EFFECTS OF BUILDING GEOMETRY ON THE URBAN ATMOSPHERE

Student Number: 06M18116   Name: Takanobu MORIIZUMI   Supervisor: Manabu KANDA

屋外模型都市を用いた建物幾何形状が都市大気に及ぼす影響の検討

森泉 孝信

屋外スケールモデルを用いて都市を構成する建物の形状やその配列の違いが熱や運動量の輸送特性に与える影響を検討した．その結果，運動量輸送には建物高さの分散や密度などの幾何形状が大きく関与している一方，熱輸送は概してその影響を受けにくいことが分かった．これは熱輸送に地表面熱収支が関与していること，また粗度要素近傍での輸送メカニズムが運動量と異なることが主要因に挙げられる．

1 Introduction

Understanding the transport process of energy and scalar in the turbulent boundary layer over cities is an ongoing important issue in meteorological study. Thanks to many laboratory and numerical studies, aerodynamic properties over urban-like roughness are being systematically understood. However, these knowledge is applicable only to highly-simplified geometries i.e., arrays of uniform building, under indoor environments with less fluctuated wind and no solar radiation. Meanwhile, real cities have never such uniform surface geometry but have a lot of buildings of various shapes. Also the real cities are under much fluctuated wind field and sunlit-sunshade distribution. This might cause more complex transport process than in wind channel.

The outdoor reduced urban scale model experiment is a suitable way in order to clarify such problem. Observed data are free of various uncertainties in real cities. We can implement detailed measurement within and above the canopy with real synoptic conditions of sunshine and wind fluctuations. In addition, it is easy to change the building array and height. This study is based on the Comprehensive Outdoor Scale Model (COSMO) data.

So far basic features on regular (aligned) array of COSMO have been well investigated: the surface energy balance by Kawai and Kanda [1], and the turbulent flow characteristics and similarity (e.g. Inagaki and Kanda [2]). This paper focuses on the effect of different geometries on such features.

The purpose of this study is to investigate the effect of irregularity of building geometry both on momentum transfer and energy balance. The surface geometry focused on includes (1) the existence of building height variation, (2) distinct characteristic arrays in cities: cluster housings and detached buildings, and (3) packing density.

2 Outdoor Urban Scale Model Experiment

2.1 Site Description

COSMO is located on a portion of the campus of Nippon Institute of Technology, Saitama Prefecture, Japan (39º04'N, 139º07'E). Gentle terrain extends at least several tens of kilometers in all direction from the site. Surrounding land use is paddy field in summer and bare soil in winter.

Dominant seasonal winds are southeasterly in summer, and northwesterly in winter. The scale models were designed such that the x axes (street line) were roughly on a northwest-southeast line along which the wind direction (WD) was defined. Positive WD is a direction anticlockwise from this axis. COSMO has two different size scale models, and this paper concentrates on the smaller one because there are two advantages to use the smaller models; one is the good workability to arrange buildings in various kinds of arrays, and the other is smaller site requires smaller lot so that it is possible to compare with different surface conditions simultaneously. Two arrays of concrete blocks are set up to be compared with each other (Figure 1). Each array is on 12-m-square concrete basement. A total of three experiments were done with the combination of two different arrays.

The first experiment was to investigate the effect of building height variability on the momentum and heat transfer characteristics. Cubic, solid concrete blocks 15cm per side composed the one array (Figure 2(a)). The blocks were distributed regularly such that the plane area density (λ_p) was 0.25 which is the normal value in European residential areas. This arrangement set is called hereinafter as "HS" (Homogeneous and Standard-dense city). The other array was composed of 2 types of blocks having the same bottom size, but different heights: 15cm × 15cm × 7.5cm and 15cm × 15cm × 22.5cm (breadth-width-height) (Figure 2(b)). These blocks were distributed alternately both in the x and y direction, keeping the same λ_p and average building height (= 1H) as that of HS. This array is called hereafter "VS" (Variable heights, and Standard-dense city).

The second experiment was to investigate the effect of clustering buildings. 3-times-length blocks, 15cm × 45cm × 15cm, described the cluster housings with λ_p = 0.25 (Figure 2(c)). This is called "AS" (Apartment array of Standard density). HS was left for the comparison.

The third experiment was to investigate the effect of the difference of λ_p. One array was again HS, while the other was the similar arrangement of 15 cm cubes but with λ_p = 0.44 (Figure 2(d)) which assumes normal Japanese residential area. I call the latter setting "HD" (Homogeneous and Dense city). See Table 1 for each observation period.
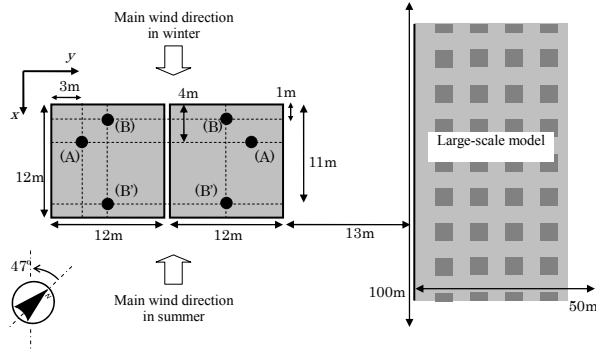
2.2 Instrumentation

Figure 1: Plane view of the two scale models and the adjacent large-scale model. (A) indicate the location of radiometers. (B) and (B') indicate the measurement points of 3 dimensional wind and vertical air temperatures in summer and winter, respectively. Large model has 1.5m cubic concrete blocks in an aligned array with λ_p being 0.25.

Figure 2: Photograph of each site; (a): HS, (b): VS, (c): AS, (d): HD.

Table 1   Observation period and the usage of two sites.

Observation period	Use of the east site	Use of the west site
'06.10/10 ~ '07.07/09	HS	VS
'07.07/17 ~ '07.09/25	HS	AS
'07.09/26 ~ '07.12/26	HS	HD

Table 2   Equipped instruments and observation conditions.

Instrument		Installed height	Sampling rate
Ultrasonic anemometer	Kaijo TR90-AH	2H (30cm)	50 Hz
Radiometer	Eko MR-40	3H (45cm)	0.5 Hz
Thermocouple (Type-E)	(my own making)	multiple points*	0.5 Hz

* 0.5H, 1H, 1.5H, 1.75H, 2H, 2.25H, 2.5H, 3H, 3.5H, 4H

Table 3   Relative magnitudes of momentum fluxes, heat fluxes, bulk transfer coefficients for momentum and heat.

		VS/HS	AS/HS	HD/HS
momentum flux	τ	1.3	1.1	0.75
sensible heat flux	Q_H	1.1	1.0	1.0
bulk transfer coefficient for momentum	C_D	2.3	1.1	0.65
bulk transfer coefficient for heat	C_H	1.6	0.84	0.85

I measured wind speeds, air temperatures, and radiations at both sites. Fluctuations of wind speeds and air temperatures were obtained by three-dimensional sonic anemometers. Upward and downward short- and long-wave radiations were measured separately by radiometers. I equipped thermocouple tower to get information of vertical air temperature. See Table 2 with detailed observational condition.

2.3 Data Processing

Momentum and sensible heat fluxes were evaluated by the eddy correlation method every 30 minutes. The data was screened out when precipitation occurred within past 24 hours, WD was more than ±45º, or mean wind speed was less than 0.1ms^{-1}, thereby optimizing data quality.

3   Results and Discussion

3.1 Fluxes and Transfer Efficiencies

Table 3 represents the observed momentum and sensible heat fluxes, and transfer efficiencies for momentum and heat in VS, AS and HD relative to those of HS.

At first we can see that a change in building geometry is the quite important factor in momentum transfer. The largest impact of all was made by the height variation in buildings, yielding much enhanced mixing. Such obvious difference can also be seen in bulk transfer coefficient for momentum (C_D); the height variant city produced much efficient momentum transfer 2.3 times larger than the canonical city's. Kanda [3] also reported that the height variation enhanced C_D by large eddy simulation (LES). The second largest impact was found in an opposite sense in the dense city. The packed buildings made the flow skim over themselves and
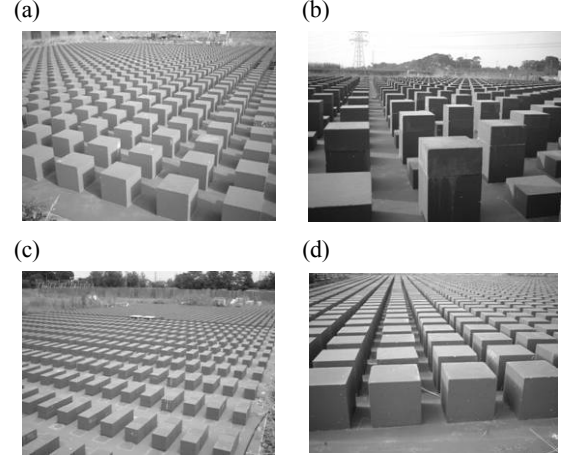
suffer less drag force. In contrast to the clear difference by height variation and densely packing, cluster buildings exhibited similar momentum transfer.

The sensible heat flux showed the least effect among the statistics given in the table. Only the height variance brought 1.1-times larger heat transfer. This augmentation is, on the one hand, a big difference from the viewpoint of thermal environment within the canopy; actually the air temperature in the height variant canopy layer becomes lower than that in homogeneous canopy in daytime due to the enhanced sensible heat transfer. However it is, on the other hand, a small change in comparison with the momentum enhancement. This reflects the fact that heat transfer is determined by the surface energy balance rather than the mixing intensity.

Although the different geometry brought similar sensible heat transfer, it is not the case for the heat transfer efficiency (C_H) because C_H is directly influenced by the mixing intensity. The height variant city showed large increase as was the case for C_D. The dense city exhibited smaller efficiency in response to the weakened momentum transfer. The apartment city showed decreased transfer efficient. One possible reason why C_H decreased despite the increase of C_D is that the wide wind street in AS lowered the height of internal layer, and the thermocouple was exposed to the
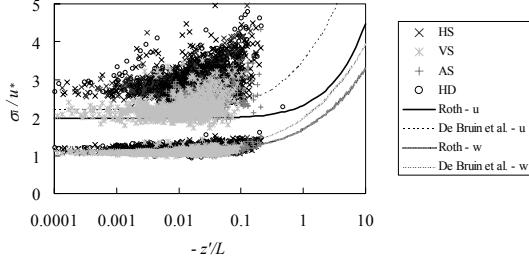
Figure 3: Normalized standard deviations of mean flow velocity (σ_u/u_*) and vertical velocity (σ_w/u_*) versus atmospheric stability. The upper and lower plots in the figure correspond to σ_u/u_* and σ_w/u_*, respectively. Two lines for respective components are the empirical fits of real urban cities (Roth [4]) and flat terrains (De Bruin et al. [5]).
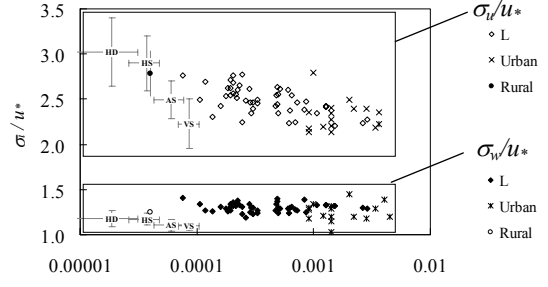

Figure 4: σ_u/u_* and σ_w/u_* against z_m/z_i. The present data (HS, VS, AS, and HD) are shown as average values with standard deviations by error bars. The other symbols are; L: large scale model experiment in COSMO, Inagaki and Kanda [2], Urban: Roth [4], Rural: Högström [6].
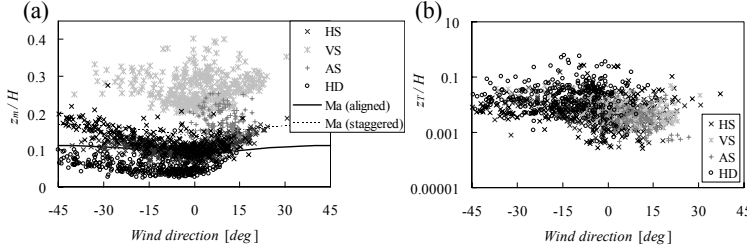

Figure 5: Roughness lengths plotted against WD; (a): for momentum, and (b): for heat. Each length was normalized by the mean building height (H). Solid and dotted lines in (a) represent the conventional morphometric relationships for the case of aligned and staggered array, respectively (Macdonald et al. [7]).
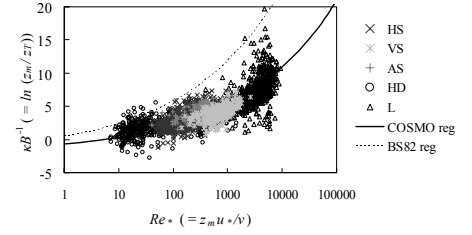

Figure 6: κB^{-1} versus Re_*. Two lines are from the theoretical relationship (equation 1); the solid curve (COSMO reg) is a fitted one by Kanda et al. [10], and the dotted curve (BS82 reg) was given by Brutsaert [9]. "L" is the results from the large-scale model in COSMO.

outer cool air. Then the temperature gradient became large, and lowered C_H.

3.2 Turbulent Statistics

The standard deviations of wind speeds normalized by friction velocity (σ_i/u_*, $i = u, v, w$) are the universal functions of atmospheric stability regardless of the surface geometry according to Monin-Obukhov Similarity Theory (MOST). However, some researchers reported that σ_u/u_* and σ_v/u_* in urban cities are somewhat different from those of another surfaces.

Figure 3 shows σ_u/u_* and σ_w/u_* against the atmospheric stability. The present data except for VS showed larger σ_u/u_* in comparison with the empirical curves given by real city (Roth [4]) and grass field (De Bruin et al. [5]) experiments. From the spectra analysis (not shown here), this enlargement was caused by the strong propagation of outer layer disturbance, which is the convective motion in atmospheric boundary layer (ABL). Inagaki and Kanda [2] succeeded in quantifying the relative importance of such outer layer disturbance to inner scale eddies in horizontal velocity fluctuations by use of z_m/z_i (z_m and z_i are the roughness length for momentum and the ABL height) in neutral conditions; σ_u/u_* gets smaller with an increase of the relative scale of z_m (i.e. the relative contribution of inner layer turbulence) (Figure 4). Four geometries implemented in this study also show such decreasing trend. For the case of VS, the instrument was closer to the higher building, and this may have made u_* larger and hence σ_u/u_* lower.

On the other hand, σ_w/u_* in all the geometries including the large scale model and real world observations agree well (Figure 3) because the outer layer contribution on vertical velocity fluctuation was moderate as seen in Figure 4 that σ_w/u_* is almost constant with various z_m/z_i.

3.3 Roughness Parameters

Figure 5 shows the evaluated roughness length for momentum (z_m) and heat (z_T) assuming MOST. We can see the systematic WD dependency of z_m; the transfer efficiency of momentum is variable with respect to the geometrical change. Two lines involved are the conventional morphometric relationship for arrays of aligned and staggered cubes (Macdonald et al. [7]). A staggered array has not been tested in COSMO, the present result of HS with WD = 45° can approximate a staggered array with WD = 0°. z_m/H in HS seems to shift from one branch (aligned array) to the other (staggered), so that the behavior of estimated z_m is reasonable. The graph also shows the relative difference of z_m in four sites. The height variant city exhibits much higher z_m so that the momentum transport could be enhanced. The dense city has smaller value reflecting the weakness of drag force.

On the other hand, such WD dependency and geometrical difference can not be found in z_T. All the results have large scatters so that it is difficult to prescribe z_T with respect to certain geometry. However, using constant z_T on numerical simulation would result in significant errors of heat flux (e.g. Kawai et al. [8]).

Brutsaert [9] theoretically related the relative ratio between z_m and z_T to the roughness Reynolds number Re_* ($= z_m u_*/\nu$, ν: the kinematic viscosity):

$$\kappa B^{-1} = a \cdot Re_*^{0.25} - 2.0 , \qquad (1)$$

where κB^{-1} is the logarithm of the ratio between z_m and z_T ($= \ln(z_m/z_T)$), and a is an empirical constant. Figure 6 represents κB^{-1} against Re_* in the case of HS, VS, AS, and HD together with the results of large scale model experiment. The dotted and solid lines are from equation 1 with different coefficients a; one is the original curve with $a = 2.46$ by Brutsaert, and the other is a best-fit curve with $a = 1.29$ from the large scale model and HS data (not the present data; Kanda et al. [10]). We can find the good agreement of all the present data (HS, VS, AS, and HD) and the large scale model data on Kanda et al.'s regression curve. The reason why the COSMO data don't follow the Brutsaert's curve is that (1) as Brutsaert wrote in his paper, his estimate was based on the data only cover Re_* smaller than 1000, and it may not be valid for very rough surfaces with z_m of the order of a meter, and that (2) the boundary conditions were different from the COSMO; Brutsaert determined the numerical constant a with the data over water surfaces. In addition, Kawai et al. [11] investigated the discrepancy between real city data and the regression curve (equation 1) with $a = 1.29$, and revealed that a was variable with respect to the vegetation ratio. Therefore, the use of equation 1 in UCM will improve urban energy balance estimation.

4 Conclusions

The effect of irregularity of building geometry, including (1) the existence of building height variation, (2) distinct characteristic arrays in cities: cluster housings and detached buildings, and (3) packing density, was investigated using the unique dataset of COSMO. The main findings are as follows;

(1) The momentum flux was obviously affected by the surface geometry. The sensible heat flux, in contrast, was less affected due to the limitation of available energy stored in the concrete materials. There exists a trade-off relationship between the enhancement (suppression) of turbulent mixing (i.e. momentum flux) and the descent (ascent) of the surface temperature. Consequently, the offset of these two factors led to the less sensitive sensible heat flux.

(2) The bulk transfer coefficients both for momentum and heat showed large variation with geometry. In particular, height variation made much efficient transport and hence it is preferable to diffuse particles (e.g. air pollutants). On the other hand, detached building arrays and apartment ones exhibited similar transfer characteristics.

(3) The outer scale turbulence influenced on all of the COSMO data used in this analysis, resulting in the departure from MOST. It was confirmed that the relative scale of outer and inner scale eddy can be the good index to estimate the inner-scaled horizontal wind velocity fluctuations.

(4) The ratio of roughness length for momentum to heat was well prescribed by the roughness Reynolds number regardless of the building geometry. Thus combining this relationship with UCM and MOST seems the better way for urban energy balance prediction.

References

[1] Kawai, T., and M. Kanda, "Energy balance obtained from comprehensive outdoor scale model experiment (I) Basic feature of the energy balance," *J. Appl. Meteor.* (submitted)

[2] Inagaki, A., and M. Kanda, "Turbulent flow similarity over an outdoor reduced urban model," *J. Fluid Mech.* (in revision)

[3] Kanda, M., "Large eddy simulations on the effects of surface geometry of building arrays on turbulent organized structures," *Bound.-Layer Meteor.*, vol.118, pp.151-168, 2006.

[4] Roth, M., "Review of atmospheric turbulence over cities," *Quart. J. Roy. Meteor. Soc.*, vol.126, pp.941-990, 2000.

[5] De Bruin, H. A. R., W. Kohsiek, and B. J. J. M. Van Den Hurk, "A verification of some methods to determine the fluxes of momentum, sensible heat, and water vapour using standard deviation and structure parameter of scalar meteorological quantities," *Bound.-Layer Meteor.*, vol.63, pp.231-257, 1993.

[6] Högström, U., "Analysis of turbulence structure in the surface layer with a modified similarity formulation for near neutral conditions," *J. Atmos. Sci.*, vol.47, pp.1949-1972, 1990.

[7] MacDonald, R. W., R. F. Griffiths, and D. J. Hall, "An improved method for the estimation of surface roughness of obstacle arrays," *Atmos. Environ.*, vol.32, pp.1857-1864, 1998.

[8] Kawai, T., M. Kanda, K. Narita, and A. Hagishima, "Validation of a numerical model for urban energy-exchange using outdoor scale-model measurements," *Int. J. Climatol.*, vol.27, pp.1931-1942, 2007.

[9] Brutsaert, W., "Evaporation into the Atmosphere," D. Reidel Pub Co., 1982.

[10] Kanda, M., M. Kanega, T. Kawai, R. Moriwaki, and H. Sugawara, "Roughness lengths for momentum and heat derived from outdoor urban scale models," *J. Appl. Meteor.*, vol.46, pp.1067-1079, 2007.

[11] Kawai, T., K. R. Mohammad, and M. Kanda, "Evaluation of a simple urban energy balance model using one-year observed fluxes from two different cities," *J. Appl. Meteor.* (submitted)

Pattern Recognition by Kernel Wiener Filter

Student Number: 06M18122   Name: Hirokazu YOSHINO   Supervisor: Yukihiko YAMASHITA

1   Introduction

Inverse problem is used in various fields such as engineering, science and medical science. In the problem we estimate an origin from its results or responses. Especially linear inverse problem is widely applied to many difficulties in, for example, restoration of deteriorated signals or images.

Let $\mathcal{H}_s$ be an original signal space and $\mathcal{H}_o$ be an observed signal space. f denotes an original signal and it is transformed into an element in the observed space by an observation operator $A \in \mathscr{B}(\mathcal{H}_s, \mathcal{H}_o)$. Then a noise n is added to the element and we can obtain an observed signal $g = Af + n$ in $\mathcal{H}_o$. Here, $\mathscr{B}(\mathcal{H}_s, \mathcal{H}_o)$ is the total set of the bounded linear operators between $\mathcal{H}_s$ and $\mathcal{H}_o$ and X denotes an estimation operator. An estimated signal of f is denoted by $\hat{f}$. Then, this model is formulated as below.

$$g = Af + n \qquad (1)$$
$$\hat{f} = Xg \qquad (2)$$

It can be illustrated by Figure 1. Linear inverse problem is to find the best-estimated signal $\hat{f}$ from the observed signal g, in other words to acquire the suitable X which gives the best-estimated signal $\hat{f}$. A variety of techniques for inverse problem are proposed. Among them Wiener filter (WF) [1] is defined as a linear operator that minimizes the squared error between f and $\hat{f}$ averaged over f and n. Many other criteria evaluating the accuracy of the restored image in $\mathcal{H}_o$ are adopted though, WF directly compares f and $\hat{f}$ in $\mathcal{H}_s$. Moreover the structure of WF is so simple that it can be widely applied to a variety of fields.
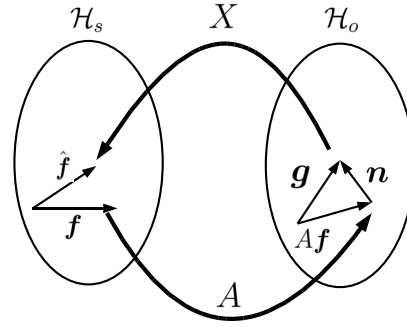

Fig. 1: Inverse problem

Recently the kernel method is intensively researched in the field of pattern recognition. In that method, vectors in the input space are mapped into a high dimensional vector space by a nonlinear mapping function. We can linearly handle them in that space instead of non-linearly in the input space. By kernel trick we just need to calculate in a space of which dimension is the number of samples. Therefore, the kernel method enables us to cut the total amount of the calculations and lets us apply it to many problems. However we can apply the kernel trick only to nonlinear functions that are derived from Mercer kernels.

In this paper, we apply the kernel Wiener filter (KWF) [2, 3] to the pattern recognition problem. We regard a pattern as an observed signal and provide an identical original vector with the patterns belonging to the same class. This model is shown in Figure 2. In Figure 2, $f_t^{\dagger}$ denotes the original signal of the t-th class and g_{ij} denotes the j-th observed signal belonging to the i-th class.
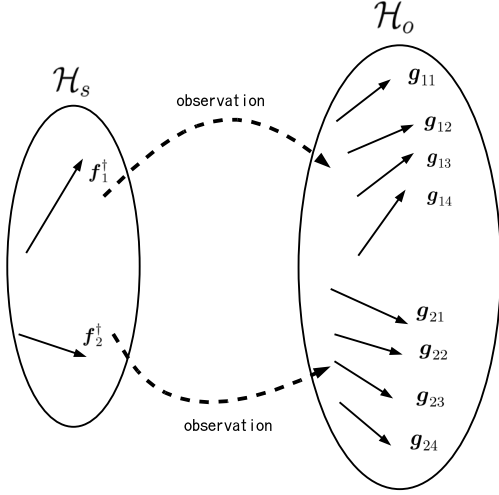
Fig. 2: Observation of original signals

Also applying first-order approximation of Taylor expansion to the nonlinear function in observed signal space, we propose a regularization method based on the distance in the observed signal space.

We clarify the advantages by experimental results and make it clear that changing properly the value of kernel function in $\mathscr{H}_s$ improves its generalization ability.

2 Wiener Filter(WF)

WF is defined as a linear operator that minimizes the squared error between an original signal f and a restored signal $\hat{f}$ averaged over f and noise n. E_f and E_n denote the average over f and n, respectively. Let the inner product of f and g be $\langle f, g \rangle$ and the norm of f be $\|f\| = \sqrt{\langle f, f \rangle}$. WF is formulated as a liner operator that minimizes the following criterion J_{WF}.

$$J_{WF} = E_f E_n \|\hat{f} - f\|^2 = E_f E_n \|Xg - f\|^2. \quad (3)$$

Let R and Q be correlation operators of a original signal and a noise, respectively.

$$R = E_f \left(f f^T \right), \quad (4)$$

$$Q = E_n \left(n n^T \right). \quad (5)$$

Here, A^T denotes the transposition of a vector or a matrix A. When an operator B satisfies $ABA = A \quad BAB = B \quad (AB)^T = AB$ and $(BA)^T = BA$, B is called the Moore-Penrose generalized inverse matrix of A and it's denoted by $A^\dagger$. Under these mathematical preparations, WF is

described as eq.(6) when the original signal and noise are uncorrelated.

$$X_{WF} = RA^T (ARA^T + Q)^\dagger. \quad (6)$$

3 Kernel Wiener Filter

The signals in a space are mapped by a nonlinear function Φ, which is derived from a Mercer kernel, into a reproducing kernel Hilbert Space (RKHS). This space is called the feature space. Generally speaking the feature space has a higher dimension than the original space. In this paper we use the following Gausian kernel function $k(x,y)$ as a Mercer kernel for the observed signal space.

$$k(x,y) = \exp\left(-\gamma \|x-y\|^2\right) \qquad (\gamma > 0), \quad (7)$$

and also we define γ as a positive parameter.

We provide the framework of inverse problem by the kernel method. Let Φ_s be a nonlinear function from the original signal space to its feature space $\mathscr{F}_s$ and also Φ_o be a nonlinear function from the observed signal space to its feature space $\mathscr{F}_o$. This model is shown in Figure 3.
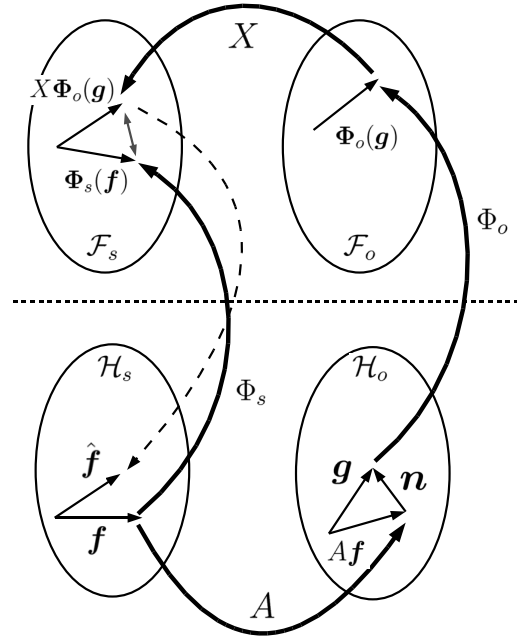

Fig. 3: Inverse problem between $\mathscr{F}_s$ and $\mathscr{F}_o$

X is a restoration operator between $\mathscr{F}_s$ and $\mathscr{F}_o$. Its estimated signal is given by $X\Phi_o(g)$. f is provided by using $X\Phi_o(g)$.

3.1 Proposed Method 1: KWF-1

We define KWF-1. Here we assume that each sample consists of both an original signal f_i and an observed signal g_i $(i = 1, 2, \ldots, L)$. KWF-1 X_1 minimizes the sum of squared errors between $\Phi_o(f_i)$ and its restored signal $X_1\Phi_o(g_i)$. Then X_1 minimizes the following criterion J_{KWF1}.

$$J_{KWF1} = \frac{1}{L}\sum_{i=1}^{L}\|\Phi_s(f_i) - X_1\Phi_o(g_i)\|^2. \quad (8)$$

From eq.(8), X_1 can be solved as follows.

$$X_1 = \sum_{i=1}^{L}\Phi_s(f_i)\Phi_o(g_i)^T\left[\sum_{j=1}^{L}\Phi_o(g_j)\Phi_o(g_j)^T\right]^\dagger. \quad (9)$$

3.2 Proposed Method 2: KWF-2

We introduce a regularization method based on the distance of $\mathcal{H}_o$, which is an N dimensional vector space, for the purpose of avoiding over fitting to learning data. Then we assume that virtual noises $e_1, \ldots, e_L$ are added to g_i $(i = 1, \ldots, L)$ respectively and propose the following criterion to minimize.

$$J_{KWF2} = E_{e_1, \ldots, e_L}\sum_{i=1}^{L}\|\Phi_s(f_i) - X_2\Phi_o(g_i + e_i)\|^2. \quad (10)$$

We assume that the observed signals and e_i are independent, the average on each element of e_i is 0 and e_i is uncorrelated with each other. Furthermore, we assume that the variance-covariance matrix of e_i $(\forall i)$ is given by the same matrix $Q = \text{diag}(\sigma_1^2, \sigma_2^2, \ldots, \sigma_N^2)$. Let the j-th element of a vector x_i be x_{ij}.

In the original kernel method, sample average over the virtual noises has to be calculated because of the nonlinear function Φ_o. It needs huge calculation cost even if the kernel trick is applied. Here, we assume that g_i is much larger than e_i and apply the following first-order approximation to eq.(10) to simplify the the calculation [4].

$$\Phi_o(g_i + e_i) \simeq \Phi_o(g_i) + \sum_{j=1}^{N}e_{ij}\phi_{o,j}(g_i), \quad (11)$$

where $\phi_{o,l}(g_i)$ is defined by

$$\phi_{o,l}(g_i) \equiv \frac{\partial\Phi_o(g_i)}{\partial g_{il}}. \quad (12)$$

For both $\phi_{o,l}(g)$ and $\Phi_o(g)$ has the same dimension, then it's difficult to calculate them directory. Here, we

define inner products concerning with above two nonlinear functions by introducing derivation of the kernel function. Then $k_{o,i}(x,y)$, $k_o^i(x,y)$ and $k_{o,ij}(x,y)$ are denoted by

$$k_{o,i}(x,y) \equiv \langle\Phi_o(x), \phi_{o,i}(y)\rangle = \frac{\partial}{\partial y_i}k_o(x,y), \quad (13)$$

$$k_o^i(x,y) \equiv \langle\phi_{o,i}(x), \Phi_o(y)\rangle = \frac{\partial}{\partial x_i}k_o(x,y), \quad (14)$$

$$k_{o,ij}(x,y) \equiv \langle\phi_{o,i}(x), \phi_{o,j}(y)\rangle = \frac{\partial^2}{\partial x_i\partial y_j}k_o(x,y). \quad (15)$$

Eq.(10) and a decision function have to be expressed by the kernel function and its differential forms without Φ_s, Φ_o and $\phi_{o,i}$.

We can define X_2 by eq.(16) from the derivations of the kernel function.

$$X_2 = \sum_{i=1}^{L}\sum_{j=1}^{L(N+1)}\alpha_{ij}(\Phi_s(f_i)\otimes\overline{v_j}) \quad (\alpha_{ij} \in R), \quad (16)$$

where

$$v_i = \begin{cases} \Phi_o(g_i) & (1 \leq i \leq L) \\ \varphi_{i-L} & (L+1 \leq i \leq L(N+1)) \end{cases}, \quad (17)$$

$$\varphi_i = \begin{cases} \phi_{o,1}(g_i) & (1 \leq i \leq L) \\ \phi_{o,2}(g_{i-L}) & (L+1 \leq i \leq 2L) \\ \vdots & \vdots \\ \phi_{o,N}(g_{i-(N-1)L}) & ((N-1)L+1 \leq i \leq NL) \end{cases}. \quad (18)$$

3.3 Kernel Function Value

It's clear we don't have to calculate the kernel function in $\mathcal{H}_s$ but just need its value.

Let an angle between $\Phi_s(f_i^\dagger)$ and $\Phi_s(f_j^\dagger)$ in $\mathscr{F}_s$ be θ_{ij}, the inner product is obtained as the following eq.(19) by deciding on the value of $\|\Phi_s(f_t^\dagger)\|$ and θ_{ij}.

$$\begin{aligned} k_s(f_i^\dagger, f_j^\dagger) &= \Phi_s(f_i^\dagger)^T\Phi_s(f_j^\dagger) \\ &= \|\Phi_s(f_i^\dagger)\| \cdot \|\Phi_s(f_j^\dagger)\|\cos\theta_{ij} \quad (19) \end{aligned}$$

4 Experimental result

4.1 2 Class Problem: Comparison Between KWF-1 and KWF-2

To avoid calculating the $(L \times (N+1))$ generalized inverse matrix to obtain X_2, which needs huge calculation

cost, we ignore the effect of $k_{o,ij}(x,y)$ and adapt an approximated KWF-2 X_2'. We can construct X_2' by letting $K = \tilde{K}$ and $K_j = \sigma_j \tilde{K}^j$.

Table 1: Error rate of KWF-1 and KWF-2

Data set Name	error rate SVM	error rate KWF-1	error rate KWF-2
banana	11.53 ± 0.66	10.38 ± 0.45	$\mathbf{10.29 \pm 0.43}$
breast cancer	26.04 ± 4.47	25.05 ± 4.04	$\mathbf{24.49 \pm 4.29}$
diabetes	23.53 ± 1.73	23.04 ± 1.79	$\mathbf{22.97 \pm 1.83}$
flare solar	$\mathbf{32.43 \pm 1.82}$	33.48 ± 1.62	33.26 ± 1.76
german	23.61 ± 2.07	$\mathbf{23.50 \pm 2.19}$	23.63 ± 2.24
heart	15.95 ± 3.26	16.38 ± 3.59	$\mathbf{15.53 \pm 3.12}$
image	2.96 ± 0.60	$\mathbf{2.79 \pm 0.56}$	2.80 ± 0.52
ringnorm	$\mathbf{1.66 \pm 0.12}$	4.00 ± 0.51	3.23 ± 0.50
splice	10.88 ± 0.66	10.85 ± 0.70	$\mathbf{10.83 \pm 0.67}$
thyroid	4.80 ± 2.19	$\mathbf{4.13 \pm 2.04}$	$\mathbf{4.13 \pm 2.26}$
titanic	22.42 ± 1.02	22.65 ± 0.73	$\mathbf{22.36 \pm 1.00}$
twonorm	2.96 ± 0.23	2.38 ± 0.13	$\mathbf{2.35 \pm 0.11}$
waveform	9.88 ± 0.43	9.54 ± 0.49	$\mathbf{9.50 \pm 0.35}$

We assume $\sigma_i = \sigma \ (\forall i)$ and determine γ, ε and σ by 5-fold cross validation. In the comparison of 2-class problem between KWF-1 and KWF-2, the inner product of the nonlinear functions in $\mathscr{F}_s$ is provided by $\|\Phi_s(f_t^\dagger)\|^2 = 1$ and $\theta_{12} = \pi$.

From Table 1 we can see KWFs have lower error rates than SVM on 11 of the 13 data sets. Furthermore KWF-2, which is regularized on the distance in $\mathscr{H}_o$, is superior to KWF-1 on 10 data sets and for remaining 3 data sets it has almost the same ability to KWF-1.

4.2 Multi-Class Problem: KWF-2

Table 2 shows an experimental result on USPS data set, which consists of 10 classes. Other experimental conditions were the same as the ones of 2 class problem. General abilities of other methods previously proposed are also shown in Table 3. KWF-2's performance was almost as good as other methods shown in Table 3.

5 Conclusion

In this paper, we proposed that we apply KWF to pattern recognition. By doing regularization based on the distance to KWF, its general ability was improved. These facts proved that KWF is effective for not only signal restoration but also pattern recognition. For future works, it's necessary to develop a method to determine the best parameters of the kernel function and a

Table 2: USPS: Error Rate of KWF-2

norm	θ_{ij}	test error	cv error
$\|\Phi_s(f_t^\dagger)\|^2$ $=1$	$\pi/4$	4.43	1.62
	$\pi/3$	4.43	1.62
	$\pi/2$	4.43	1.62
$\|\Phi_s(f_t^\dagger)\|^2$ $=2$	$\pi/4$	4.43	1.62
	$\pi/3$	4.43	1.62
	$\pi/2$	4.43	1.62
$\|\Phi_s(f_t^\dagger)\|^2$ $=t$	$\pi/4$	69.91	49.93
	$\pi/3$	24.71	3.88
	$\pi/2$	5.48	2.30
	$2\pi/3$	4.68	4.44

Table 3: USPS: Error Rate of Other Methods

Method	test error
RBF SVM	4.20
Polynomial SVM	4.00
k-means RBF	6.70

way to reduce the amount of calculation when data set is large.

References

[1] H. Ogawa and E. Oja, Projection filter, Wiener filter and Karhunen-Loeve subspace in digital image restoration, *J. Math. Anal. Appl.*, vol.114, no.1, Feb. 1986, pp.37-51.

[2] M. Yamada and M. R. Azimi-Sadjadi, Kernel Wiener Filter using Canonical Correlation Analysis Framework, *IEEE Workshop on Statistical Signal Processing 2005 (SSP'05)*, Bordeaux, France, July 17-20, 2005.

[3] Y. Washizawa and Y. Yamashita, Kernel Wiener filter, *JIEICE 6workshop in computer information-theoretic learning theory*, Nov. 2003, pp.143-148.

[4] S. Akaho, SVM that Maximizes the Margin in the Input Space, *JIEICE magazine* vol.J86-D-II, no.7, July 2003, pp.934-942. (In Japanese)

[5] S. Abe *Support Vector Machine for Pattern Classification* (Springer-Verlag, 2005).

[6] Y. Washizawa and Y. Yamashita, Non-linear Wiener filter in reproducing kernel Hilbert space, *18th International Conference on Pattern Recognition(ICPR'06)*, 2006, pp.967-970.

[7] Y. Yamashita and H. Ogawa, Relative Karhunen-Loeve Transform, *IEEE TRANSACTIONS ONSIGNAL PROCESSING*, vol.44, no.2, Feb. 1996.

[8] Young-Chul SONG and Doo-Hyun CHOI, Kernel Adjusted Wiener Filter for Image Enhancement, *Japanese Journal of Applied Physics.*, Part 2 Letters, vol.44, issue.6A, 2005, pp3996-3999.

Effect of stiffness and shape on release mechanism mimicking gecko foot-hair

Student Number: 06M18139   Name: Junichi WATANABE   Supervisor: Kunio TAKAHASHI

ヤモリ脚部の微小毛構造を模倣した脱離機構に対する硬さと形状の影響

渡邉絢一

ヤモリは壁や天井で素早く動き回り、強い凝着力を有しながらも容易に足を脱離させる脱離機構を有していると考えられる。本研究ではこの脱離機構に注目し、ヤモリが足の裏に有している微小毛構造を大変形する梁構造であると仮定し、脱離に必要な水平方向と垂直方向の力の関係を求める。そして梁の硬さや形状が脱離機構に与える影響を検討する。

1 Introduction

It is known that geckos can walk on vertical and inverted surfaces quickly using adhesion force generated by a huge number of foot-hair under their feet[1]. Recently, Autumn measured gecko's adhesion force, and reported that the adhesion force is due to Van Der Waals interaction[2][3].The adhesion force of the gecko foot-hair is considered to be independent to the surface's conditions, hence some researches on the application of the mechanism of adhesion have been carried out. Takahashi proposed a release mechanism for gecko foot-hair to explain their quick step[4]. He suggested that gecko can control the normal force for detachment by giving the tangential force. In our former work, we consequently used a straight and hard beam, expressing a single gecko foot-hair, to analyze the relation between the normal and tangential force which are necessary for the detachment process. But actually, gecko foot-hair is soft, and not straight. Therefore, it is possible that the stiffness and shape of the beam influence the release mechanism.

In this study, in order to clarify those effects, a soft beam as shown in Fig.1 is introduced. Numerical and experimental study, to obtain the force at detachment using various kinds of beams, offer us a new understanding of the stiffness and shape's effects on the release mechanism.

2 Model of gecko foot-hair and numerical method

Fig.1 shows a 2-dimensional model of a single gecko foot-hair using an elastic beam, with length l, Young's modulus E, and cross-sectional moment of inertia I. The beam is assumed that, it can be largely deformed, the mass is ignored, both ends can not rotate around, i.e. the root angle θ_l and the top angle θ_0 in Fig.1 are fixed, and it detaches from the object's surface without sliding. We define the contact area which contacts with the object's surface at the lower end of the beam, as adhesion area. The critical stress for detachment at the adhesion area
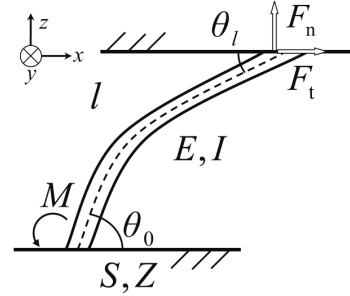

Fig. 1: Model of gecko foot-hair

is constant. When a normal force F_n and tangential force F_t are given to the upper end of the beam, the normal stress is generated at the adhesion area. The normal stress can be expressed as the sum of the stress generated by the normal force F_n and the bending stress generated by the moment M at the lower end of the beam. If the maximum stress at the adhesion area σ_{max} exceeds the critical stress σ_{cr}, the beam detaches from the object's surface. So, the criterion for detachment can be expressed as eq.(1).

$$\frac{F_n}{S} + \frac{|M|}{Z} = \sigma_{max} > \sigma_{cr} \qquad (1)$$

Where, S is the area of the adhesion area, and Z is the section modulus of the adhesion area, and F_n, F_t, and M is assumed positive in the direction of the arrows shown in Fig.1.

From the equations of the beam, the boundary condition (θ_l and θ_0 are fixed), and the criterion for detachment, F_n and F_t at detachment can be solved numerically.

Fig.2 is an example of the numerical result. The line plotted with circle points depicts the F_n and F_t needed to detach the beam from the object's surface in $M > 0$ direction, and the line plotted with triangle points depicts the F_n and F_t needed to detach the beam in $M < 0$ direction. The region surrounded by these two lines denotes the gripping region, i.e. the beam does not detach. In otherwise region, the beam detaches from the surface.
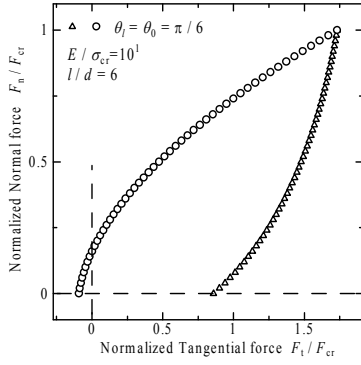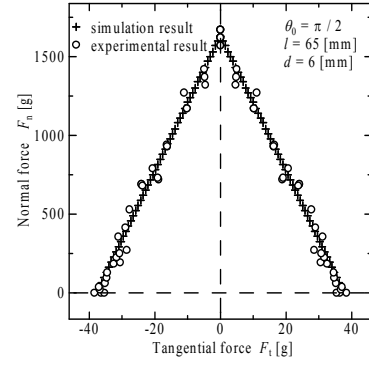
Fig. 2: Example of the numerical result

Fig. 4: Experiment result and numerical result when the beam is deformed slightly (acrylic)
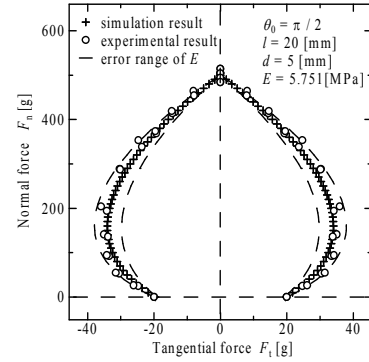
Fig. 5: Experiment result and numerical result when the beam is deformed largely (rubber)

3 Measurement of normal and tangential force at detachment

To verify the validity of the numerical simulation, we carried out a measurement of the normal and tangential force acting on a straight beam at detachment. Both θ_l and θ_0 are 90[degree]. The original experiment model is shown in Fig.3(a).

To simplify the experiment model in Fig.3(a) without losing its generality, we use an equivalent model with a half length and the upper end is free, as shown in Fig.3(b).

Stress generated at the adhesion area is the same as in Fig.3(a). So, the normal force and tangential force at detachment are identical. F_n and F_t are applied to the upper end of the beam, and gradually increased. When the beam begins to detach, we record the values of F_n and F_t. In this experiment, we used an acrylic ($E = 3234$[MPa]) and a rubber ($E = 5.751$[MPa]) cylindrical beams, whose results are shown in Fig.4 and Fig.5.

Fig.4 and Fig.5 show numerical results, solved by the method described in previous section, and experimental results. The numerical results are in good agreement with the experimental ones. So, the validity of the numerical procedure explained in previous section is verified.

4 Effect of stiffness and shape of the beam on the release mechanism

We simulate F_n and F_t required to detach a slanted beam shown in Fig.1, by changing the stiffness and shape of the beam.

First, Fig.6 shows the numerical results when the normalized Young's modulus $\frac{E}{\sigma_{cr}}$ varies, whereas, the shape of the beam is unchanged. From Fig.6, it is clear that the gripping region increases as the beam is softer. This is advantageous for gripping, and also advantageous for avoiding the detachment from a sudden disturbance.

Second, Fig.7 shows the numerical result when the root angle of the beam is changed. From Fig.7, it is clear that, as the root angle of the beam is smaller, the gripping region becomes larger when M is negative compared to that when M is positive. So, the bigger positive tangential force can be held. This is also the advantageous point of the soft beam.

Third, for a single bent beam shown in Fig.8, we simulated and compared the result with those of a straight beam, shown as Fig.9. The area of the ad-
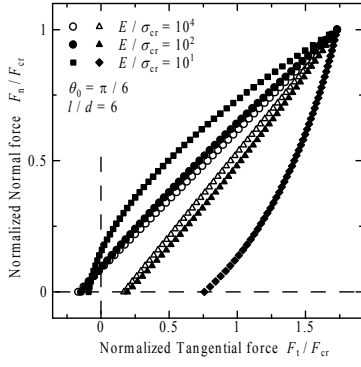

Fig. 3: Experimental model. (a) straight beam, $\theta_0 = \theta_l = \frac{\pi}{2}$. (b) equivalent model of (a), the beam has half length the upper end of the beam is free.

Fig. 6: Effect of stiffness of the beam on release mechanism.

Fig. 7: Effect of gradient of the beam on release mechanism.

Fig. 8: Illustration of a bent beam. u is modulus to decide the bending position of the beam. ($0 \leq u \leq 1$)
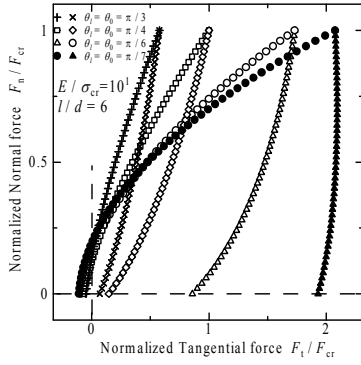

Fig. 9: Effect of shape of the beam on release mechanism.

hesion area S and the section modulus of adhesion area Z of the bent beam and the straight beam are the same. Two kinds of beams are designed as the maximum normal force is identical. From Fig.9, it is clear that when no F_n exerted, bigger F_t is needed to detach the bent beam compared to the straight beam. It is also clear that the gripping region is shifted to the positive direction of F_t, compared to that of the straight beam. $|F_t + F_n|$ needed to detach the bent beam in $M > 0$ direction, i.e. the line with black circles in Fig.9, becomes smaller than that of the straight beam. So, detachment can occur with smaller force. This is advantageous for quick step.

5 Possibility for release mechanism using magnetic force

As an application, we replaced the adhesion force by the magnetic force. To solve the force for detachment, the equations of the beam, the boundary condition, and the criterion for detachment have to be considered. Since the equations of the beam and the boundary condition, depending on the beam, have been previously studied, here, we focus just on the criterion for detachment. In this case, theoretically analyzing the criterion for detachment is difficult.
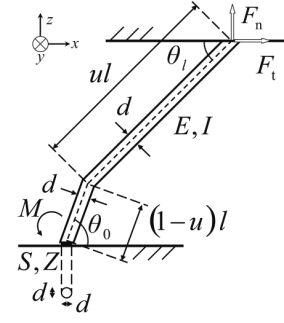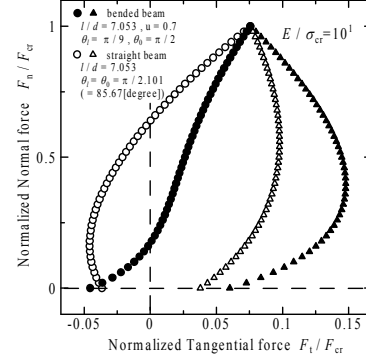
But if the criterion for detachment can be acquired by measurement, the normal and tangential forces for detachment can be solved.

We assumed two kinds of beams as shown in Fig.10. Both of them are straight, hard enough. The same magnets of circular shape and thin enough are fixed to the lower end of both beams (S and Z are the same). When the same magnets are used to the beams under the same condition, the criterion for detachment would be the same. So, if F_n is the same, M is the same, hence, we can get the following expression.

$$F_t' = \frac{F_n \left(\cos \theta_0' - \frac{l}{l'} \cos \theta_0\right) + F_t \frac{l}{l'} \sin \theta_0}{\sin \theta_0'} \qquad (2)$$

If F_n and F_t at detachment using a magnet are measured, we can estimate the relations of the force at detachment for the other beam using the same magnet from eq.(2). Fig.11 and Fig.12 show the experiment results. In both experiments, the estimated results are in good agreement with the experimental results.

We also do the same experiment while changing the maximum normal force by inserting one or two thin plastic sheets between the magnet and the magnetic body. Fig.13 shows the result of the relation of the normalized normal force and normalized moment. From Fig.13, it is clear that the relation
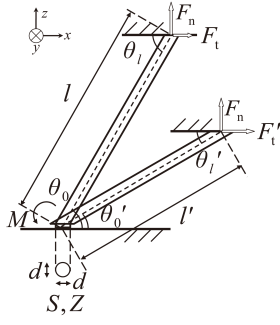
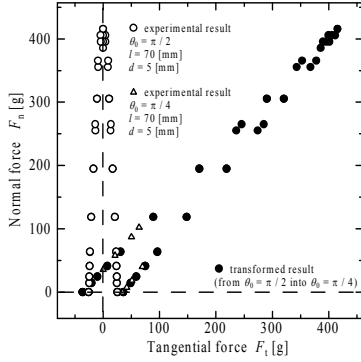Fig. 10: Two kinds of beams having different length and root angle.

Fig. 11: Experimental result when the root angle of the beam is changed.
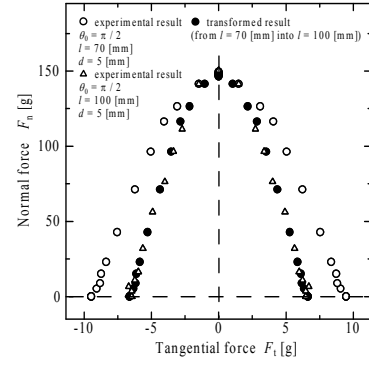

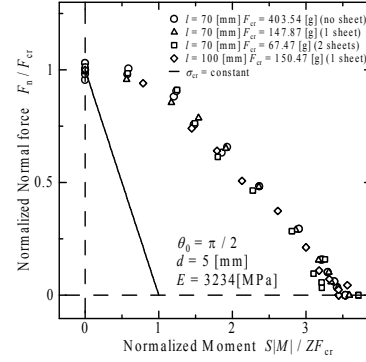Fig. 12: Experimental result when the length of the beam is changed.

Fig. 13: Relation between normal force and moment generated at adhesion area when maximum normal force and length of the beam are changed.

of normalized normal force and normalized moment generated at the adhesion area is almost the same even if the maximum normal force are changed. So, the criterion for detachment seems unchanged even if the magnet is slightly away from the magnetic body.

6 Conclusion

We assumed a single gecko foot-hair with a large deforming beam, and carried out a numerical calculation and experiment to obtain the normal and tangential force at detachment. As the results, we can conclude as follows: first, the gripping region increases as the beam is softer. Second, as the root angle of the beam is smaller, the gripping region becomes larger when the moment generated at adhesion area is negative compared to that when the moment generated at adhesion area is positive. Third, in case of a bent beam, the gripping region is shifted to the positive direction of tangential force, and when no normal force exerted, bigger tangential force is needed to detach the bent beam compared to the straight beam. When magnetic force is used instead of adhesion force, if we know the criterion for detachment by measurement, the relation of the force at detachment can be calculated. The criterion for detachment is possibly unchanged even if

the magnet is slightly apart from the magnetic body. These knowledge are helpful for applying the release mechanism in engineering.

References

[1] Walker.G. Adhesion to smooth surfaces by insects - a review, Int. J. adhesion and adhesive 13: 3-7. 1993.

[2] K.Autumn, W.P.Chang, R.Fearing, T.Hsieh, T.Kenny, L.Liang, W.Zesch, R.J.Full. Adhesive force of a single gecko foot-hair. Nature 405: 681-685. 2000.

[3] K.Autumn, M.Sitti, A.M.Peattie, W.Hansen, S.Sponberg, Y.A.Liang, T.Kenny, R.Fearing, J.N.Israelachvili, R.J.Full. Evidence for van der Waals adhesion in gecko setae. PNAS 99(19): 12252-12256. 2002.

[4] K.Takahashi. Effect of surface roughness on adhesion of multi-hair structure. Computer Methods and Experimental Measurements for Surface Effects and Contact Mechanics VII. 49: 141-150. 2005.

A STUDY ABOUT THE PARAMETERS OF THE NON-LINEAR CONTRACTANCY EXPRESSION FUNCTION

Student Number: 06M18151   Name: NI WEI   Supervisor: Hideki OHTA

(2006)

n_E, n_L

(DACSAR)

n_E, n_L

I.C.

(EC/LC model)

EC/LC model

Ariake clay

n_E, n_L

1. Introduction

Many constitutive equations of the natural clay deposit have been proposed before. As the representative examples there are Original Cam-Clay model (1963), Modified Cam-Clay model (1968), Ohta-Hata model(1971) and Sekiguchi-Ohta model(1977). ε_v (Volumetric strain) and η (stress ratio) have been used to describe the contractansy (negative dilatancy)-response. And the experimental data of ε_v and η has been plotted by Shibata (1963). In Ohta-Hata model, the relationship between them is considered as
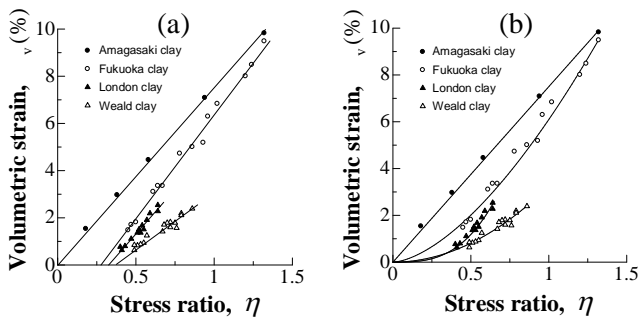

Fig.1.1 Modeling the cotractancy-response as (a) linear and (b) non-linear

linear (Fig.1.1(a)). Ohno (2006) proposed that the relationship between them also can be considered as non-linear (Fig1.2 (b)). By introducing exponential function and logarithmic function to describe the contractancy-response, new constitutive models for the clay deposit called EC/LC model has been

developed. EC/LC model has two new parameters n_E and n_L called fitting parameters in it. With different n_E and n_L value, EC/LC model can connote the representative constitutive equations. EC/LC model is also considered more usefully in prediction of ground deformation by finite element analysis. For that it is important to define the range of n_E and n_L value for the different object clay to improve the prediction accuracy. In fact, the range of value or determination method of n_E and n_L have not been proposed yet.

In this study, define the range of n_E and n_L for different clay is the object. To make the range clearer, many simulations of K_0-consolidation tests under undrained condition for both compression and extension by finite element analysis was carried out. Then, the analysis was compared with the experimental results to determine the possible range value of n_E and n_L. At last, the applicability of the range defined for Ariake clay was examined by simulating the movement during the fill construction process of the highway embankment.

2. The constitutive equation of EC/LC model

Under the axi-symmetric stress condition

$$EC \bmod el : f\left(p', q, \varepsilon_v^p\right) = MD \ln \frac{p'}{p_0'} + \frac{MD}{n_E}\left(\frac{|\eta|}{M}\right)^{n_E} - \varepsilon_v^p = 0$$

$$LC \bmod el : f\left(p', q, \varepsilon_v^p\right) = MD \ln \frac{p'}{p_0'} + \frac{2MD}{n_L}\ln\left(\frac{M^{n_L} + |\eta|^{n_L}}{M^{n_L}}\right) - \varepsilon_v^p = 0$$

1

When $n_E = 1.0$ the EC model corresponds to the Original Cam-Clay model. When $n_L = 2.0$ the LC model corresponds to the Modified Cam-Clay model.

Extend to general stress state

$$EC \bmod el : f\left(\boldsymbol{\sigma}', \varepsilon_v^p\right) = MD\ln\frac{p'}{p_0'} + \frac{MD}{n_E}\left(\frac{\eta^*}{M}\right)^{n_E} - \varepsilon_v^p = 0$$

$$LC \bmod el : f\left(\boldsymbol{\sigma}', \varepsilon_v^p\right) = MD\ln\frac{p'}{p_0'} + \frac{2MD}{n_L}\ln\left(\frac{M^{n_L} + \eta^{*n_L}}{M^{n_L}}\right) - \varepsilon_v^p = 0$$

When $n_E = 1.0$ the EC model corresponds to the Sekiguchi-Ohta model. When $n_L = 2.0$ the LC model corresponds to the Modified Cam-Clay model which is modified by Hashiguchi, Chen (1998) and Asaoka (2002). The shapes of yield surface of EC/LC model are shown as Fig2.1.
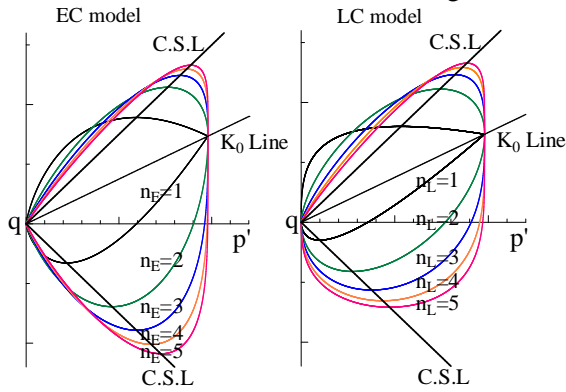

Fig2.1. Shapes of yield surfaces of EC/LC model

3. Experimental results

Watabe (2003) carried out a series of K_0-consolidation tests in a triaxial cell for 8 kinds of marine clay collected from different areas in the world (Fig.3.1). Ariake clay and Yamashita clay from Japan, Bothkennar clay from England, Drammen clay from Norway, Louiseville clay from Canada, Singapore clay from Singapore, Pusan clay from Korea, Bangkok clay from Thailand. For all these 8 kinds of clay, after a K_0-consolidation test with a specimen trimmed to 35mm in diameter and 85mm in height, the K_0-normally consolidated specimen was sheared under undrained condition for both compression and extension. Relationship between (a) deviator stress and axial strain $(q - \varepsilon)$ and (b) deviator stress and effective mean stress $(q - p')$ normalized by the consolidation stress for K_0-normally consolidated undisturbed clays are shown in Fig.3.2.
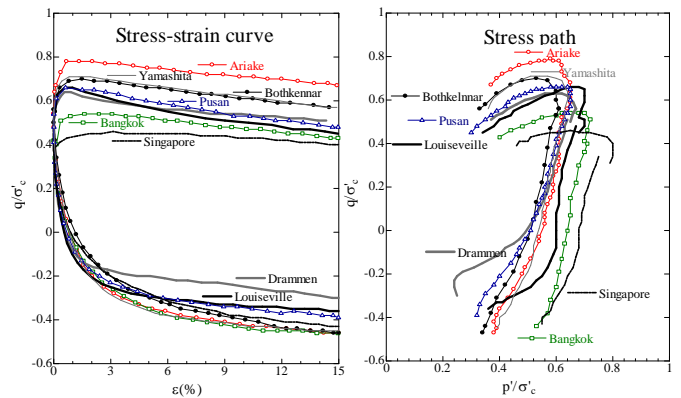

Fig.3.1 Sampling sites for clays dealt in this study

Fig3.2. Stress-strain curves and stress paths observed in $CK_{0NC}UC$ and $CK_{0NC}UE$ tests for undisturbed clays

4. Input parameters

Table 4.1. Input parameters for DACSAR

Parameter	Description
D	Coefficient of Dilatancy proposed by Shibata(1963)
Λ	Irreversibility Ratio expressed by
M	Critical State Parameter
v'	Effective Poission's Ratio
σ_{v0}'	Preconsolidation Pressure
K_0	Coefficient of Earth Pressure at rest immediately after K_0-normal consolidation (reference state)
σ_{vi}'	Effective Overburden Pressure in-situ
K_i	Coefficient of In-situ Earth Pressure at rest
α	Coefficient of Secondary Compression expressed by $\alpha = d\varepsilon_v/(d(\ln t))$ at time t_c
$\dot{v}_0$	Initial Volumetric Strain Rate at reference state expressed by $\dot{v}_0 = \alpha / t_c$, where t_c is the time at end of primary consolidation
λ	Compression Index in the $e - \ln(p'/p_0')$ relationship $\lambda = 0.434C_c$ (Cc is compression index in the e-logp' relationship)
e_0	Void Ratio corresponding to σ_{v0}' at reference state (if you don't know the value of e_0, specify $e_0 = 0$)
n_L, n_E	fitting parameter to describe non-linear contractancy

In this study, the simulation was carried out by DACSAR (Deformation Analysis Considering

Stress Anisotropy and Reorientation). The descriptions about the input parameters are shown as Table 4.1. And the values of input parameters are shown as Table 4.2.

Table 4.2. The value of input parameters

clay	D	Λ	M	ν'	$\sigma'_{v0} (kPa)$	K_0
Drammen	0.031	0.88	1.35	0.32	336.8	0.47
Bothkennar	0.096	0.95	1.61	0.30	240.0	0.43
Louiseville	0.112	0.93	1.32	0.35	408.4	0.53
Singapore	0.158	0.83	0.81	0.39	734.7	0.66
Bangkok	0.143	0.84	1.09	0.39	279.9	0.64
Pusan	0.098	0.91	1.38	0.32	213.3	0.47
Ariake	0.064	0.92	1.67	0.30	150.0	0.43
Yamashita	0.072	0.92	1.58	0.31	941.2	0.45
clay	K_i	α	$\dot{v}_0$	λ	$\sigma'_{vi} (kPa)$	e_0
Drammen	0.47	0.002	0.002	0.10	336.8	1.12
Bothkennar	0.43	0.008	0.008	0.45	240.0	1.79
Louiseville	0.53	0.008	0.008	0.45	408.4	1.79
Singapore	0.66	0.008	0.008	0.36	734.7	1.34
Bangkok	0.64	0.009	0.009	0.49	279.9	1.62
Pusan	0.47	0.007	0.007	0.39	213.3	1.63
Ariake	0.43	0.006	0.006	0.55	150.0	3.82
Yamashita	0.45	0.006	0.006	0.44	941.2	2.54

5. Analysis results

Table 5.1. Range for fitting parameters

Clay	EC model n_E		LC model n_L	
	Elasto Plastic	Elasto Visco Plastic	Elasto Plastic	Elasto Visco Plastic
Drammen	1.0 1.1	1.0	1.3 1.5	1.1 1.3
Bothkennar	1.0 1.1	1.0	1.3 1.5	1.1 1.3
Louiseville	1.1 1.3	1.0	1.6 1.7	1.2 1.4
Singapore	1.1 1.3	1.0	1.4 1.6	1.2 1.4
Bangkok	1.1 1.3	1.0	1.4 1.6	1.2 1.4
Pusan	1.1 1.2	1.0	1.4 1.6	1.2 1.3
Ariake	1.1 1.3	1.0	1.3 1.5	1.2 1.4
Yamashita	1.0 1.2	1.0	1.4 1.6	1.1 1.3

The simulation of K_0-consolidation tests under undrained condition for 8 kinds of marine clays was carried out and the analysis result for Ariake clay was plotted as Fig. 5.1~5.4. Consequently, n_E and n_L value for the other clays are listed in Table 5.1. For Ariake clay, the movement analysis during the fill construction process was carried out with the range value $n_E = 1.0 \sim 1.3$ and $n_L = 1.2 \sim 1.5$. Then, compare the analysis results to the field
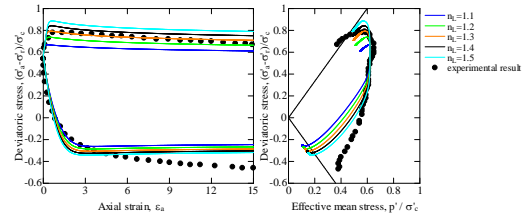
measurement data to examine the applicability of the n_E and n_L value defined (Fig.5.5 and Fig.5.6).
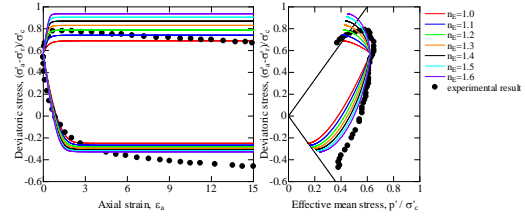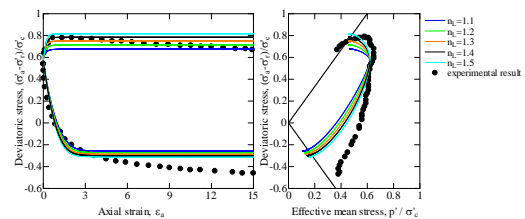

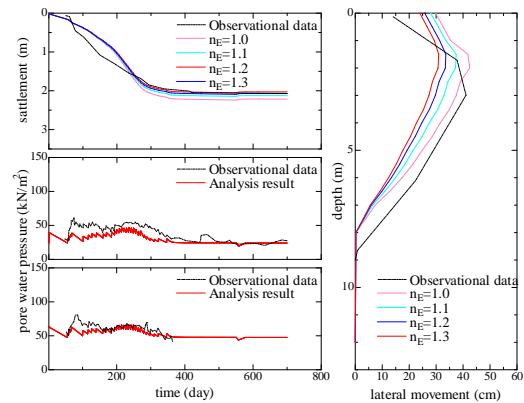**Fig.5.1. Using EC model without considering viscosity**
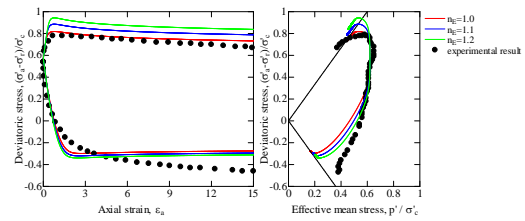
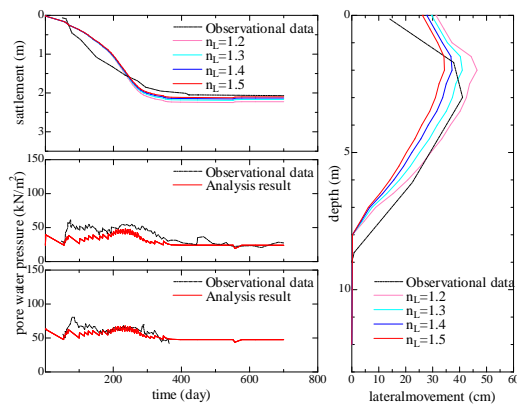**Fig.5.2. Using EC model considering viscosity**

Fig.5.3. Using LC model without considering viscosity

**Fig.5.4. Using LC model considering viscosity**

Fig.5.5. Movement simulation using EC model

3

Fig.5.6. Movement simulation using LC model

6. Conclusions

For the 8 kinds of marine clays the range values of n_E and n_L was approximately defined. The values for Ariake clay was $n_E = 1.0 \sim 1.3$ and $n_L = 1.2 \sim 1.5$. The applicability for those values also was examined. Consequently, the reliability is 75% when simulated by EC model, on the other hand it is 80% when use LC model. The adjustment ratio plotted in Fig6.1 shows that the best values of fitting parameters are $n_E = 1.2$ and $n_L = 1.5$.
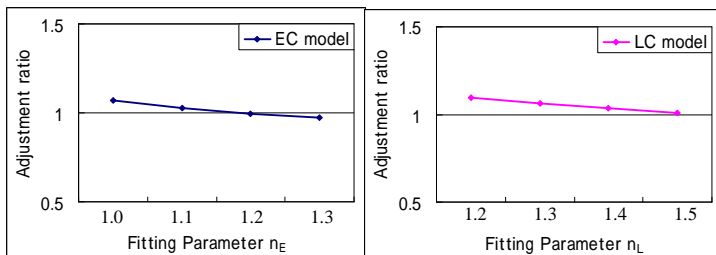
Fig.6.1. The adjustment ratio of EC/LC model

References

[1]Yoichi WATABE, Masanori TANAK, Hiroyuki TANAKA and Takahashi TUCHIDA, K_0-CONSOLIDATION IN A TRIAXIAL CELL AND EVALUSATION OF IN-SITU K_0 FOR MARINE CLAYS WITH VARIOUS CHARACTERISTICS, SOIL AND FOUNDATIONS Vol. 43, No. 1, 1-20, February 2003 Japanese Geotechnical Society, 2003.

[2]Shintaro OHNO, ELASTO-PLASTIC CONSTITUTIVE MODELS DERIVED FROM NON-LINEAR DESCRIPTION OF SOIL CONTRACTANCY, Doctor's Thesis of Tokyo Institute Technology Graduate School of Science and Engineering, 2006.

[3]Tomohide TAKEYAMA, ANALYSIS ABOUT MECHANICAL SECULAR VARIATION OF THE FILL STRUCTURE ON THE SOFT GROUND, Graduate Thesis of Tokyo Institute Technology, 2001.

[4]Shintaro OHNO, Atsushi IIZUKA and Hideki OHTA, DEVELOPMENT OF THE ELASTO-PLASTIC CONSTITUTIVE MODEL FOR SOILS BY USING NEW DESCRIPTIVE FUNCTION OF CONTRSCTANCY, Technical report, 2006.

[5]Takenobu FUJIKAWA and Masateru TAKAYAMA, PHYSICAL PROPERTIES OF ARIAKE MARINE CLAY-GEOTECHNICAL PROPERTIES OF ARIAKE MARINE CLAY(1)-, Transactions of The Japanese society of Irrigation Drainage and Rural Engineering, 1980.

[6]Takenobu FUJIKAWA and Masateru TAKAYAMA, COMPRESSION INDEX OF ARIAKE MARINE CLAY-GEOTECHNICAL PROPERTIES OF ARIAKE MARINE CLAY(2)-, Transactions of The Japanese society of Irrigation Drainage and Rural Engineering, 1980.

[7]Takenobu FUJIKAWA and Masateru TAKAYAMA, Cu/p VALUE OF ARIAKE MARINE CLAY-GEOTECHNICAL PROPERTIES OF ARIAKE MARINE CLAY(3)-, Transactions of The Japanese society of Irrigation Drainage and Rural Engineering, 1980.

[8]Kenta MIZUNO, Takashi TSUCHIDA, Masaki KOBAYASHI and Yoichi WATABE, NEW CONSTITUTIVE EQUATION OF CLAY AND THE PREDICTION OF HORIZONAL DEFORMATIONS OF LARGE SCALE EMBANKMENTS, Journals of the Japan Society of Civil Engineers Vol.63 No.4, 936-953. 2007.11.

[9]Hiroyuki TANAKA, Jacques Locat, Dinesh Raj Shiwakoti and Masanori TANAKA, DIFFERENCES IN PHYSICAL AND CHEMICAL PROPERTIES OFJAPANESE AND NON-JAPANESE CLAYS, The Japanese Geotechnical Society, 2001.

[10]Shintaro OHNO, Tomohide TAKEYAMA, Thirapong PIPATPONGSA, Hideki OHTA and Atsushi IIZUKA, ANALYSIS OF EMBANKMENT BY NONLINEAR CONTRACTANCY DESCRIPTION, Proc. 13th Asian Regional Conference on Soil Mechanics and Geotechnical Engineering, Kolkata, India, 2007.

[11]Hashiguchi, K. and Chen, Z.P., ELASTOPLASTIC CONSTITUTIVE EQUATION OF SOIL WITH THE SUBLOADING SURFACE AND ROTATIONAL HARDENING, International Journal for Numerical and Analysis Method in Geomechanics, Vol.22, 197-277.

[12]Asaoka, A., Noda, T., Yamada, E., Kaneda, K. and Nakano, M.. AN ELASTO-PLASTIC DESCRPTION OF TWO DISTINCT VOLUME CHANGE MECHANISMS OF SOILS, Soils and Foundations, Vol.42, No.5, 47-57.

4

Development of a visible light responsive photocatalyst

for PCE treatment

Student Number: 06M18168   Name: Zhiwei Wu   Supervisor: Hirofumi Hinode

　現在テトラクロロエチレン(PCE)などの有機塩素化合物による地下水の汚染が発生している。このような化学物質は産業活動を継続発展させるために現在は不可欠な物質でもある。そのため、これらの化学物質の高度処理システムの開発が急務である。本研究では有機塩素化合物である PCE を除去するための簡易かつ省エネルギーな方法で、太陽光が利用できる可視光応答型触媒多層カーボンナノチューブと酸化チタンの複合触媒(TiO₂-MNWT)を開発し、PCE 光分解実験によって評価を行った。実験の結果、TiO₂-MNWT 触媒にシナジー効果が現れ、可視光照射で TiO₂- MNWT 複合触媒を用いた PCE も光分解ができた。

1. Introduction

Chlorinated organic compounds such as tetrachloroethylene (PCE) and tricholoroethylene (TCE) have been widely used as industrial solvents for degreasing metals and dry cleaning. However, they are commonly found to cause water, soil and air pollution due to their low biodegradability, toxicity and high persistence in the environment. In water environment, contamination is usually found in groundwater. The treatment of groundwater contaminated with PCE will be very costly and requires long treatment time due to large amount of groundwater that must be treated. Although some effective PCE treatment methods have been established for industrial purposes, there is still no practical method for groundwater treatment. Some methods such as air pershing or bioremediation have been researched recently, however these methods have problems such as secondary treatment or long treatment period. Previous study of treatment method using photocatalysis by titanium dioxide (TiO_2) supported on carbon nanotube under ultraviolet light (UV) showed promising results in adsorptive ability and photoactivity of the catalyst [1]. Using this photocatalyst, low energy cost, short treatment period and simple treatment process could be achieved.

In this study, the photodegradation of PCE under visible light irradiation using the composite of TiO_2 and multi-walled carbon nanotube (MWNT) photocatalyst was investigated.

2. Experimental

Preparation and characterization

TiO_2-MWNT was synthesized by sol-gel method. The precursor, titanium isopropoxide (TIP), was hydrolized to form TiO_2 and deposited on MWNT with the aid of supersonic treatment [2].

Catalyst are named as X-TiO_2-MWNT, where X (1, 10, 20 and 30) corresponds to the weight ratio of MWNT to a 100 weight basis of TiO_2-MWNT (ex. 10-TiO_2-MWNT means 100(TiO_2-MWNT):10(MWNT), w/w)

The TiO_2-MWNT composites were characterized by TEM, XRD, TG, BET and UV-vis spectroscopy.

Photodegradation experiments

The evaluation of TiO_2-MWNT photocatalytic activity for degradation of PCE was conducted under UV and visible light irradiation. The experiments were carried out in a glass immersion photochemical reactor. The reactor was equipped with a UV and visible light lamp (100W, 300nm~600nm) located axially and held in a quartz immersion, and a UV-cut film which allows only visible light (400nm~600nm) to pass. The UV photodegradation experiment was carried out without the UV-cut film and the visible light photodegradation experiment was carried out by applying the UV-cut film on the lamp. The experiments was done in a closed system. Before irradiation, the PCE solution with photocatalyst was stirred in a dark condition for 60 minutes to establish an adsorption-desorption equilibrium.

3. Result and Discussion
Characterization

The XRD results of TiO_2-MWNT are shown in Figure 1. Only titania in anatase structure were found from the XRD patterns of TiO_2 and TiO_2-MWNT. This structure is known to contribute to the photoactivity. The intensity of MWNT in TiO_2-MWNT was lower than that in MWNT. And the peak of TiO_2 shifted slightly with the addition of MWNT. This could indeicate a change in crystal structure of TiO_2. The sizes of catalysts ($d_{catalyst}$) calculated from XRD are listed in Table 1. The size of TiO_2-MWNT increased with the ratio of MWNT in TiO_2-MWNT.

The carbon contents of TiO_2-MWNT calculated from the TG curves (C_{TG}) are listed in Table 1.

The results from BET surface area measurements are also given in Table 1. The surface areas of TiO_2-MWNT (BET) were higher than those of estimated theoretically based on the amount of TiO_2 and MWNT (BET_{cal}). It can be attributed to the formation of new mesopores between TiO_2 and MWNT.
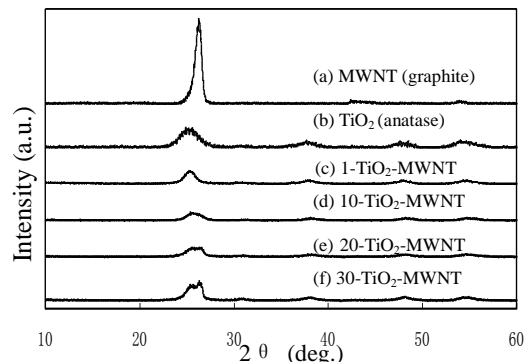

Fig. 1 XRD results

Table 1
Carbon content determined from TG (C_{TG}), Calculated BET surface area (BET_{cal}) and determined BET surface area (BET), TiO2-MWNT size ($d_{catalyst}$)

Catalyst	C_{TG}(%)	BET (m²/g)	BET_{cal}(m²/g)	$d_{catalyst}$(nm)
TiO_2	—	127.32	—	8.28
MWNT	—	20.62	—	—
1-TiO_2-MWNT	1.84	128.99	126.65	9.24
10-TiO_2-MWNT	8.95	130.14	116.65	9.49
20-TiO_2-MWNT	21.39	131.18	105.98	10.48
30-TiO_2-MWNT	31.57	136.90	95.31	11.79

Figure 2 shows UV-vis spectroscopy results of TiO_2 and TiO_2-MWNT. As expected TiO_2 has low absorption toward visible light range (400nm~600nm). On the other hand, the composite catalysts with MWNT could absorb more at wavelength higher than that of TiO_2 even starting at low MWNT ratio (1-TiO_2-MWNT).
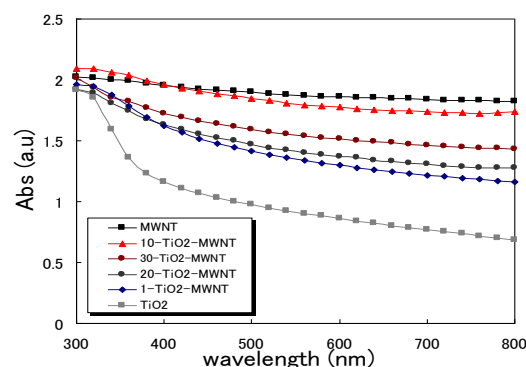

Fig.2 UV-vis spectroscopy

Photoactivity for PCE degradation

Figure 3 shows the PCE degradation by photocatalysts under UV irradiation. No improvement os PCE conversion could be observed when using MWNT only. High conversions of PCE were observed for 1-TiO_2-MWNT, 10-TiO_2-MWNT and TiO_2 only. Samles with MWNT ratio than 10-TiO_2-MWNT showed a decrease in conversion of PCE. High amount of MWNT could cover TiO_2 thus reduced the photoactivity of the TiO_2-MWNT composite photocatalyst.

Figure 4 shows the PCE degradation under visible light irradiation with photocatalysts. MWNT showed no photoactivity toward visible light. 10-TiO_2-MWNT gave the highest PCE conversion which was almost twice as high as TiO_2 only. This result indicated a synergetic effect between TiO_2 and MWNT which could lower the energy band gap of TiO_2 toward visible light range.

The PCE photodegradation mechanism could be explained as followed. Firstly, PCE was adsorbed on MWNT, then transfered to TiO_2 surface. The driving force for this transfer was probably the difference in the PCE concentration between MWNT and TiO_2 [3]. MWNT could also act as electron donor by injecting electrons into the TiO_2 conduction band and lower TiO_2 energy band gap so that it could be photoactive and generate highly active hydroxyl radicals in visible light

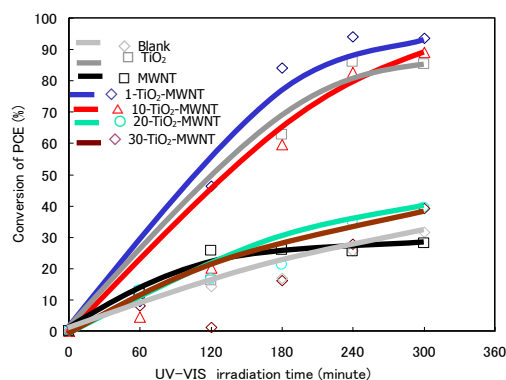range. Then PCE adsorbed on TiO_2-MWNT could be degraded by the radicals [4].
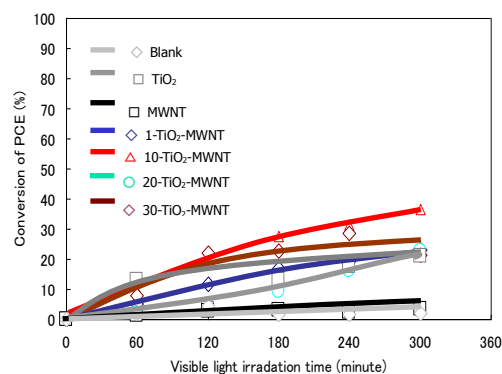

Fig.3 PCE degradation under UV irradiation

Fig.4 PCE degradation under visible light irradiation

4. Conclusion

TiO_2-MWNT photocatalyst was prepared by a modified sol–gel method. The PCE degradation using TiO_2-MWNT photocatalyst under visible light irradiation was confirmed with 10-TiO_2-MWNT showing the highest photoactivity under visible light irradiation (35% PCE converted).

From the result, a synergetic effect was found which makes TiO_2-MWNT to be activated under visible light irradiation. MWNT could act as electron donor by injecting electrons into the TiO_2 conduction band and lower TiO_2 energy band gap so that it could be photoactive and generate highly active hydroxyl radicals in visible light range.

Reference:
[1] Tomonori, OGATA, the Dissertation for Master Degree of Engineering, 2005.
[2] G An, W Ma, Z Sun, Z Liu: *Carbon*, **45**, 9, (8.2007) 1795-1801.
[3] J. Matos, J. Laine and J.-M. Herrmann, *Appl. Catal. B* **18** (1998), p. 281.
[4] A. Kongkanand and P. V. Kamat: *ACS Nano*, 1(1), 13(2007)

Plasma Enhancement of Hydrogen Permeation through Metal Membrane

Student Number: 06M1817-4   Name: Xuejia Zhu   Supervisor: Masaaki SUZUKI

CO

1 Introduction

The properties of hydrogen in metals are important in describing many phenomena such as heterogeneous catalysis, purification of hydrogen by membranes, and storage of hydrogen in metal hydrides [1–6]. However, a detailed understanding of metal–hydrogen systems is required, in particular, for the development of membrane reactor and fuel cell technologies. It is well known that Pd has a special tendency to absorb hydrogen compared to many other metals and hence Pd–H system has been investigated extensively [1–6]. On the other hand, Pd and its alloys have been known for their hydrogen separation. Of the Pd alloys, Pd–Ag is by far the most studied [7]. While Pd readily absorbs large amounts of hydrogen at room temperature but hydrogen is practically insoluble in Ag. Despite this, the solubility of hydrogen is larger in Pd–Ag alloys.

Further, Pd–Ag alloy membranes have high-selectivity for hydrogen permeation and hence suitable for hydrogen selective membranes. In this regard, the understanding of hydrogen permeation in Pd–Ag alloy is extremely important.

Through a large amount of work has been aimed at the preparation of thin palladium or palladium alloy layers, there is little known about the influences to that of plasma.

In this thesis, considering that plasma has possibilities of permeation enhancement due to its dissociation at low temperature, the plasma effect on hydrogen permeation through thin silver-palladium membranes has been investigated experimentally.

2 Experimental

2.1 Gas permeation measurements
A shell-and-tube apparatus shown in Fig. 1 equipped with mass flow controllers, pressure gauges and mass flow meter is used to measure the permeation of hydrogen through the membranes. One of the ends of membrane tube is connected to the outlet tube, the other one is cemented together with a thermal-couple, whose o.d. is 0.25mm. And it is placed in the center of an electric furnace which is used as a heater to change the outside temperature for comparisons between the permeations with or without plasma. Hydrogen or /and helium gas is introduced into the membrane tube from outer shell through the mass flow controller and the gas permeated through the membrane is led to a mass flow meter to measure the flow rate.CH_3OH, CO, H_2O is introduced as a contamination source from the left bypass which is shown in the Fig. 1. Both in the "Thermal" condition and the "Plasma" condition, the membrane temperature are all controlled at 190 . The pressure of feed side is 1 atmospheric pressure and the pressure of permeated side is vacuum.

2.2 Electrodes arrangement and Membranes
The metal membrane which was used in this research is a kind of composite palladium/silver alloy. In Table 1 the detail information is listed. Then, the reactors is connected onto the ground to make it played as separator and the inner electrode. A piece of the commercial aluminum film is helically band around a silica glass of which the o.d. is 6mm as the outer electrode, and the length of it is 80 ~ 70mm approximately. As soon as power is supplied, the plasma generated between the outer membrane and the silica glass. Fig. 2 shows the electrodes arrangement and membranes. At the membrane's temperature $150^{\circ}C$, the primary current was 0.10 ~ 0.11 [A], and the voltage was 34 ~ 35 [V], while at that of $190^{\circ}C$, it was 0.13 ~ 0.14 [A] and 38 ~ 40 [V], respectively.
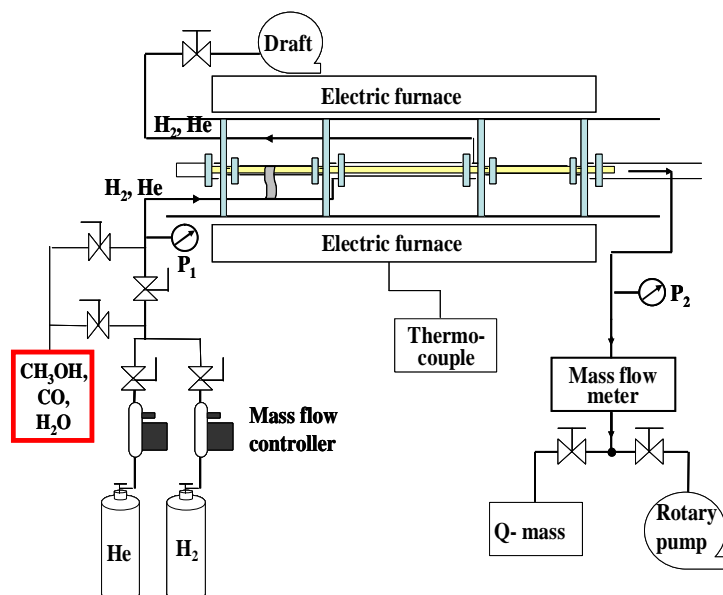
1

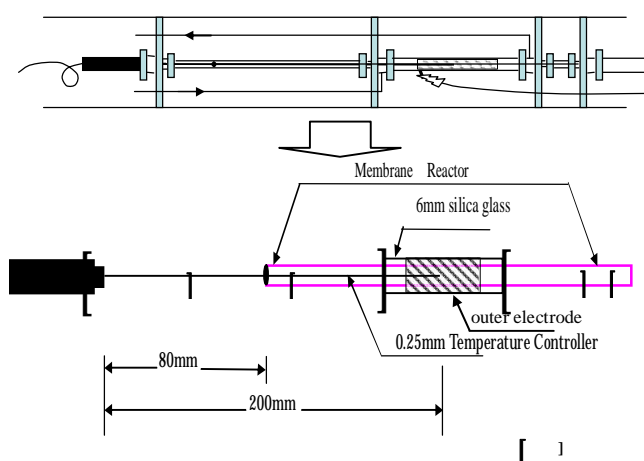Fig. 1. Equipment used for gas permeation experiments of the membrane.

Fig. 2. The electrodes arrangement and membranes.

Table 1   The information about the palladium/silver alloy tube

	Ag-Pd alloy
percent of Pd (%)	75
o.d. (mm)	1.4
i.d. (mm)	1.25
thickness (μ m)	75
length (mm)	330
operating length (mm)	65-85
with porous support	×

3 Results and discussion

In this study, basically, hydrogen permeation experiments were carried out at the same membrane temperature in spite of existence of plasma. As plasma generates heat during discharge by itself, membrane surface temperature was controlled by using additional furnace heating. Therefore, two kinds of heating conditions were in the research. One is the test section is heated by only furnace heating and the other is heated by both of heat generated due to plasma discharge and heat by additional furnace heating. In the following discussion and figures, "thermal" means the former condition and "plasma" means the latter condition.

3.1 Plasma Enhancement of Hydrogen Permeate-on

Figure 3 shows Hydrogen permeability through the palladium/silver alloy membrane under two heating conditions "thermal" and "plasma".
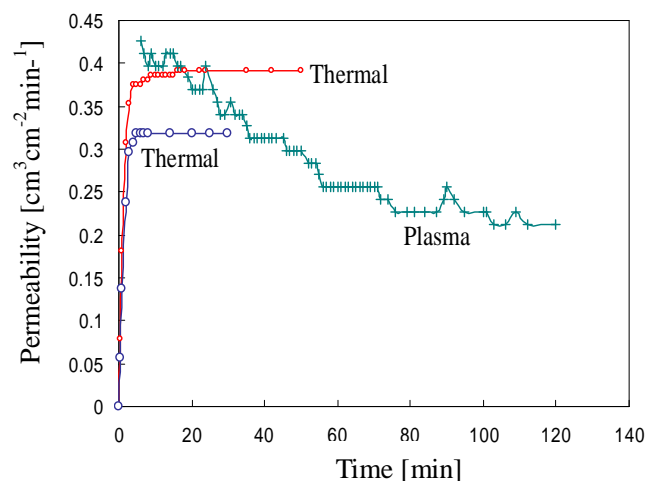

Fig. 3. Hydrogen permeability through the palladium/silver alloy membrane under two heating conditions "thermal" and "plasma".

From this figure, it may be seemed that the hydrogen permeations can be enhanced by plasma ignition. However, the absolute value of permeability is very low and data including error are unstable without reproducibility.

3.2 Effect of Air-treatment

The effect of air-treatment was shown in Fig. 4. Air-treatment is the operation that the system is opened to the atmosphere and kept at 190°C for 16 hours.

From Fig. 4, it can be seen that permeability increases significantly compared with the one before treatment. This effect can be understood by

2

explanation that the membrane surface, which was contaminated by water molecule or other, is cleaned up and the surface area working for permeability increases. After this treatment, however, plasma effect was not detected.
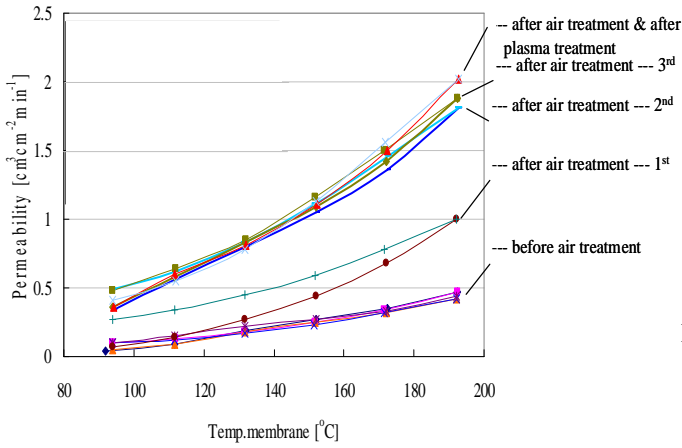

Fig. 4. Hydrogen permeations in thermal condition before and after air-treatment.

3.3 Effect of Adsorbed Methanol

Figure 5 shows that of the effect of adsorbed methanol on the surface of the membrane. The ratio of CH_3OH to H_2 is 15:100.

In order to compare the effect of adsorbed methanol under the two kinds of heating conditions, the procedure was taken as following: first, the "thermal" experiments with and without water were carried out 3 times, and then, stopped the furnace heating to cooling down until the temperature of membrane becomes to the room temperature. After that, the "plasma" experiments with and without water were carried out 3 times.

In the figure, blue circle means the data when not supplying methanol vapor and pink circle means the one when supplying methanol vapor, in the "thermal" experiments. Also, greenish-blue circle means the data when not supplying methanol vapor and red circle means the one when supplying methanol vapor, in the "plasma" experiments. Green line shows with no additional heating.

From Fig. 5, it is clearly that the adsorbed methanol on the membrane's surface suffocated the permeation of hydrogen, because during the reaction in plasma, carbon monoxide was created. And carbon monoxide adsorbed chemically with palladium atoms strongly, and then covered the surface of it, so that the membrane couldn't work as normal [9]. This was confirmed by CO introducing experiments in Section 3.4.
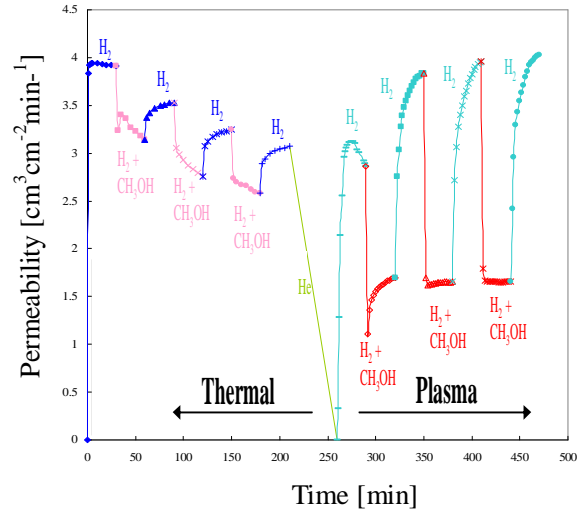

Fig. 5. The comparison between Hydrogen permeations through the palladium/silver alloy layer by thermal and plasma with adsorbed CH_3OH molecules.

3.4 Effect of Adsorbed Carbon Monoxide

Using the same method as that used in Section 3.3, carbon monoxide was supplied together with hydrogen to membrane's surface. The ratio of CO to H_2 is 1.2:100.

The result is shown in Fig. 6. In the figure, purple circle means the data when not supplying carbon monoxide and black circle means the one when supplying carbon monoxide, in the "thermal" experiments. Also, pink circle means the data when not supplying carbon monoxide and dark purple circle means the one when supplying carbon monoxide, in the "plasma" experiments. Green line shows with no additional heating.
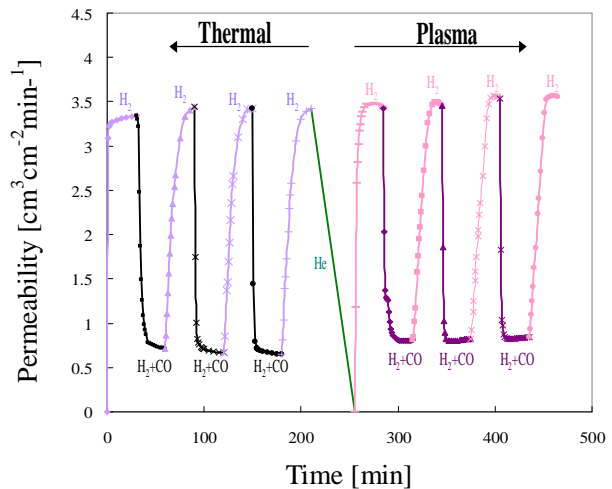

Fig. 6. The comparison between Hydrogen permeations through the palladium/silver alloy layer by thermal and plasma with adsorbed carbon monoxide.

From this figure, the explanation of Section 3.3 was confirmed. That the reason of the adsorbed methanol on the membrane's surface suffocated the

3

permeation of hydrogen is that during the reaction, carbon monoxide was produced, which can combine with palladium atoms strongly, and then covered the surface of it, so that the membrane couldn't work as normal [9].

3.5 Effect of Adsorbed Water Molecules

Using the same method, introducing water vapor together with hydrogen to membrane's surface was done. The ratio of H_2O to H_2 is 2.4:100.

The result is shown in Fig. 7. In the figure, black circle means the data when not supplying water vapor and blue circle means the one when supplying water vapor, in the "thermal" experiments. Also, purple circle means the data when not supplying water vapor and blue circle means the one when supplying water vapor, in the "plasma" experiments. Green line shows with no additional heating.
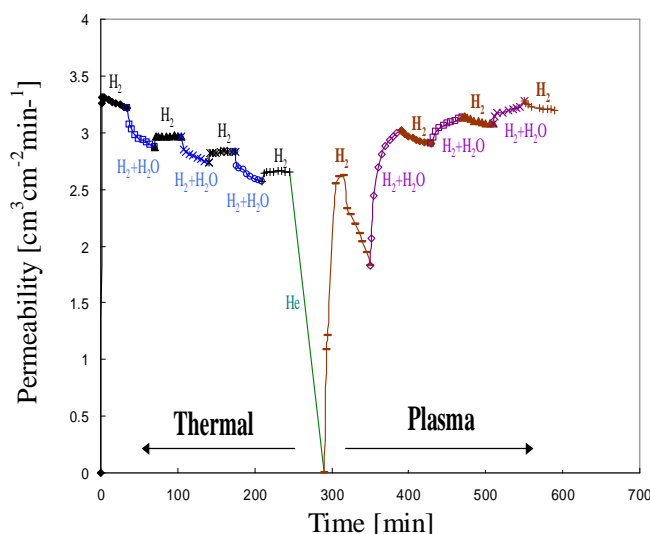

Fig. 7. The comparison between Hydrogen permeations through the palladium/silver alloy layer by thermal and plasma with adsorbed water molecules.

From this figure, it can be found that the hydrogen permeation was suffocated by the water molecules adsorbed on the surface of the membrane in "thermal" condition. However, it was enhanced in "plasma" condition. At the atmospheric pressure lots of water molecules adsorb on the membrane surface by introducing water vapor. The water molecules adsorbed on the membrane suffocate the dissociation of hydrogen molecules and it makes the permeability lower and lower. In plasma atmosphere, the hydrogen atoms, which are dissociated by electrons with high energy, can go through the water film into the membrane, and the water film is effectively on preventing the dissolved hydrogen atoms get out and recombine on the membrane's surface. So in the plasma's case, the hydrogen permeation can get higher and higher

value. The same phenomenon has been reported in low pressure (about 2 Pa) in the research related to nuclear reactor [8].

4 Conclusion

The effect of plasma on hydrogen through thin silver-palladium membranes was studied.

➤ Hydrogen permeations can be enhanced by plasma ignition. However, the absolute value of permeability is very unstable and include big error.
➤ Due to the air-treatment, the surface of the permeability membrane was cleaned up.
➤ Because of the adsorbed water molecules on the surface of the membrane, the hydrogen permeation was suffocated with thermal condition. However, it was enhanced with plasma.
➤ The adsorbed methanol on the membrane's surface suffocated the permeation of hydrogen. Especially, in the plasma condition, carbon monoxide produced by electron impact suffocates the permeation.

References

[1]   G. Alefeld, J. Völkl, Hydrogen in Metals. I. Basic Properties, Springer, Berlin, 1978.
[2]   G. Alefeld, J. Völkl, Hydrogen in Metals. II. Applicationoriented Properties, Springer, Berlin, 1978.
[3]   L. Schlapbach (Ed.), Hydrogen in Intermetallic Compounds. I. Electronic, Thermodynamic, and Crystallographic Properties, Preparation, Springer, Berlin, 1988.
[4]   L. Schlapbach (Ed.), Hydrogen in Intermetallic Compounds. II. Surface and Dynamic Properties, Applications, Springer, Berlin, 1992.
[5]   Y. Fukai, The Metal–Hydrogen System, Springer, Berlin, 1993.
[6]   H.Wipf, Hydrogen in Metals. III. Properties and Applications, Springer, Berlin, 1997.
[7]   F.A. Lewis, The Palladium–Hydrogen System, Academic Press, London, 1967.
[8]   Masayuki Takizawa, A study about the low temperature plasma drive hydrogen permeation phenomenon, Tokyo Institute of Technology, 1998. (in Japanese)
[9]   Yoshimi Kubo The application of the fuel cell - Application to a mobile device of a direct methanol type fuel cell-
http://www.jaie.gr.jp/z18_kubo.pdf.

4

Enhancement of Permeation for Emulsion Liquid Membrane Separation of Coal Tar Absorption Oil

Student Number: 06M18197   Name: Dejin BI   Supervisor: Ryuichi EGASHIRA

(EG)   (DEG)

(TEG)   (

)   (1-   2-   )

O/W/O

EG DEG TEG

DEG   EG   TEG

1. Introduction

Coal tar absorption oil (AO) is one of distillation fractions of coal tar (b.p. =470~550K). There are several kinds of chemical compounds contained in it, the nitrogen heterocyclic compounds such as quinoline (Q), isoquinoline (IQ), indole (IL); the homocyclic compounds such as 1-methylnaphthalene (1MN), 2-methylnaphthalene (2MN), etc. These compounds are useful as raw materials for agricultural chemicals, medicines, perfumes, and many other useful chemicals. Generally, the current method mainly used to separate these compounds in AO is carried out in two steps: separation of AO into several fractions by acidic and basic extraction; and further separation and purification of these fractions into respective products by other methods. The separation for this first step in the industrial fields has some drawbacks, e.g., corrosion of the equipments and difficulties in solvent recovery. To solve these problems, several alternative methods, such as liquid-liquid extraction method and O/W/O emulsion liquid membrane permeation (LMP) method have been proposed[1)-5)]. In O/W/O emulsion liquid membrane system, water is the main material of aqueous membrane liquid phase. Although water showed a rather highly selective nature in separation but it only allowed quite slow permeation of compounds through liquid membrane because the solubilities of above-mentioned components (Q, IQ, IL, 1MN, 2MN etc.) in water are not so high. EG, DEG, TEG have been widely used as solvent to dissolve organic compounds and would have a high capacity for the dissolution of compounds which contained in AO. Therefore, the addition of one of these substances into an aqueous membrane solution is expected to enhance the permeation[6)-7)].

This work tried to enhance the permeation in separation of AO by O/W/O emulsion liquid membrane. At first the distribution coefficients of compounds which contained in AO, between EG, DEG, TEG aqueous solution and AO were measured. Then an aqueous membrane solution with adding EG, DEG or TEG was used in O/W/O emulsion liquid membrane separation of AO. The effects of these three kinds of additives on yield and separation selectivity were described.

2. Liquid-liquid equilibrium between absorption oil and aqueous phase

2.1. Experimental

AO and aqueous solution of EG, DEG, TEG were brought into contact to be equilibrated using Erlenmeyer flask and commercial constant temperature bath. Then the solvent phase and raffinate phase were sampled and analyzed by gas chromatography. The principal experimental conditions are shown in **Table 1**.

2.2. Result and Discussion

The mass fractions of the components in absorption oil were descried as follows: Q 0.08, IQ 0.02, IL 0.04, 1MN 0.10, 2MN 0.28, BP 0.07, DBF 0.14. The mass fraction of 2MN was highest among homocyclic components, so that 2MN was taken as representative component of homocyclic compounds. The distribution coefficient of component i between aqueous phase and oil phase was defined as:

$$m_{i,R} = \frac{C_i}{x_i} \tag{1}$$

where C_i and x_i denote the mass fraction of compound i in the extract and raffinate phases, respectively. **Figures 1(a)-(d)** show the relation between $m_{i,R}$ of Q, IQ, IL, 2MN and concentration of TEG/DEG/EG in aqueous phase, C_A. The $m_{i,R}$ of nitrogen heterocyclic compounds Q, IQ, IL were larger than that of 2MN and, in all the cases with additives, distribution coefficients were larger than those without additive. At any case, the $m_{i,R}$ increased with increasing C_A. For example, the maximum $m_{Q,R}$ was 1.8×10^{-1} at C_{TEG}=0.5, that was nearly twenty times of that without TEG, and the maximum $m_{2MN,R}$ was 2.8×10^{-3} that was fifteen times of that without TEG. In case with DEG, the maximum $m_{Q,R}$ was 1.1×10^{-3} and $m_{2MN,R}$ was 2.4×10^{-3}; in case with EG, maximum $m_{Q,R}$ was 5.0×10^{-2} and $m_{2MN,R}$ was 1.2×10^{-3}. $m_{i,R}$ increased in the order of EG, DEG, and TEG cases. This result

Table 1 Experimental condition of liquid-liquid equilibrium

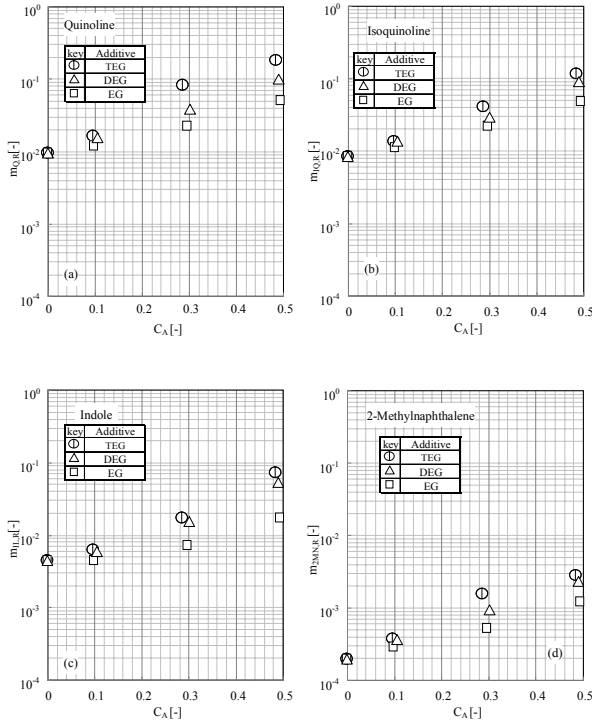| Oil phase	Absorption Oil	
mass, R_0 [kg]	0.05	
Aqueous phase	Aqueous solution of EG/DEG/TEG	
mass, E_0 [kg]	0.05	
Mass fraction of EG/DEG/TEG in Aqueous phase C_A [-]		0-0.05
Frequency of shaking	[h^{-1}]	5400
Amplitude of shaking	[m]	0.04
Shaking time	[h]	72
Temperature, T	[K]	303

1

Figure 1 Distribution coefficient of component which contained in AO (a) Quinoline (b) Isoquinoline (c) Indole (d) 2-methylnaphthalene

suggests that EG, DEG, TEG, added to a liquid membrane solution, would enhance the permeation of components. The $m_{i,R}/m_{2MN,R}$ slightly decreased by addition of the additives and also decreased with increasing concentration of additives. The effect of the additive difference was not observed clearly.

3. Batch separation of absorption oil with emulsion liquid membrane

3.1. Experimental

AO was used as inner oil phase; aqueous membrane solution consisted of ion-exchanged water, one of EG, DEG and TEG as permeation enhancing additive, and saponin as an emulsifying agent; toluene was used as external solvent phase. The feed AO and aqueous membrane solution were stirred by a commercial high-speed homogenizer to prepare the emulsion. This prepared emulsion was brought into contact with the solvent by stirring vessel which was made of Pyrex glass equipped with a six-flat-blade turbine type impeller and four baffles. **Figure 2** shows the schematic diagram of high-speed homogenizer and stirring vessel. Stirring started to begin a permeation run (t=0) and continued for a specified operating time. This operation was repeated for the several different times to obtain the time courses of the compositions in the extract phase etc. **Table 2** gives the detailed experiment conditions.

3.2. Results and Discussion
3.2.1. Basic Relationships

The permeation rate of component i through ideal one layer liquid membrane was represented by,

$$N = P_i \cdot A \cdot [x_i - \frac{m_{i,E}}{m_{i,R}} y_i] \tag{2}$$

Table 2 Experimental conditions for batch separation with emulsion liquid membrane

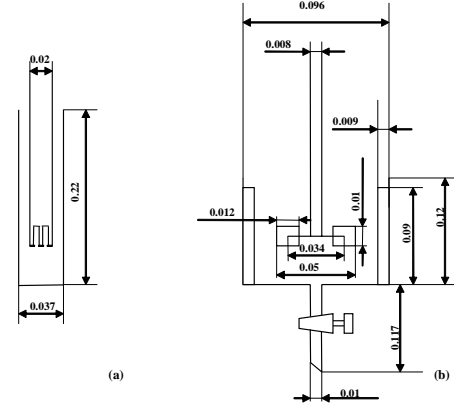| Feed	AO			
Membrane	Aqueous solution of saponin and EG/DEG/TEG			
Solvent	Toluene			
C_s [−]	N_e [h⁻¹]	N_p [h⁻¹]	V_T [m³]	C_A [−]
0.03	1.1×10^6	18000, 36000	4.0×10^{-4}	0~0.25
$\phi_{OW,0}$ [−]	$\phi_{O,0}$ [−]	t [h]	T [K]	
0.25	0.5	0~0.044	298±5(room temp.)	

Figure 2 Schematic diagrams of apparatuses for batch separation with emulsion liquid membrane (a) emulsifier with high-speed homogenizer (b) stirring vessel (unit in this figure is meter)

Here, overall permeation coefficient P_i can be expressed by next equation:

$$P_i = m_{i,R} \cdot D_i \cdot \rho / \delta \tag{3}$$

According to these equations the overall permeation coefficient, P_i would be influenced qualitatively by both distribution coefficients, $m_{i,R}$, and diffusion coefficient D_i. x_i can be calculated by mass balance as follows:

$$R_0 x_{i,0} + E_0 y_{i0} = R x_i + E y_i \tag{4}$$

Here, E and R were obtained from the experimental data. Yield of component i, Y_i, was defined as,

$$Y_i = E y_i / R_0 x_{i0} \tag{5}$$

where x_{i0} and y_i denote the mass fraction of component i in the inner oil phase at t=0 and that in the external extract oil phase after a run, respectively. R_0 refers to the initial mass of inner oil phase and E expresses the mass of out oil phase after the run. Separation selectivity of component i relative to 2MN was represented by,

$$\beta_{i,2MN} = \frac{y_i / y_{2MN}}{x_i / x_{2MN}} \tag{6}$$

3.2.2. Compositions of raffinate and extract

Figures 3 (a)-(d) show the time courses of x_i and y_i. In any case, x_i decreased and y_i increased with stirring time. In all the cases, y_i of the nitrogen heterocyclic compounds were larger than those of homocyclic compounds, although $x_{i,0}$ of homocyclic compounds were higher than those of nitrogen heterocyclic compounds. Nitrogen heterocyclic compounds were selectively transferred through liquid membrane to extract phase and could be separated from homocyclic compounds. **Figure 3 (d)** shows effect of different additives on x_Q and y_Q. x_Q decreased and y_Q increased in the order of EG, TEG, and DEG cases. $m_{Q,R}$ increased in the order of EG, DEG, and TEG cases, as shown in Figure 1. On the contrary, the diffusion coefficient, D_Q, would increase in the order of
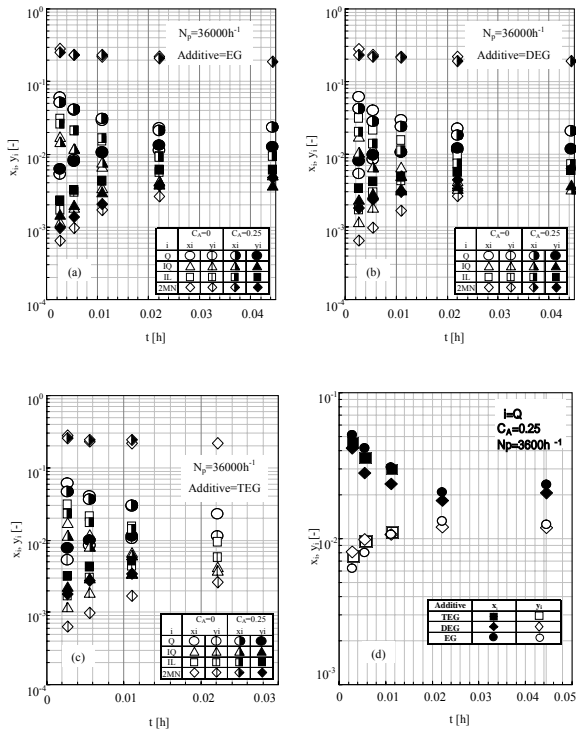
2

Figure 3 Time course of composition (a) with EG in aqueous membrane solution (b) with DEG in aqueous membrane solution (c) with TEG in aqueous membrane solution (d) compare the effect of different additives (EG, DEG, TEG)

TEG, DEG, and EG cases, based on the Wilke-Chang equation, since the viscosity decreased in the order of TEG, DEG, and EG cases. Both of $m_{Q,R}$ and D_Q affected the permeation rate as Eqs.(1) and (2).

3.2.3 Yield

Figures 4 (a)-(c) are proving that the yields of nitrogen heterocyclic compounds, Q, IQ, and IL were definitely larger than those of 2MN. All kinds of additives did enhance the yields of all the components, obviously. The highest Y_Q, Y_{IQ}, and Y_{IL} in the additive cases were almost as 1.5 times larger than that without additive. These results were attributed to increase of the distribution coefficients as shown in **Figure 1**. The effect of different additives on Y_Q was shown in **Figure 4 (d)**. Y_Q increased in the order of EG, TEG and DEG cases, because $m_{Q,R}$ increased and D_Q decreased as mentioned above. **Figure 4 (e)** indicates the relation between Y_Q and C_A. The Y_Q increased with increasing C_A. This mainly resulted from the increase of distribution coefficients as shown in **Figure 1**. The relation between yields and stirring velocity was shown in **Figure 4 (f)**. Higher stirring velocity gave higher yield, since the interfacial contact area between emulsion and external phase, A, increased.

3.2.4 Separation selectivity

Figures 5 (a)-(c) show the effects of additives EG, DEG, and TEG on separation selectivities of nitrogen heterocyclic compounds. Any kind of additive lowered these separation selectivities, because m_i/m_{2MN} decreased with adding the additives. **Figures 5 (b)-(d)** indicate the relation between additive concentration and separation selectivity of i. In all the cases separation selectivity of
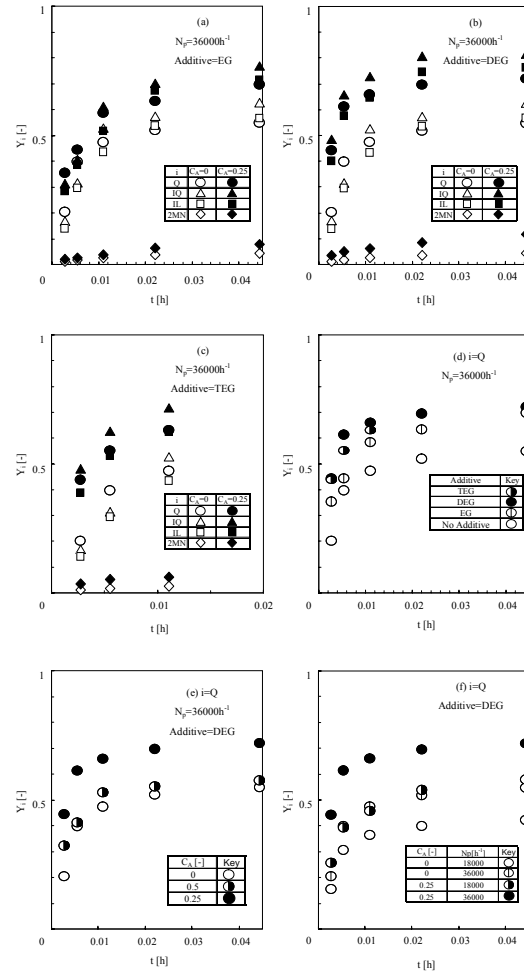

Figure 4 Time course of yields (a) with the EG in aqueous membrane solution (b) with the DEG in aqueous membrane solution (c) with the TEG in aqueous membrane solution (d) compare the effect of different additives (TEG, DEG, EG) (e) relation between yields of Q and additive concentration in aqueous membrane solution (f) relationship between yield of Q and stirring velocity of permeation

component i decreased with increasing concentration of additives in aqueous membrane solution, because the m_i/m_{2MN} decreased.

The relation between stirring velocity and separation selectivity is shown in **Figure 5 (e)**. The separation selectivity of component i increased with stirring velocity. The emulsion drop size and, then, the number of internal oil droplet in a emulsion drop decreased, so that the unfavorable concentration distribution in a emulsion drop disappeared[8].

4. Conclusions

The distribution coefficients of the components contained in absorption oil between absorption oil and aqueous phases increased by addition and with increasing concentration of the additives, EG, DEG, and TEG. This suggested that these additives would be added into the membrane liquid to improve the performance of emulsion liquid membrane separation. The permeation rates of the components in absorption oil were increased by addition of the additives into the membrane liquid in batch emulsion liquid membrane permeation runs, as predicted from the above liquid-liquid equilibrium.
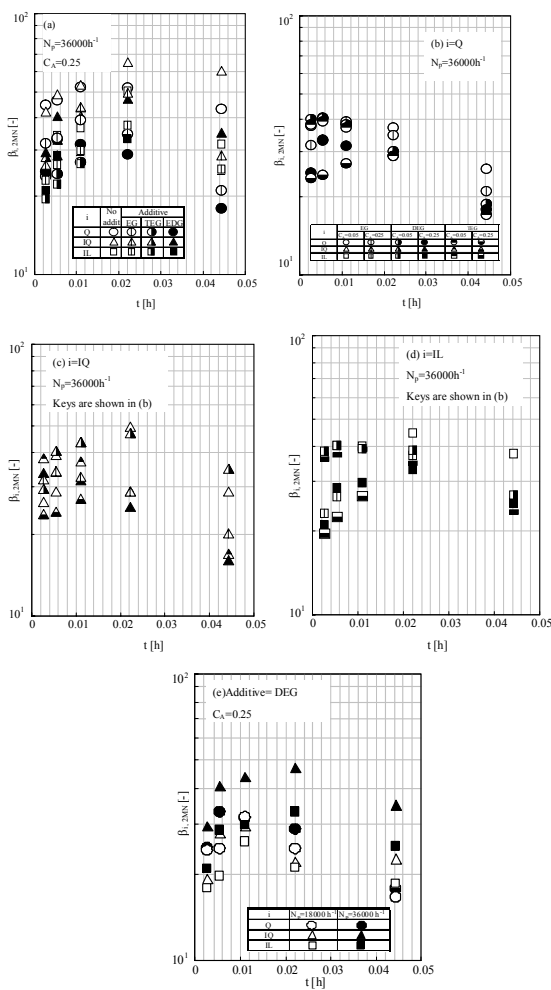
3

Figure 5 Time course of separation selectivity (a) effect of different additives on separation selectivity (b) relation between additive concentrations and separation selectivity of Q(c) relation between additive concentration and selectivity of IQ (d) relationship between additive concentration and separation selectivity of IL (e) effect of stirring velocity on separation selectivity of Q

Nomenclatures

A	= contact area	[m^2]
C_A	= mass fraction of the additive in aqueous membrane phase	[-]
C_s	= mass fraction of the saponin in aqueous membrane phase	[-]
C_i	= mass fraction in extract phase	[-]
Di	= diffusivity of component i in liquid membrane	[-]
E	= mass of extraction	[kg]
m	= distribution coefficient	[-]
M	= mass of aqueous phase	[kg]
N_e	= stirring velocity at emulsification	[h^{-1}]
N_p	= stirring velocity in permeation vessel	[h^{-1}]
p_i	= permeation coefficient of component i	[kg
R	= mass of raffinate phase	[g]
V_T	= total volume of liquid in permeation vessel	[m^3]
x	= mass fraction in raffinate phase	[-]
y	= mass fraction in extract phase	[-]
$\beta_{i,2MN}$	= separation selectivity of component i relative to 2-methylnaphthalene	[-]

<Subscript>

i	= component i	
A	= additive	
Q	= quinoline	
IQ	= Isoquinoline	
IL	= Indole	
1MN	= 1-methylnaphthalene	
2MN	= 2-methylnaphthalene	
BP	= Biphenyl	
DBF	= Dibenzofuran	
EG	= Ethylene glycol	
DEG	= Diethylene glycol	
TEG	= Triethylene glycol	

Reference

1) Hara, N.; "Permeation of Nitrogen Heterocyclic Compounds through Supported Liquid Membrane," Bachelor Thesis, Tokyo Tech (2001)

2) Hara, N.; "Improvement of Rough Separation with O/W/O Liquid Membrane from Coal Tar Absorption Oil," Master Thesis, Tokyo Tech (2003)

3) Nagai, M.; "Separation of Nitrogen Heterocyclic Compounds Contained in Coal Tar Absorption Oil Fraction by Extraction," Bachelor Thesis, Tokyo Tech (1999)

4) Nagai, M.; "Rough Separation of Heterocyclic Nitrogen Compounds Contained in Coal Tar Absorption Oil Fraction," Master Thesis, Tokyo Tech (2001)

5) Saito J.; "Separation of absorption oil and tar light oil by solvent extraction method," Bachelor Thesis, Tokyo Tech (2004)

6) Bi, D.; "Separation of Coal Tar Absorption with O/W/O Emulsion liquid Membrane-Effect of Additive in Membrane Liquid-"Bachelor Thesis, Tokyo Tech (2006)

7) Kato, S. and J. Kawasaki; "Enhanced Permeation of Hydrocarbons through Liquid Membranes by Lipophilic surfactants," J. Chem. Eng. Japan, 20, (2), 140-145

8) Egashira, R., H. Tanno, S. Kato and J. Kawasaki; "A Simple way for the Improvement of Separation Selectivity of Hydrocarbons by O/W/O Emulsion Liquid membrane," J. Chem. Eng. Japan, 28, 38-45 (1995b)

4

STRENGTH OF CLAY SEAM ALONG THE POTENTIAL FAILURE PLANE IN SOFT ROCK SLOPES

Student Number: 06M18205 Name: Sokbil HENG Supervisor: Hideki OHTA

軟岩斜面の滑り面における粘土薄層の強度特性

ヘン　ソクビル

多くの岩盤斜面の破壊においては，粘土薄層の存在によって滑り面が形成される．本研究は軟岩斜面の滑り面における粘土薄層の強度特性を調査するために定体積一面せん断実験を行った．不撹乱試料に現れた粘着力は水中でせん断すると消失するが，室内試験において不飽和・乾燥させたら再び現れることが判明した．従い，現場における強度を室内試験において再現できるのは，内部摩擦角のみであるという理由から，実用的な方法として不撹乱試料の代わりに練返し試料から強度定数がある程度得られる．実験を通して提案されたせん断抵抗特定の決定法を用いて，実際に現場で発生した斜面破壊の安定計算を実行し、その妥当性を確認した．

1. INTRODUCTION

Temperature rises in global warming issue making the tropical ocean over warm, and subsequently appearing year by year a series of miserable natural disasters. Rockslide is one amoung the disasters occuring at the hill or the mountain area, provoked the environmental destruction and damaged lives and properties on the high land as well as along the valley. The failure, triggered by heavy rain fall, earthquake and excavation, often occurred at the potential slip plane where the weak layer of clay seam reposed with its relatively thin layer. Even thought the issue is not new, the catastrophe remains severe and difficult to predict.

Understanding the behaviour of clay seam is very crucial for the safety designed factor in slope stability analysis. In recent year, many research works are undertaken, aiming to demonstrate the appropriate and more reliable strength parameter determination of slope materials. The collection of undisturbed samples of clay seam, although difficult, is believed important by many researchers.

This study focuses particularly on the strength behaviour of clay seam at the failure plane in soft rock slope. Constant volume shear box test was used in the experimental work in order to investigate cohesion and friction angle of the specimen colleted from Shizuoka, Japan, where cutting slopes for the new Tomei Highway's construction are under operation. The experiment work had also been conducted on disturbed sample of clay seam from Guinsaugon, Philippines where experienced the rock slope failure.

Shear strength parameters of clay seam obtained from laboratory tests will be used in safety factor analysis of this study.

2. LITERATURE REVIEW

The shear strength parameters of soil known as cohesion c and internal friction angle ϕ have been discussed amoung experts in geotechnical fields. An advantage come from their interpretation will be a backbone of final recommendation.

- Mohr-Coulomb's theory (Terzaghi 1943)
  Shear strength of soil: $\tau = c' + \sigma' \tan \phi'$ (2.1)

- Terzaghi and Hvorslav's interpretation (1937)
  Shear strength of soil: $s = c_e + \sigma' \tan \phi_e$ (2.2)

- Taylor's interpretation (1948)
  Shear strength of soil: $\tau = \dfrac{dz}{dx}\sigma' + \sigma' \tan \phi'$ (2.3)

  $\dfrac{dz}{dx}$ rate of dilataion, resulting an apparent interlocking

- Schofield opposed to Terzaghi and Hvorslav
  Schofield (2006) refered to shear strength of soil has no true cohesion, only apparent interlocking obsearves at dry side.

Observation showed that a presence of cohesion in safety factor design made the safety factor overestimated to safe side, whereas in reality, unstability and failure occured.

3. METHODOLOGY

In general intact sample of clay seam collected at a weak plane is best to represent the properties of material at a potential failure plane. It shall be taken at some locations along the plane and at natural condition to be analyzed especially the potential state at which soft rock might possible to slide. Rock slope failure occurred at the weak plane where laying on the clay seam with its variety of thickness. Most observation cases have indicated that rockslide happened after a huge soft rock mass saturated in a following weeks after heavy rainfall. The rainstorm induces an increase of sliding force and to weaken the shear strength of clay seam. Therefore the sample which could be best to represented the critical state of clay seam shall be taken at the submerged state. However, to collecte sample at dangerious moment is not practical.
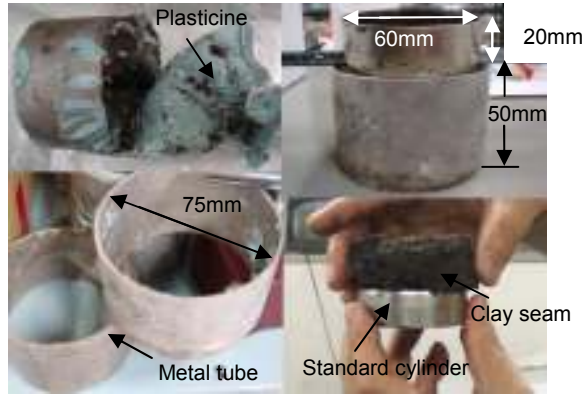
(1) Site sampling operation

Fig.1 Metal tube for taking and storing clay

In this study, samples were taken at unsaturated condition from a weak plane where discontinuity riches of soft material clay; and types of sample were classified as undisturbed and reconstituted sample. Because a plane failure is consisted not only the clay seam but also of some mixed gravel, the sampling size of undisturbed sample shall be greater than enough fit to the dimension in a shear box. For instance, the sample taken shall have diameter and height larger than a standard cylinder of 60mm diameter and 20mm height (i.e. 75mm diameter and 50mm height). Metal tube is used to penetrate into clay seam layer at least 20mm depth and in some case additional force need to apply when this layer is stiff. The metal tube must stand in position perpendicular to the plane surface regardless to the vertical. The sample placing in the solid tube needs to be covered by plastcine and plastic rap in order to keep its original position (direction of plane) and its moisture content (see fig. 1).

(2) Laboratory testing method

Consistency of clay seam

Liquid limit (*LL*) and plastic limit (*PL*) are necessarily determined on soils which have had their natural structure completely destroyed by kneading or remoulding. Specimen used for testing has to be fine particle of diameter not excess 0.425mm. Therefore sieving process is necessary for clay seam in which some gross particles is mixing inside.

Effective friction angle can also be appeocximated by an empirical relation, (Kenney (1959)).

$$\sin \phi' = 0.81 - 0.233 \log PI \qquad (3.1)$$

where plasticity index *PI=LL-PL*

Specific gravity of clay seam

The specific gravity of a soil is often used in relating a weight of soil to its volume. Therefore, knowing the unit weight of a moist soil can be computed when knowing the void ratio, the degree of saturation, and the specific gravity.

This experiment was carried aiming at defining the unit weight of soil which is necessary in nearly all pressure, settlement, and especially stability problems in soil engineering.

Specific gravity of clay seam

The specific gravity of a soil is often used in relating a weight of soil to its volume. Therefore, knowning the unit wight of a moisture soil can be computed when when knowing the void ratio, the degree of saturation, and the specific gravity.

This experiment was carry out in order to obtain the unit weight of soil which is necessary in calculation over burden spressure in stability analysis.

Shear strength of clay seam

Strength parameter of clay seam can be investigated by using few laboratory testing methods among them are triaxial test, simple shear test, direct shear test and constant volume shear test. Observation shows that thickness of clay seam is not excess few centimetre and the condition at failure is free for water to drain out. It is thus drained condition of shear test shall be best to suit the case. Drained direct shear test using direct shear box box test is one of simple methods often used at laboratory. Application of this method consumes so much time as the shearing speed is very slow in order to assure that there is no excess pore water pressure during the testing process. Constant volume shear box test, however, does not require so much time when water was freely to either stay inside or flow out from the specimen. Vertical strain is controlled by varying vertical stress during shearing process. Horizontal displacement is governed by a constant velocity of 0.2mm per minute. Vertical and horizontal stress and displacement were recorded by loadcells and strain guages connecting to data logger.

Multistage-consolidated shearing process was performed with the different types of specimens at different conditions. Stress paths of each sample are plotted and the interpretation of each condition is stated in article 4.

(3) Experimental program

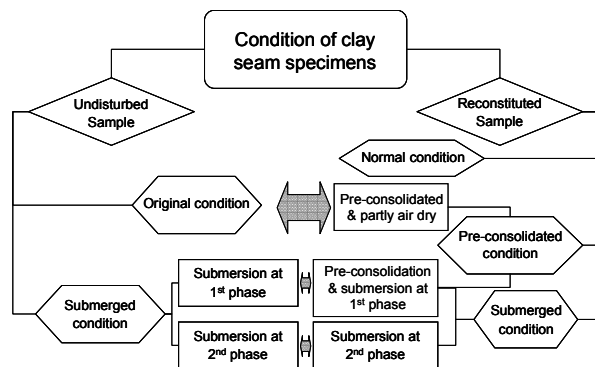Program testing on different specimens' condition:
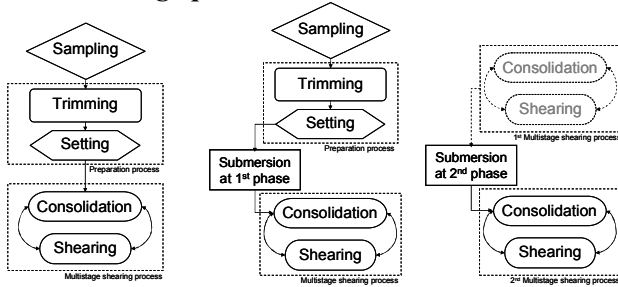

Fig.2 Diagram fitting specimens condition

2

Fig.3 Testing operation for undisturbed sample

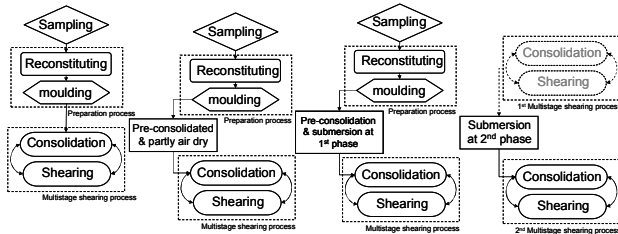Fig.4 Testing operation for reconstituted sample

Laboratory testing procedures

a) Preparation process

Trimming and setting of undisturbed sample: Once the samples manipulated to the laboratory, the trimming process can be operated on the undisturbed sample in order to have an appropriated geometric form which is just fit to the shear box apparatus. By carefully and patiently removing the sample covered with plasticine little by little from metal tube, spatula or cuter is used to slice laterally without much disturbance to the structure of sample. Specimen sunk into a pattern cylinder of 60mm diameter and 20mm height when its dimension just a little fit to the cylinder. Finally, only both surfaces of lower and upper clay seam sample are needed to be trimmed and flattened. The specimen in the cylinder is just having a good geometrical form as its container and later released to the shear box apparatus.

Reconstituting and remoulding of a sample: Disturbed clay seam collected from the site or some residual amount from trimming of undisturbed specimen can be reused to reconstitute a new sample by mixing the clay with some water, making it softer or paste-like material. In certain cases, granular of diameter bigger than 2mm, contained in clay seam is needed to remove by letting the slurry flow through the sieve of 2mm diameter. That slurry then moulded in a shear box apparatus which covered at upper and lower cylinder with porous stones through which water can drain out.

b) Submersion processes

This process is conducted over unsaturated sample (intact condition or reconstituted condition) at the beginning of shearing process (submersion at 1st phase, or over unsaturated sample at the end of 1st multistage shearing process (submersion at 2nd phase,) aiming to observe shear resistance at submerged condition of the sample.

c) Pre-consolidated and partly air dry

The pre-consolidated and party air dry procedure is the particular case of investigation in the experimental program. It was initiated in order to clarify how capillary force acts on the sample during man-hours for undisturbed specimen preparation. Specimen was once experienced a reconsolidated pressure of 80kPa and released by few hours exposing to the air at an open top caps. This model simulated the physical appearance of undisturbed sample of which residual effective stress releases and moisture content diminishes during the time of sampling preparation.

d) Multistage shearing processes

Consolidation process: Constant volume shear test is operated in accordance with specification as described in a manual of Testing of Soil Mechanics, produced by The Japanese Geotechnical Society (2001). Clay seam specimen was trimmed and set into the shear box apparatus, then started to consolidate with normal pressure of 9.8kPa, in case of submersion, water was poured around the metal device inside the acrylic rectangular box and kept for 2 to 3 hours before starting consolidation. Consolidation time was estimated by using square root of time ($\sqrt{t}$) method or three time (3t) method.

Shearing process: Once after finishing consolidation, shearing force is applied horizontally with a constant speed of 0.2mm per minute until the horizontal displacement reaches to 7mm and the shearing ends at that time (35mns stated from the setting time). The specimen then forced to return to the beginning position and reconsolidated with double pressure before the other shearing stage restarts. The entire shearing process comprises 6stages with the same procedure, consolidation then shearing.
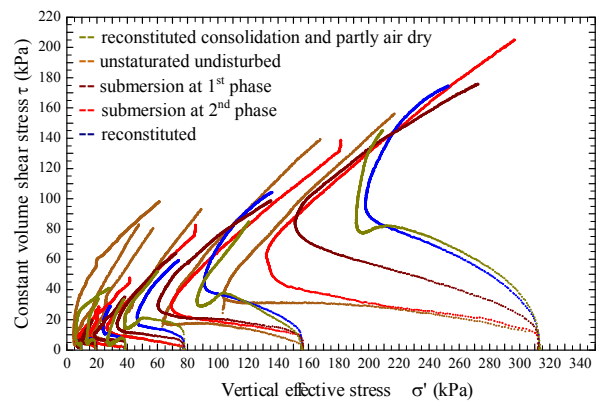
4. EXPERIMENTAL RESULTS

Fig.5 Stress paths during the constant volume shear

Experimental results obtained from 5 unsaturated undisturbed samples showed a considerable cohesion value similar to a model reconstituted sample under

preconsolidation pressure and partly air dry condition. In submerged condition of the same sample, strss paths showed a relatively small value or negative apparent cohesion. Similar to this case the reconstituted sample is comparable to the submerged condtion.

Figure 5 showed the stress paths of sample from Nakanogou at different conditions. At intact state, apparent cohesion reached to 40kPa and at submersion 2nd phase, little apparent of $c' = 6kPa$. The other samples taken at the same site Nakanogou, a reconstituted sample and the clay seam sample at failure plane showed negative apparence of cohesion with angle at kink 24.6^o and 20° respectively. All the case of testing conditions are subject to verify in back analysis in following article.

5. BACK ANALYSIS

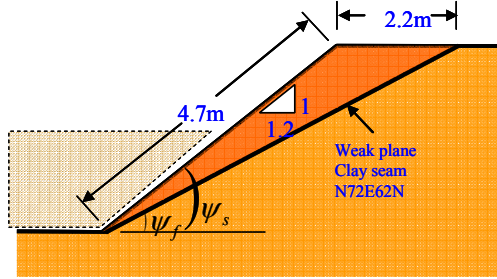A case of slope failure occurred in Nakanogou, 2004 has its records as presented in the figure below:

Fig. 6 Model of 2D Plane failure of Nakanogou site

Total unit weigth of material: $\gamma_t = 22.51 kN/m^3$

Weigth of massmovement: $W_f = 74.49 kN$

Normal component of weight:

$$F_n = W_f \cos\psi_f = 74.49 \times \cos 27.38^o = 66.15 kN$$

Tangential component of weight:

$$F_t = W_f \sin\psi_f = 74.49 \times \sin 27.38^o = 34.25 kN$$

According to equation (2.2), $c' = 0$

Resistance force: $F_R = F_n \tan\phi' = 66.15 \tan\phi'(kN)$

Safety factor against slidding:

$$F_s = \frac{\text{shear resistance}}{\text{mobilized shear stress}} = \frac{F_R}{F_t} = \frac{66.15 \tan\phi'}{34.25} = 1.931 \tan\phi'$$

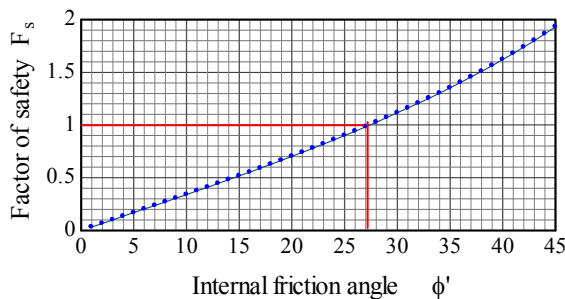Fig.7 Relation between safety factor and friction angle of Nakanogou soil with $\gamma_t = 22.51 kN/m^3$

Regarless the cohesion in safety design with, figure 7 shows the factor of safety against sliding for Nakanogou clay seam. For all conditions of soil samples, friction angle at kink level resistes with the safety factor less than one, and that result agreed with the site respond that slope failed under that condition.

On the other hand, by including cohesion in safety factor design, the result showed safety factor equal 1.85 and 8.34 for strength parameter of submersion at 2nd phase ($c' = 6kPa$, $\phi' = 23.5^o$) and of non-submerged intact sample ($c' = 40kPa$, $\phi'=20.1^o$) respectively.

6. CONCLUSION

i)   apparent cohesion obtained from laboratory test is resulted from the effect of capillary force forming during the sampling at site and laboratory process only and it does not represent the real condition of the site behaviour.

ii)   apparent cohesion will disappear partly or totally after submerging or re-submerging into the water. Using this cohesion in safety factor analysis showing risk of lower estimation.

iii)   to avoid capillary action, shear test in submerged condition is recommended, otherwise apparent cohesion obtained from non-fully saturated sample shall be exempted.

iv)   reconstituted sample, of which major cohesion disappear and only its friction angle is comparable to that of the submerged undisturbed samples shall be able to represent the shale sample of clay seam at submerged state. Advantages of reconstituted sample gain through this finding.

v)   effective friction angle represented by a line crossing at kinks agrees well in safety factor design.

REFERENCES

1)   Ohta, H. et al, "Case records of rock slope failures," *Proceedings of the Second Japan-Philippine Workshop on Safety of Infrastructure against Environmental Impacts*, Core University Program of JSPS on Environmental Engineering, Sept 2001, pp. 179-192.

2)   Thirapong, P., "Rock slope failure analysis," *Mechanics of geo-material, Special Seminar,* 2008.

3)   Hoek, E. and Bray, J.W., "Graphical presentation of geological data," *Rock Slope Engineering, Ch. 2,* 1977, pp. 37-63

4)   Takemura, J., "Sampling and Laboratory testing of cohesive geomaterials," *Mechanics of Geomaterials, special course's lecture at Tokyo Tech,* 27April 2006, pp. 1-16.

5)   Terzaghi, K. and Peck, R.B., "Shearing Resistance of Soil," *Soil Mechanics in Engineering Practice, Ch.2, Atr.15*, 1948, pp 78-104

6)   Schofield, A.N., "Letter to Editor," *Géotechnique 56, No. 5*, 2006, pp 357-358

7)   Lambe, T.W., "Soil Testing for Engineers," *Massachustts Institute of Technology, 1951*, Trans-Edition 1982.

8)   Bjerrum, L. and Landa, A., "Direct simple-shear tests on a Norwegian quick clay," *Geotechnique, 16(1)*, 1966, pp 1-20

9)   Brady, B.H.G. and Brown, E.T., "Rock mass structure and characterisation," *Rock Mechanics for Underground mining*, 1985, pp. 46-82.

10)   NEXCO., "Geological Data and Material Properties," 2004-2007

11)   土質試験　基本と手引き　2001 年（社団法人地盤工学会

4